Analysis of non-stationary signals in dispersive media : contribution of compressive sensing techniques for interference management

Isidora Stankovic

THESIS

for jointly obtaining the grade of

DOCTOR OF TECHNICAL SCIENCES (PHD)

Spécialité : **Signal, image, paroles, télécoms**

Arrêté ministériel : 7 août 2006

Authored by
Isidora STANKOVIC
Thesis supervised by **Milos DAKOVIC** and **Cornel IOANA**
prepared at
Grenoble Image Parole Signal Automatique (GIPSA) laboratory in **Electronique, Electrotechnique, Automatique et Traitement du signal (EEATS) doctoral school**
and
Faculty of Electrical Engineering (FEE) at **University of Montenegro (UoM)**

Analysis of non-stationary signals: contribution of compressive sensing for interference management in dispersive media

Thèse soutenue publiquement le **4 juin 2021**,
devant le jury composé de:

Patrick FLANDRIN
Directeur de Recherche CNRS à ENS Lyon, Rapporteur
Cédric RICHARD
Professeur à l'Université de Nice, Rapporteur
Jérôme MARS
Professeur Grenoble INP GIPSA-lab, Examinateur
Jonatan LERGA
Professeur Université de Rijeka Croatie, Examinateur
Irena OROVIC
Professeur Université de Monténégro, Examinateur
Eric GAUSSIER
Professeur Grenoble INP GIPSA-lab, Président du jury
Milos DAKOVIC
Professeur Université de Monténégro, Codirecteur de thèse
Cornel IOANA
Maitre de Conférences Grenoble INP, GIPSA-Lab, Directeur de thèse

T H E S I S

Analysis of non-stationary signals: contribution of compressive sensing for interference management in dispersive media

Presented and defended by

Isidora STANKOVIC

for jointly obtaining the

DOCTORATE DEGREE

of University of Grenoble Alpes
Doctoral School for Electronics, Electrical Energy, Automatic Control, Signal Processing
Specialization: Signal, Image, Speech, Telecommunications

and the

DOCTORATE DEGREE IN TECHNICAL SCIENCES

of University of Montenegro
Faculty of Electrical Engineering
Specialization: Digital Signal Processing

Thesis directed by Milos DAKOVIC and Cornel IOANA.

Prepared at the Grenoble Image Parole Signal Automatique (GIPSA) lab
and at the Faculty of Electrical Engineering (FEE).

Defended in Grenoble, on 10.02.2020.

Jury :

Rapporteurs :	Patrick FLANDRIN	-	Directeur de Recherche CNRS à ENS Lyon
	Cédric RICHARD	-	Professeur à l'Université de Nice
Directeurs :	Cornel IOANA	-	Maitre de Conférences, Grenoble INP, GIPSA-lab
	Milos DAKOVIC	-	Professeur Université de Monténégro
Examinateurs :	Jérôme MARS	-	Professeur Grenoble INP GIPSA-lab
	Jonatan LERGA	-	Professeur Université de Rijeka Croatie
	Irena OROVIC	-	Professeur Université de Monténégro
	Eric GAUSSIER	-	Professeur Grenoble INP GIPSA-lab

Abstract

In signal processing, the theory behind compressive sensing presented a successful sampling technique in various fields. Using a small number of measurements for the acquisition improves the efficiency of storage, memory, and transmission of signals. Since numerous signals in nature can be represented as sparse in some representation domain, the technique showed massive potential in many areas such as medicine, telecommunications, radar, and sonar systems. Although very successful, compressive sensing is not yet fully developed and implemented in underwater acoustics. Acoustic signals transmitted through water introduce many complex characteristics making their analysis challenging and difficult. The process of transmitting and receiving signals through shallow water environment is a representative example of a signal transmission through dispersive channel. The non-stationary nature of such signals leads to the time-frequency signal analysis as well developed theory suitable for non-stationary signal processing. Within the compressive sensing framework, it is important to emphasize that the non-stationary signals are only approximately sparse or nonsparse in the corresponding transformation domain. Since the compressive sensing reconstruction methods intrinsically relies on the sparsity, the reconstruction of approximately sparse or non-sparse signals will produce an error that should be considered in the calculations and applications. The main contributions of this thesis are in extending and adjusting the compressive sensing methods and results to the non-stationary signals, with application to the acoustic and sonar signals. This can include dispersive media propagation. In particular, the exact expected error of the reconstruction of non-stationary signals in time-frequency analysis using the compressive sensing methods is derived. The decomposition and reconstruction of signals in sonar systems and dispersive underwater channels using time-frequency approaches are presented. Various sequences used in the sonar imaging are considered from the point of the compressive sensing based reconstruction, including a reduced set of measurements or highly corrupted samples and real-world scenario setup. All of the presented theoretical results are followed by numerous examples. Application of the proposed methods and obtained theoretical results to image reconstruction and denoising problems is also presented as an example that developed tools and theoretical results are important not only for underwater acoustic systems. The algorithms used to achieve the main results in the thesis are given in the Appendix.

Acknowledgements

I want to thank the University of Montenegro (Faculty of Electrical Engineering) and the University of Grenoble Alpes (GIPSA Lab, INP Grenoble), for giving me the opportunity to study and achieve the title of PhD under the double-degree program. Also, I would like to thank the Ministry of Science of Montenegro for seeing the potential of this thesis and financially supporting its realization.

This thesis would not have been written without my two thesis supervisors, prof. Milos Dakovic and prof. Cornel Ioana. Your selfless guidance and patience during all these years helped me finish my goals, and I am eternally grateful for that.

I want to thank prof. Irena Orovic, prof. Igor Djurovic, prof. Olivier Michel, prof. Angela Digulescu, prof. Ervin Sejdic, prof. Ilija Vujosevic, prof. Rada Dragovic Ivanovic, prof. Budimir Lutovac, prof. Vesna Popovic Bugarin, prof. Wei Dai, prof. Jerome Mars, prof. Gabriel Vasile, prof. Joachim Ender, prof. Mokhtar Mohammadi, and prof. Jonatan Lerga, for allowing me to work with and learn from them, as well as for their support and suggestions during the research. Also, I would like to thank all the HR staff of Faculty of Electircal Engineering and GIPSA Lab for helping me during the process and making the balance between the offices in Montenegro and France as easy as possible.

A huge thank to my dear people from the Faculty of Electrical Engineering in Montenegro, Dr Milos Brajovic, Dr Andjela Draganic, Stefan Vujovic, and Nikola Bulatovic, for all the joyful moments we had in and out of the lab. A very big gratitude goes to Dr Karina Ashurbekova, Dr Saloua Chlaily, Akerke Dinzhumanova, Hardik Doshi, and Dr Jitendra Sewada, for making Grenoble feel like home to me. A special thanks to my office buddy Julien Muzeau for his strong patience and help during my stay in Grenoble. Also, I want to thank all other people from GIPSA Lab, for the unforgettable days and coffee breaks at 5 o'clock.

To all my friends in London and Montenegro, I want to thank you for all the time when I let my problems go away when I am with you. It would definitely be hard to move forward without your presence and constant encouragement.

I dedicate this thesis to my niece Iskra, who gives me the reason to finish my goals and be a better person every day. In the end, I want to thank my family for everything that they did for me, for all the powerful, kind, and encouraging words they were sharing with me to help me succeed not only in my thesis but also in life. I deeply appreciate all of your hard work, which helped me be where I am at right now. I love you.

Contents

List of Figures

List of Tables

List of Acronyms and Abbreviations

2D-DCT	Two-Dimensional Discrete Cosine Transform
2D-DFT	Two-Dimensional Discrete Fourier Transform
AC	Auto-Correlation
AF	Ambiguity Function
CAZAC	Constant Amplitude Zero Autocorrelation
CoSaMP	Compressive sampling matching pursuit
CS	Compressive Sensing
DCT	Discrete Cosine Transform
DFT	Discrete Fourier Transfrom
DWT	Discrete Wavelet Transfrom
DOA	Direction Of Arrival
DPFT	Dual Polynomial Fourier Transform
ECG	Electrocardiogram
EEG	Electroencephalogram
FPGA	Field Programmable Gate Arrays
FT	Fourier Transform
IHT	Iterative Hard Thresholding
ISAR	Inverse Synthetic Aperture Radar
ISTA	Iterative Shrinkage Thresholding Algorithm
JPEG	Joint Photographic Experts Group
LASSO	Least Absolute Shrinkage and Selection Operator
LFM	Linear Frequency Modulated
LPFT	Local Polynomial Fourier Transform
MAE	Mean Absolute Error
MF	Matched Filter

MRI	Magnetic Resonance Imaging
MSE	Mean Squared Error
MUSIC	Multiple Signal Classification
OMP	Orthogonal Matching Pursuit
PFT	Polynomial Fourier Transform
PSNR	Peak Signal to Noise Ratio
PWD	Pseudo Wigner Distribution
RIP	Restricted Isometry Property
SAR	Synthetic Aperture Radar
SM	S-Method
SNR	Signal to Noise Ratio
SSIM	Structural Similarity
SSP	Sparse Signal Processing
TV-L1	Total Variation L1
STFT	Short-Time Fourier Transform
QF	Quality Factor
WT	Wavelet Transform

Introduction

In recent years, compressive sensing had an enormous breakthrough in the signal processing community as a successful sampling and reconstruction method for signals in various areas. The idea of using a small number of randomly positioned observations for signal acquisition improves efficiency od signal processing systems in terms of storage, memory, and transmission. Accurate recovery of signals with a reduced set of measurements is the primary goal of compressive sensing and sparse signal processing. Defining the domain of sparsity of a signal is the first step to be considered for application of compressive sensing to specific signal. Each of the signals and their sparsity domains has characteristics that are important for defining the method that should be used for their proper recovery. Many signals can be represented as sparse in some representation domain, resulting in compressive sensing showing a huge potential originally in medicine, and then later in many other fields, such as communications, meteorology, remote sensing, image processing, and radar and sonar systems.

Although very successful, the idea of compressive sensing is still challenging for research and developing in many application areas, including the underwater acoustics field. Acoustic signals transmission through the water introduce many complex characteristics that are very difficult for analysis. Most of the problems occur in the process of transmitting and receiving signals in water due to its dispersive media properties. This is especially exhibited in shallow water environments, as a representative example of dispersive channels. The dispersivity produces multiple nonlinear components, changing the very nature of the original transmitted signals. The non-stationary nature of such signal components makes them suitable for the analysis using time-frequency tools.

In the compressive sensing sense, non-stationary signals are only approximately sparse or nonsparse in the most of the common transformation domains. Such signals, when reconstructed under the sparsity assumption, will produce errors in the reconstruction procedure. This error highly depends on the sampling method and the sparsity domain of the analyzed signal. The exact error is of great importance for further improvement of the reconstruction performance in prospective. Except for the dispersive systems, time-varying nonsparse signals can also be found in the processing of many other areas, such as audio signals, images, radar systems, and wideband sonar images, where the processing under the sparsity assumption requires appropriate analysis of the reconstruction results.

The problem of approximative sparsity is intrinsically built in the area of compressive sensing based reconstruction of targets in sonar images. In real-world cases, the sonar signals are positioned off-grid in the transformation domain, which makes them nonsparse in their nature. The problem of finding a sequence suitable for the transmission, as well as developing the proper theory behind the detection and reconstruction of targets, is a topic of great importance for theory and practice in sonar systems. Considering that only a few target points (or few targets) commonly are of the interest in the sonar images, the idea of compressive sensing can successfully be applied in their reconstruction. The compressive sensing methods

can be suited and used for effective localization of the underwater targets in sonar systems.

The dispersive characteristics of the underwater environment is of crucial importance in the underwater acoustics and signal processing. A typical example of a dispersive media is the shallow water environment since most activities are performed in waters with deep less than 200 meters. From the signal processing view, a dispersive channel introduces many complex nonstationary components during the signal transmission. It is essential to recognize, decompose, and reconstruct such components (modes) truthfully, for a better understanding of the environment in which the signal is transmitted. Although challenging, the theory of compressive sensing with appropriate transformation domain, adjusted to the complex nature of the signal modes, can provide an effective reconstruction of the strongest modes.

Three key problems which are considered in this thesis are:

1. exact error calculation in the reconstruction procedure in compressive sensing (only error bound were given in the existing literature);
2. reconstruction of sonar images within the compressive sensing framework using various sequences for transmitted signal (so far only basic sequence forms were used in the literature, applied on the real data);
3. the problem of decomposition of signals in dispersive channels (with a robust method for such an requirement).

One of the aims of this thesis is to fulfill the gaps of using the compressive sensing techniques in underwater acoustic and sonar systems with appropriate and exact reconstruction performance analysis, which can also serve as a basis for a further direction in implementation of these techniques in other signal processing fields.

The contribution of this thesis can be divided into three major parts:

- **Analysis of nonsparsity** – Many signals, especially non-stationary and signals arriving from a dispersive environment are not strictly sparse in their corresponding transformation domains. They should be considered as approximately sparse or nonsparse signals, meaning that all components cannot be exactly reconstructed with compressive sensing methods. The expected reconstruction error caused by the nonreconstructed components is derived and exactly calculated. This helps further investigation on the quality of the reconstruction of various signals. The problem of quantization (digitization) of measurements is considered within the context of additive noise and signal nonsparsity.
- **Reconstruction of sonar signals** – The wideband sonar images can be reconstructed using different sequence forms. An extensive analysis of different sequence forms within the compressive sensing reconstruction framework is done with appropriate comparison and directions how to achieve an improved recovery of sonar images. The time-varying cross-range, as a challenging topic that causes sonar image smearing, was additionally analyzed, as a complex parameter in the analysis of such signals. Gathering of real data and their reconstruction helped further justification of the presented analysis.

- **Sparse decomposition of signals in dispersive channels** – A novel approach to the decomposition of signals received in the dispersive channel is introduced. The method is based on the time-frequency representations derived from polynomial extension of Fourier transform. High-resolution and model-based techniques are considered for the analysis of received signals in such channels.

The methods presented for sonar imaging can be applied to general problems in image processing. A method for denoising and reconstruction of sparse images based on a gradient-descent algorithm is developed as an example. Unlike common image reconstruction methods, the advantage of this method is that the uncorrupted pixels remain unchanged in the reconstruction process. The noisy pixels are blindly detected and reconstructed using compressive sensing approach by assuming (and not explicitly imposing) the image sparsity.

The thesis is organized as follows. The background theory on signal processing and the compressive sensing theory are presented in Chapter 2. The analysis of nonsparsity, together is presented in Chapter 3. Chapter 4 presents the analysis of different sequences and their application in compressive sensing, for a successful reconstruction of sonar signals. The background of shallow water environment, together with the techniques for sparse decomposition of the received signals in dispersive channels is analyzed in Chapter 5. Additional work on the topic of image denoising using compressive sensing techniques is introduced in the Chapter 6. Chapter 7 concludes the thesis, with the brief description of presented results and discussion on future work.

Chapter 1

Background theory

Contents

Signal processing, as such, was introduced in the 1960s, and became one of the most important tools for the analysis of signals and corresponding information. Although introduced in the 20th century, the basics on which the analysis lies are known mathematical formulations for many centuries earlier. Its use is mostly related to the introduction of computers we know today (such as the Fourier series and transform). However, due to their rapid development, the digitalization of the world is inevitable. The data which should be stored became massive. That is why the techniques developed earlier are helpful, yet not enough. In recent years, it has be seen that numerous signals are of sparse nature in a specific representation domain. New technologies have been introduced, based on compressing those signals and trying to keep the original information in their full meaning. These technologies can be summarized under the theory of compressive sensing, which is based on sparse signal processing.

In this Chapter the fundamental theory and notations used throughout this thesis are presented. The basics of signals and their representations in a transformation domain are introduced with the method of time-varying signals. It also introduces the background of compressive sensing and sparse signal processing. A basic yet effective reconstruction algorithm, which will be used through the thesis, is explained. Finally, the conditions necessary for a successful and unique reconstruction of sparse signals are presented.

1.1 Signal representation

Consider a time-domain signal $x(t)$ of duration T_s. Its samples $x(n\Delta t)$ are within the sampling interval $\Delta t = T_s/N$. The sampling interval satisfies the traditional sampling theorem. The traditional sampling theorem was introduced in few occasions [1–4], and states that a signal can be fully recovered if its sampling frequency f_s is at least twice as high as the maximum signal frequency f_{max}, i.e.

$$f_s > 2f_{max}. \tag{1.1}$$

Any discrete one-dimensional signal $x(n) = x(n\Delta t)$ of length N, $n = 0, 1, \ldots, N-1$, can be written in the vector form as

$$\mathbf{x} = [x(0), x(1), \ldots, x(N-1)]^T, \tag{1.2}$$

where T is the transpose operation. Examples of one-dimensional signals can be found in a large number of everyday applications, including audio, speech, sonar, radar, various environment sensing and biomedical signals (such as the electrocardiogram - ECG and electroencephalogram - EEG).

The sampling theory can be extended to two-dimensional signals. Examples of two-dimensional signals are photos, radar/sonar images, biomedical images (such as magnetic resonance imaging - MRI), and many others. A two-dimensional signal of size $N \times M$ is represented in a matrix form as

$$\mathbf{x} = \begin{bmatrix} x(0,0) & x(0,1) & \cdots & x(0,M-1) \\ x(1,0) & x(1,1) & \cdots & x(1,M-1) \\ \vdots & \vdots & \ddots & \vdots \\ x(N-1,0) & x(M-1,1) & \cdots & x(N-1,M-1) \end{bmatrix}. \tag{1.3}$$

In the two-dimensional case, the sampling frequency has to satisfy the sampling relation for each considered sampling direction.

In the theory, signals are commonly analyzed and processed in a certain representation (transformation) domain. Depending on its nature, the transform is suited for a specific type of the signal. The most common transformation domains are the discrete Fourier transform (DFT), discrete wavelet transform (DWT), and discrete cosine transform (DCT). For the case of radar and sonar signals, the representation domains are related to specific sequences that will be explained along with this application field.

In general, the transformation of a one-dimensional signal from one domain to another one can be presented using the matrix relations

$$\mathbf{X} = \mathbf{\Phi x} \tag{1.4}$$

where $\mathbf{\Phi}$ is the transformation matrix and $\mathbf{X}$ is the signal transform vector

$$\mathbf{X} = [X(0), X(1), \ldots, X(N-1)]^T, \tag{1.5}$$

considering the length to be N. The inverse transform provides the relation between the transformation and the signal as

$$\mathbf{x} = \mathbf{\Psi X} = \mathbf{\Phi}^{-1}\mathbf{X} \tag{1.6}$$

with the common orthonormal transformation domains relation $\mathbf{\Phi}^{-1} = \mathbf{\Phi}^H$, where H is the complex-conjugate and transpose (Hermitian) matrix. In general, the full transformation and inverse transformation matrices are given by

$$\mathbf{\Phi} = \begin{bmatrix} \phi_0(0) & \phi_1(0) & \cdots & \phi_{N-1}(0) \\ \phi_0(1) & \phi_1(1) & \cdots & \phi_{N-1}(1) \\ \vdots & \vdots & \ddots & \vdots \\ \phi_0(N-1) & \phi_1(N-1) & \cdots & \psi_{N-1}(N-1) \end{bmatrix}, \tag{1.7}$$

and

$$\mathbf{\Psi} = \begin{bmatrix} \psi_0(0) & \psi_1(0) & \cdots & \psi_{N-1}(0) \\ \psi_0(1) & \psi_1(1) & \cdots & \psi_{N-1}(1) \\ \vdots & \vdots & \ddots & \vdots \\ \psi_0(N-1) & \psi_1(N-1) & \cdots & \psi_{N-1}(N-1) \end{bmatrix}. \tag{1.8}$$

These matrices depend on the type of the transformation used for a particular signal.

1.1.1 Discrete Fourier transform (DFT)

The most frequently used transformation domain in the field of signal processing is the discrete Fourier transform, named after the mathematician Joseph Fourier (1768–1830). The basis functions are harmonic signals, allowing analysis of signals in the corresponding spectral domain. The DFT form, for a discrete-time signal $x(n)$, is given by

$$X(k) = \sum_{n=0}^{N-1} x(n)\phi_k(n) = \sum_{n=0}^{N-1} x(n)e^{-j2\pi nk/N}. \tag{1.9}$$

Its inverse is

$$x(n) = \frac{1}{N}\sum_{k=0}^{N-1} X(k)\psi_n(k) = \frac{1}{N}\sum_{k=0}^{N-1} X(k)e^{j2\pi nk/N}. \tag{1.10}$$

Note that the relation between the DFT and the inverse DFT coefficients is given by $\psi_n(k) = \phi_k^*(n)/N$ or $\mathbf{\Psi} = \mathbf{\Phi}^H/N$.

The two-dimensional extension of the DFT is defined by

$$X(k,l) = \sum_{n=0}^{N-1}\sum_{m=0}^{M-1} x(n,m)e^{-j2\pi nk/N}e^{-j2\pi ml/M} \tag{1.11}$$

with the corresponding inverse transform

$$x(n,m) = \frac{1}{N}\frac{1}{M}\sum_{k=0}^{N-1}\sum_{l=0}^{M-1} X(k,l)e^{j2\pi nk/N}e^{j2\pi ml/M}. \tag{1.12}$$

The transformation coefficients $e^{-j2\pi nk/N}e^{-j2\pi ml/M}$ are four-dimensional, since they depend on four indices (n, m, k, l). In order to use the standard derivations and optimization algorithms, as well as for notation simplification, the two-dimensional signals and transformation matrices are commonly rearranged into column matrices by layering its columns after each other in a way that

$$x(n + N(m - 1)) = x(n, m), \tag{1.13}$$

$$X(k + M(l - 1)) = X(k, l), \tag{1.14}$$

where $n = 0, 1, \ldots, N - 1$, $m = 0, 1, \ldots, M - 1$, $k = 0, 1, \ldots, N - 1$, and $l = 0, 1, \ldots, M - 1$. Then, the four-dimensional transformation forms of coefficients are rewritten as large two-dimensional matrices.

1.1.2 Time-varying signals

The signals whose spectral content change happens through time, are considered as time-varying or non-stationary signals [5–7]. Audio signals or signals transmitted through a dispersive channel are representative examples of time-varying signals. For their analysis, more complex transforms than the standard DFT must be used. These transforms should adapt for signal changes in both time and frequency domain, simultaneously.

Consider a time-varying signal $x(n)$ with C components,

$$x(n) = \sum_{c=1}^{C} x_c(n), \tag{1.15}$$

where $x_c(n)$, $c = 1, 2, \ldots, C$, are the non-stationary signals. Commonly, time-varying signals are localized in time by using a window function defined by $w(n_w)$. The basic linear time-frequency representation is a direct extension of the DFT of a windowed signal, and it is referred to as the short-time Fourier transform (STFT). It is calculated as the standard DFT applied to the windowed signal around the instant n. That is, the signal $x(n + n_w)$ at n (and around it) is multiplied by a window $w(n_w)$. Its DFT is then found as

$$S_{STFT}(n, k) = \mathrm{DFT}\{x(n + n_w)w(n_w)\} = \sum_{n_w=-N_w/2}^{N_w/2-1} x(n + n_w)w(n_w)e^{-j2\pi n_w k/N_w} \tag{1.16}$$

positioned at an instant n, a frequency k, windowed by $w(n_w)$ of length N_w. The window function can be a rectangular, Hamming, Hanning, or any other window introduced in the literature [8]. The indices n_w that vary from $-N_w/2$ to $N_w/2 - 1$ will be used. Similar results would be obtained when the index values vary from 0 to $N_w - 1$ (due to the DFT periodicity). If the STFT, for a given instant n, is arranged into a vector form, the coefficients can be denoted by $\mathbf{S}_{STFT}(n)$.

The STFT represents a simple and robust tool for time-varying signal analysis. As mentioned, the main difference from the standard DFT is in introducing the time localization

window. If this window is narrow, then more localized properties in the time domain, around the considered instant n, are obtained. However, narrow windows have poor frequency resolution, meaning that a compromise should be made. Many efforts have be done in literature to find the optimal window width for a given signal which would produce a good localization in the time domain, with a sufficiently high frequency resolution. For more complex signals, with fast changes of the spectral content, a suitable window can be found using, for example, the approach presented in [9]. In order to elevate the resolution problem more sophisticated quadratic representations are introduced in time-frequency analysis. The goal of those representations is to track spectral changes more accurately, preferably without using a localization window.

The most prominent representation of quadratic time-frequency representations is the Wigner distribution whose discrete-time form is calculated as

$$S(n,k) = 2 \sum_{n_w=-N/2}^{N/2} x(n+n_w)x^*(n-n_w)e^{-j4\pi n_w k/N}. \tag{1.17}$$

It can track linear changes in the frequency of signal components without any window. In order to limit the computation interval, a window is introduced in this distribution as well. This distribution is then defined as the pseudo Wigner distribution (PWD) of the form

$$S_{PWD}(n,k) = 2 \sum_{n_w=-N/2}^{N/2} w(n_w/2)w(-n_w/2)x(n+n_w)x^*(n-n_w)e^{-j4\pi n_w k/N}. \tag{1.18}$$

Although a window is present (as in the case of STFT), its only purpose in PWD is to limit the calculation interval. This means that the window is not crucial for the spectral localization of the presentation. For such reasons, the PWD is used for signals with fast spectral variations. However, the PWD is a quadratic distribution since it is calculated as the DFT of the product $x(n+n_w/2)x^*(n-n_w/2)$. For a multicomponent signal, we will have the product of different components $x_c(n+n_w/2)x_s^*(n-n_w/2)$ for $c \neq s$. The DFT of these products will appear in the time-frequency representation as new components (cross-terms) and can sometimes overlap with desirable auto-terms.

A simple way to keep the good properties of the PWD, while avoiding or reducing cross-terms can be achieved by using the S-method (SM)

$$S_{SM}(n,k) = \sum_{p=-L_{SM}}^{L_{SM}} S_{STFT}(n,k+p)S_{STFT}^*(n,k-p) \tag{1.19}$$

where $2L_{SM}+1$ is the width of the window in the spectral domain. Two of the most widely used representations (STFT and PWD) can be obtained from the S-method as its special cases [9]. That is, when $L_{SM} = 0$, the squared modulus of the standard STFT (i.e. spectrogram), is

$$S_{spectrogram}(n,k) = |S_{STFT}(n,k)|^2, \tag{1.20}$$

while for $2L_{SM} + 1 = N_w$ the standard PWD is obtained. The optimal representation is obtained by adding the terms for $p = 0, \pm 1, \pm 2, \ldots$ which improve the representation from the

STFT toward the PWD, until the cross-terms start to appear [9]. This effect can be detected by using measures of concentration of time-frequency representations. One such measure was based on norm-one and was introduced for measuring and optimizing time-frequency representation finding the minimum of

$$||S_{STFT}(n,k)||_1 = \sum_{k=0}^{N-1} |S_{STFT}(n,k)| \tag{1.21}$$

with respect to the window length. In this case

$$\min_{N_w,L_{SM}} ||S_{SM}(n,k)||_1 \tag{1.22}$$

produces optimal representation. It is interesting to note that this kind of minimization is used in compressive sensing for sparse signal reconstruction [10–13]. This will be reviewed in the next section.

1.2 Compressive sensing and sparse signal processing

Many signals in the nature exhibit sparsity property in a transformation domain. This fact brought the idea of developing the compressive sensing technique, which was introduced in data processing as such by Donoho, Candes, and Baraniuk [14–18].

A signal wtih small number of nonzero component, in comparison to the total length of the signal, in a transformation domain is described as sparse. It is defined by Definition 1.1.

Definition 1.1
*A signal $x(n)$ of length N is K-**sparse** in a transformation domain if it consists of K nonzero components in the corresponding domain, $K \ll N$, at positions $\mathbb{K} \in \{k_1, k_2, \ldots, k_K\}$, and zero-valued components everywhere else,*

$$X(k) = \begin{cases} A_k \neq 0, & \text{for } k \in \mathbb{K} \\ 0, & \text{otherwise} \end{cases} \tag{1.23}$$

where A_k are the amplitudes of the components at positions $k \in \mathbb{K}$.

1.2.1 Measurements of sparse signals

Unlike the traditional sampling theorem, one of the main advantages of sparse signal processing is that such signals can be recovered using a reduced number of N_A observations. The measurements are defined in Definition 1.2.

Definition 1.2
A measurement of sparse coefficients $X(k)$, $k = 0, 1, \ldots, N-1$, is obtained as their linear combination

$$y(i) = \sum_{k=0}^{N-1} a_k(i) X(k), \tag{1.24}$$

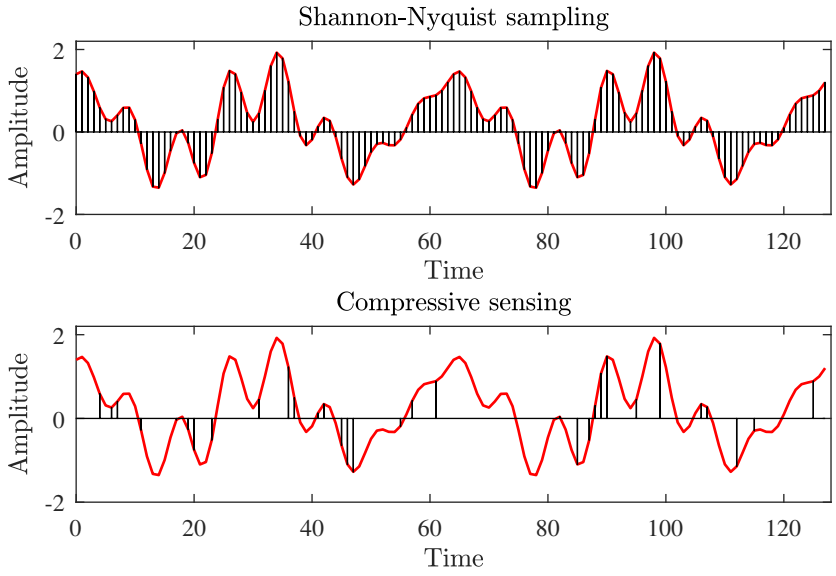

Figure 1.1: The difference betweeen traditoinal sampling theorem and compressive sensing: traditional Shannon-Nyquist sampling (top); compressive sensing sampling (bottom).

where $a_k(i)$, $k = 0, 1, \ldots, N-1$, *are the weighting coefficients for the* i*-th measurement,* $i = 0, 1, \ldots, N_A - 1$.

The aim of recovering sparse signals with a reduced set of samples/measurements/observations had a wide range of interest in the recent literature [19–23]. The theory stating this fact is known as compressive sensing (CS), developed under the framework of sparse signal processing (SSP). Notice that we can relate the general form of measurements, defined by (1.24), with signal samples defined by (1.10). Comparing these two relations, we can state that a signal sample, at one instant n_i, can be seen as the measurement of $X(k)$ with

$$y(i) = x(n_i) = \sum_{k=0}^{N-1} e^{-j2\pi n_i k/N} X(k), \tag{1.25}$$

where the weighting coefficients are the DFT transform coefficients, i.e.

$$a_k(i) = e^{-j2\pi n_i k/N}. \tag{1.26}$$

A reduced set of measurements, within this context, can be considered as the reduced number of signal samples. The difference between the sampling by the traditional sampling theorem and by compressive sensing is shown in Fig. 1.1, where only $N_A = 32$ samples are used for the analysis, instead of the full set of measurements $N = 128$.

The main objective of CS and SSP is to desirably reduce the number of acquisition samples/observations/measurements used for the signal sensing, transmission, and storying. Besides that, the small number of available measurements or signal samples can be the consequence of other physical restrictions in the considered system. It could also be a result of

unavailable samples due to high corruption of some signal samples or parts of the signal. All of these scenarios will be considered in the thesis, since the formal mathematical framework is similar.

1.2.2 Measurement matrix

The measurement matrix consists of the coefficients used to form measurements of a sparse signal with elements $X(k)$. In the case that the signal samples are used as the measurements, the measurement matrix is defined based on the transformation matrix for the considered domain of the signal sparsity.

The N_A available samples $y(i)$ at the positions defined by the set

$$\mathbb{N}_{\mathbb{A}} = \{n_1, n_2, \ldots, n_{N_A}\},$$

can be written as

$$\mathbf{y} = [y(0), y(1), \ldots, y(N_A - 1)]^T = [x(n_0), x(n_1), \ldots, x(n_{N_A-1})]^T. \tag{1.27}$$

The measurements, which are the linear combinations of the inverse transform coefficients, are presented in a matrix form as

$$\mathbf{y} = \mathbf{A}\mathbf{X}, \tag{1.28}$$

where $\mathbf{A}$ is a measurement matrix of size $N_A \times N$ obtained by keeping the rows of the inverse transformation matrix $\mathbf{\Psi}$, which correspond to the instants n_i, $i = 0, 1, \ldots, N_A - 1$, of the available samples/measurements

$$\mathbf{A} = \begin{bmatrix} \psi_0(n_0) & \psi_1(n_0) & \cdots & \psi_{N-1}(n_0) \\ \psi_0(n_1) & \psi_1(n_1) & \cdots & \psi_{N-1}(n_1) \\ \vdots & \vdots & \ddots & \vdots \\ \psi_0(n_{N_A-1}) & \psi_1(n_{N_A-1}) & \cdots & \psi_{N-1}(n_{N_A-1}) \end{bmatrix}. \tag{1.29}$$

Using the notation $a_k(i) = \psi_k(n_i)$ we can write a more general form of the measurement matrix as

$$\mathbf{A} = \begin{bmatrix} a_0(0) & a_1(0) & \cdots & a_{N-1}(0) \\ a_0(1) & a_1(1) & \cdots & a_{N-1}(1) \\ \vdots & \vdots & \ddots & \vdots \\ a_0(N_A - 1) & a_1(N_A - 1) & \cdots & a_{N-1}(N_A - 1) \end{bmatrix}. \tag{1.30}$$

Depending on the particular application, several measurement matrices other than the partial DFT, are frequently used in compressive sensing. An example of a widely used measurement matrix is the Gaussian measurement matrix, where the weighting coefficients are the Gaussian distributed random numbers

$$a_k(i) \sim \mathcal{N}(0, 1/N_A), \tag{1.31}$$

with zero mean and variance $1/N_A$. The weighting coefficients can also be uniformly distributed random numbers, or random numbers assuming values $+1$ or -1 (i.e. Bernoulli measurement matrix).

Note that randomness is a desirable property of the measurement matrices. Considering the DFT, the randomness can be increased by sampling the signal at an arbitrary instant t_i instead of the regularly defined Nyquist samples at $i\Delta t$. This case will be also examined.

1.2.3 Problem formulation

In the mathematical sense, the objective of the CS based approach is to reconstruct the N unknown elements of a sparse signal using only the $N_A < N$ available samples $\mathbf{y}$. Reduction in the number of available measurements will result in a system of N_A equations, whose matrix form is $\mathbf{AX} = \mathbf{y}$. Since there are $N > N_A$ unknown variables in $\mathbf{X}$, the system is under-determined and cannot be solved uniquely, without additional constraints.

The primary and most crucial constraint in CS is that the signal is sparse. If this constraint is satisfied, the solution is obtained by minimizing the sparsity of the signal $\mathbf{X}$, given the measurement equations. Firstly, in order to minimize the sparsity, the sparsity measure must be defined. The most straightforward sparsity measure is the L_0-norm, which counts the nonzero values in the transformation domain. The L_0-norm of $\mathbf{X}$ with K nonzero elements is

$$\|\mathbf{X}\|_0 = K. \tag{1.32}$$

The problem formulation, using the L_0-norm, is then

$$\min \|\mathbf{X}\|_0 \quad \text{subject to} \quad \mathbf{y} = \mathbf{AX}. \tag{1.33}$$

This is a direct and basic way to minimize sparsity. However, it is an NP-hard (NP – non-deterministic polynomial-time) combinatorial problem. Also, it is sensitive to noise and not feasible for computational purposes, having $\binom{N}{K}$ possible combinations for a viable solution. This is why more practical cases, such as the closest convex cost function, the L_1-norm, are used

$$\min \|\mathbf{X}\|_1 \quad \text{subject to} \quad \mathbf{y} = \mathbf{AX}. \tag{1.34}$$

In theory, it has been proved that the minimization of the L_1-norm will have the same solution as the minimization of the L_0-norm following particular conditions [24]. The L_1-norm minimization allows the application of linear programming methods for convex function minimization.

1.3 Problem solutions

The CS theory has produced a vast number of methods to find the unique solution to the previously stated problem. These can be divided into three broad groups of algorithms minimizing the signal sparsity:

- L_0-based reconstruction algorithms, solving Eq. (1.33), such as
  - Orthogonal matching pursuit (OMP) [25–27],
  - Compressive sampling matching pursuit (CoSaMP) [28],
- L_1-based reconstruction algorithms, solving Eq. (1.34), such as
  - LASSO minimization [29–32],
  - Gradient-based reconstruction [33, 34]
  - Total variations [35–37],
  - Iterative hard thresholding (IHT) [38–40].
- Bayesian-based reconstruction [41, 42].

The summary of some of these algorithms can be found in Appendix 1. In the next subsection, the OMP and its iterative extension will be further detailed.

1.3.1 Reconstruction algorithm

In all reconstruction methods, the initial estimate plays a crucial role. It is not only a starting point for all of them, but contains information about the solution existence as well. The initial estimation gives a good insight of the reconstruction performance which could be expected.

Initial estimate

The available samples (measurements) are used to estimate the initial values of the sparse coefficients $X(k)$, $k = 0, 1, 2, \ldots, N$. The values of the initial estimate will be denoted by $X_0(k)$, $k = 0, 1, 2, \ldots, N$, or in a vector form as $\mathbf{X}_0$. The initial estimate can be considered as a back-projection of the measurements to the matrix $\mathbf{A}$,

$$\mathbf{X}_0 = \mathbf{A}^H \mathbf{y}. \tag{1.35}$$

The elements of this initial estimate can be written as

$$X_0(k) = \sum_{i=0}^{N_A-1} a_k(i) y(i). \tag{1.36}$$

From Eq. (1.35), using $\mathbf{y} = \mathbf{A}\mathbf{X}$, the relation between the initial estimate with the true coefficients (the actual solution of our problem) is

$$\mathbf{X}_0 = \mathbf{A}^H \mathbf{A} \mathbf{X}. \tag{1.37}$$

Note that if $\mathbf{A}^H\mathbf{A}$ is an identity matrix, i.e., $\mathbf{A}^H\mathbf{A} = \mathbf{I}$, then the initial estimate would be equal to the correct coefficients $\mathbf{X}$, resulting in the solution of our problem. However, this is

impossible to achieve when a reduced set of measurements is available (when the measurement matrix is of size $N_A \times N$). The off-diagonal elements in the matrix $\mathbf{A}^H\mathbf{A}$ cannot be zero. The maximal value of these elements, denoted by μ (discussed later in Section 1.3.2.), satisfies the Welch upper bound [43, 44], meaning that

$$\mu \geq \sqrt{\frac{N - N_A}{N_A(N-1)}}. \tag{1.38}$$

From this inequality, we see that the maximal off-diagonal element must be greater than zero when $N_A < N$. Only if all signal samples are available (when $N_A = N$), then it is possible to get the bound equal to zero and $\mathbf{A}^H\mathbf{A} = \mathbf{I}$. This is an expected result when the reconstruction process reduces to the inverse signal transform. Then, the measurements would be equal to the full set of signal samples $\mathbf{y} = \mathbf{x}$.

Since the properties of the initial estimate will be crucial throughout this thesis, its form for a sparse signal will be presented in detail. The measurements in (1.24) for a sparse signal with nonzero coefficients $X(k)$ at $k \in \{k_1, k_2, \ldots, k_K\} = \mathbb{K}$, can be written as

$$y(i) = \sum_{l=1}^{K} a_{k_l}(i) X(k_l), \tag{1.39}$$

The initial estimate elements from (1.36) is of the form

$$X_0(k) = \sum_{i=0}^{N_A-1} a_k(i) y(i) = \sum_{i=0}^{N_A-1} a_k(i) \Big(\sum_{l=1}^{K} a_{k_l}(i) X(k_l) \Big) \tag{1.40}$$

or, by changing the order of summation,

$$X_0(k) = \sum_{l=1}^{K} X(k_l) \Big(\sum_{i=0}^{N_A-1} a_k(i) a_{k_l}(i) \Big) = \sum_{l=1}^{K} X(k_l) \mu(k, k_l), \tag{1.41}$$

where

$$\mu(k, k_l) = \sum_{i=0}^{N_A-1} a_k(i) a_{k_l}(i). \tag{1.42}$$

This relations will be used for the analysis of the reconstruction accuracy. Note that the value of $\mu(k, k_l)$ is equal to the element of matrix $\mathbf{A}^H\mathbf{A}$ at the position (k, k_l).

OMP reconstruction algorithm

For most of the presented results, an iterative variant of the OMP reconstruction algorithm [19, 28], will be used. This algorithm belongs to the group of implicit zero-norm minimization solutions, since it is based on counting and minimizing the number of nonzero elements in $X(k)$. Most of the results presented in the thesis are valid for other CS algorithms as far the conditions for unique reconstruction are satisfied.

The reconstruction algorithm is implemented in two main steps:

1. estimation of the set of positions $\mathbb{K}$ of the nonzero components in $\mathbf{X}$, and
2. reconstruction of the element $X(k)$ values using the measurements/available samples with the estimated nonzero positions.

In order to find the positions of nonzero elements, the initial estimate from (1.35) is calculated and used. Two of the methods are considered, an one-step reconstruction and the iterative version of this algorithm. Note that, the hardware realization of the algorithm in the Field Programmable Gate Arrays (FPGA) circuit is shown in [45]. More architectures for CS methods can be used, as presented in [46, 47].

One-step OMP

The simplest case is when we can expect that the number nonzero coefficients of the initial estimate $X_0(k)$ at $k \in \mathbb{K}$ are notably greater in comparison to all other elements at $k \notin \mathbb{K}$. In this case, matrix $\mathbf{A}^H\mathbf{A}$ should be such that $\mathbf{X}_0$ contains K coefficient much higher than the other coefficients. The position detection of the nonzero component is done by finding the positions of the K largest components in $\mathbf{X}_0$, that is

$$\mathbb{K} = \{k_1, k_2, \dots k_K\} = \arg\{\max|\mathbf{X}_0|\}. \tag{1.43}$$

Taking the positions of the$K$ largest components forming the set $\mathbb{K}$ in (1.35) the amplitude reconstruction is performed. As it has been stated before, if $\mathbf{A}^H\mathbf{A}$ were an identity matrix, $\mathbf{X}_0$ would be identical to the exact solution $\mathbf{X}$. However, with a reduced set of samples, the Welch lower bound prevents this. Nevertheless, it is important to achieve that the diagonal elements of $\mathbf{A}^H\mathbf{A}$ are more significant regarding the other non-diagonal elements.

For the second part of the algorithm, let consider that all K positions are found correctly. Then, the values in $X(k)$ at $k \notin \{k_1, k_2, \dots, k_K\}$ are set to zero, and the vector $\mathbf{X}_K = [X(k_1), X(k_2), \dots, X(k_K)]^T$ is with unknown nonzero values that should be found (reconstructed). Note that this assumption transforms the initial under-determined system $\mathbf{y} = \mathbf{A}\mathbf{X}$ with N_A equations and N unknowns in $\mathbf{X}$ to an over-determined system of N_A equations with K unknowns $(X(k_1), X(k_2), \dots, X(k_K))$. The new set of equations now reads

$$\mathbf{y} = \mathbf{A}_K\mathbf{X}_K. \tag{1.44}$$

This system can be solved for the nonzero spectral values $\mathbf{X}_K$ at the estimated positions $\mathbb{K}$. The matrix $\mathbf{A}_K$ is an $N_A \times K$ sub-matrix of $\mathbf{A}$, keeping only the columns of the nonzero elements positions in $X(k)$

$$\mathbf{A}_K = \begin{bmatrix} a_{k_1}(0) & a_{k_2}(0) & \cdots & a_{k_K}(0) \\ a_{k_1}(1) & a_{k_2}(1) & \cdots & a_{k_K}(1) \\ \vdots & \vdots & \ddots & \vdots \\ a_{k_1}(N_A-1) & a_{k_2}(N_A-1) & \cdots & a_{k_K}(N_A-1) \end{bmatrix}. \tag{1.45}$$

The smallest number of measurements needed to recover K coefficients at the known positions is $N_A = K < N$. However, for an accurate estimation of the nonzero positions,

a much larger number of measurements is needed according to the reconstruction conditions (which will be discussed in the next section). When $N_A > K$, the system is over-determined, and the solution is found in the mean squared error (MSE) sense. The solution is

$$\mathbf{X}_K = (\mathbf{A}_K^H \mathbf{A}_K)^{-1} \mathbf{A}_K^H \mathbf{y} = \text{pinv}(\mathbf{A}_K)\mathbf{y}, \tag{1.46}$$

where $\text{pinv}(\mathbf{A}_K) = (\mathbf{A}_K^H \mathbf{A}_K)^{-1} \mathbf{A}_K^H$ is a matrix $\mathbf{A}_K$ pseudo-inverse and $\mathbf{A}_K^H \mathbf{A}_K$ is called a $K \times K$ Gram matrix of $\mathbf{A}_K$.

Iterative OMP

The OMP procedure considers the criteria when the K components are larger than the initial value coefficients at originally zero-coefficient positions. That condition can be relaxed by using the iterative version of the method. In order to estimate the position of the largest nonzero component, only its value must be larger than the values at the originally zero-valued coefficient positions. The position of the largest component is found as

$$k_1 = \arg\max\{\mathbf{X}_0\}. \tag{1.47}$$

Its amplitude value is estimated using Eq. (1.46) as it were the only nonzero coefficient. It is reconstructd using the sub-matrix $\mathbf{A}_1$. Then, this component is subtracted from the measurements, i.e., $\mathbf{y} - \mathbf{A}_1\mathbf{X}_1$, and the procedure is continued by estimating the next largest coefficients with the new measurements. After the initial estimate is calculated with these samples, its largest value position is found as k_2, and the new set of two nonzero positions is formed as $\{k_1, k_2\}$. Matrix $\mathbf{A}_2$ is formed with these two positions and (1.46) is solved for $\mathbf{X}_2$. After the two largest coefficients are detected and estimated, they are removed from the measurements as $\mathbf{y} - \mathbf{A}_2\mathbf{X}_2$.

If these new measurements are equal to zero after the subtraction, it means that we have solved the problem and that signal is $K = 2$ sparse. If this not the case, the new measurements (removing the two largest coefficients) are used for the next initial estimate and the third largest coefficient position detection. The procedure is iteratively continued until some desired stopping criterion is achieved. The simplest measure for it can be that the new measurement matrix, after K steps, calculated as $\mathbf{y} - \mathbf{A}_K\mathbf{X}_K$, is equal to zero or its energy is bellow a defined small accuracy level.

1.3.2 Conditions for reconstruction

Having the condition of sparsity fulfilled, additional criteria should be satisfied for a successful and unique reconstruction with a reduced number of samples. These criteria are intensively studied and they are commonly expressed using the coherence index of a measurement matrix or the restricted isometry property (RIP) of this matrix.

Coherence index

The most widely used criterion for a successful reconstruction is based on the coherence

index of the measurement matrix $\mathbf{A}$. Consider an $N_A \times N$ measurement matrix $\mathbf{A}$ and denote its columns by vectors $\mathbf{a}_i$, $i = 0, 1, \ldots, N-1$, that is

$$\mathbf{A} = [\mathbf{a}_0, \mathbf{a}_1, \ldots, \mathbf{a}_{N-1}]. \tag{1.48}$$

The scalar product of two columns of this matrix, k and i, is defined by

$$\langle \mathbf{a}_k^H, \mathbf{a}_i \rangle = \sum_{p=0}^{N_A-1} a_i(p) a_k^*(p). \tag{1.49}$$

Notice that this product is, by definition, equal to the (k, i) element of matrix $\mathbf{A}^H\mathbf{A}$.

Definition 1.3
*The **coherence index** of a measurement matrix is defined as the maximal value of the normalized scalar product*

$$\mu = \max |\mu(i,k)| = \max \left| \frac{\langle \mathbf{a}_k^H, \mathbf{a}_i \rangle}{\langle \mathbf{a}_k^H, \mathbf{a}_k \rangle} \right| = \max \left| \frac{\sum_{p=0}^{N_A-1} a_i(p) a_k^*(p)}{\sum_{p=0}^{N_A-1} |a_i(p)|^2} \right|, \tag{1.50}$$

for $i \neq k$. For the normalized measurement matrices $\sum_{p=0}^{N_A-1} |a_i(p)|^2 = 1$, the coherence index is defined by

$$\mu = \max |\mu(i,k)| = \max \left| \langle \mathbf{a}_k^H, \mathbf{a}_i \rangle \right| = \max \left| \sum_{p=0}^{N_A-1} a_i(p) a_k^*(p) \right|. \tag{1.51}$$

This value is an important parameter in choosing the measurement matrix which will be further discussed by Statement 1.

Statement 1: A K-sparse signal can be reconstructed from the measurements in a unique way if the cohrence index of the matrix $\mathbf{A}$ satisfies the condition

$$K < \frac{1}{2}\left(1 + \frac{1}{\mu}\right). \tag{1.52}$$

A smaller coherence index means that signal with larger sparsity values K can be reconstructed. The relation can be derived considering the initial estimate as

$$X_0(k) = \sum_{l=1}^{K} X(k_l)\mu(k, k_l). \tag{1.53}$$

Without loss of generality, assume that the largest coefficient value is $X(k_1) = 1$. The largest disturbance to this coefficient estimation is if the remaning $(K-1)$ nonzero coefficients are almost equally strong, i.e., close to 1. Then the initial estimate would be

$$X_0(k) = \sum_{l=1}^{K} \mu(k, k_l). \tag{1.54}$$

Since $\mu(k,k_l) \leq \mu$, the largest possible value at the original zero coefficient position is $|X_0(k)| \leq K\mu$. At the largest coefficient position, $k = k_1$, the worst case is if all other $(K-1)$ terms are maximal (equal to μ) but with opposite sign than its value, that is $X_0(k_1)| > 1-(K-1)\mu$. The detection of the largest element is successful if its worst case initial estimate is greater than the worst case value at zero coefficient positions

$$1-(K-1)\mu > K\mu \tag{1.55}$$

Note that, if this relation is satisfied for the largest coefficient, then, after it is successfully detected, reconstructed and removed, the relation holds for the signal with lower $(K-1)$-sparsity.

Restricted isometry property (RIP)

The restricted isometry property is another way to define a condition which the measurement matrix should satisfy in order to uniquely reconstruct a signal under the CS approach.

Firstly, a K sparse signal is uniquely reconstructed if the size of the smallest nonsingular sub-matrix of $\mathbf{A}$ (spark) is such that

$$\text{spark}\{\mathbf{A}\} > 2K. \tag{1.56}$$

This condition means that all submatrices of $\mathbf{A}$ with order lower than $2K$ are nonsingular.

Statement 2: A K-sparse signal can be uniquely reconstructed using the measurement matrix $\mathbf{A}$, if the RIP condition

$$1-\delta_{2K} \leq \frac{\|\mathbf{A}_{2K}\mathbf{X}_{2K}\|_2^2}{\|\mathbf{X}_{2K}\|_2^2} \leq 1+\delta_{2K}, \tag{1.57}$$

holds for all its sub-matrices $\mathbf{A}_{2K}$ of order $2K$, where δ_{2K} is the isometric constant in the range $0 \leq \delta_{2K} < 1$. The constant δ_{2K} can be calculated as

$$\delta_{2K} = \max\{1-\lambda_{\min}, \lambda_{\max}-1\} \tag{1.58}$$

where $\lambda_{\min}$ and $\lambda_{\max}$ correspond to the minimum and the maximum eigenvalue of $\mathbf{A}_{2K}^T\mathbf{A}_{2K}$, respectively.

The RIP condition ensures that the solution of the Eq. (1.33) and Eq. (1.34) give the identical results, meaning that the results of the approximation are close to the true values [24]. It is seen that, in the case of Eq. (1.34), the isometric constant is in the range $0 \leq \delta_{2K} < \sqrt{2}-1$.

Although these conditions are fundamental for obtaining a successful and unique reconstruction of a sparse signal, it is interesting to note that they are very conservative for real-world sparse signals. Without loss of generality, we can assume that the reconstruction conditions are met and the practical guidelines are satisfied (that the number of measurements is significantly higher than the sparsity).

Chapter 2

Reconstruction error of non-stationary signals

Contents

The compressive sensing framework assumes sparse signals. However, due to their nature, many real signals (particularly non-stationary signals) are only approximately sparse or not sparse at all. Additionally, the sparsity condition can be distorted due to many other reasons. The most evident one is the additional noise in signals. Moreover, a very simple, yet an immense real-world problem, is the analysis of signals which are not on the sparsity domain grid. This includes signals which are not on grid frequencies. These signals can be analyzed and processed within the compressive sensing framework assuming that they are sparse under natural circumstances. The influence of their nonsparsity will result in the error through the reconstruction. For such signals, only the limit bounds of the reconstruction error were derived in the literature [15,24,48–50]. The main contribution of this Chapter is the calculation of the precise expected squared reconstruction error in time-varying signals. The STFT is assumed as the sparsity domain of the analysis. The reconstruction of nonsparse signals constrained with a sparsity coindition will be examined and compared to the statistical error calculation.

In the first part of the Chapter, the properties of the initial estimate in the reconstruction procedure will be explained as the basis to the error derivation. The noise in the initial estimate will be calculated on uniformly and randomly sampled signals. These results will support the error calculation in the STFT domain. The result will be generalized for cases when the signal is nonuniformly sampled [51] as a consequence of sampling jitter or intentional sampling deviations. Since most of the real systems are implemented in hardware using finite

length registers, a specific form of noise, the quantization noise, is also present in signals [52], and it will be also analyzed in this Chapter. At the end, the effect of noise folding will be considered, which will conclude the effectiveness of the error calculation in many real circumstances of signals nature.

2.1 Initial estimate analysis for uniform sampling

The initial estimate $\mathbf{X}_0$ from Eq. (1.35) is the key for deriving the exact error of an approximately sparse or nonsparse signal. It can be understood as the back-projection of the samples on the measurement matrix, which is defined as the matched filtering. It is the first important step for the analysis and reconstruction of a signal. The available data are back-projected to the measurement matrix and used in all reconstruction algorithms. Moreover, the back-projection relation contains more properties of the desired sparse signal than being used just as its initial estimate. In Section 1.3.3. it was shown that the key criteria for the signal reconstruction can be related to the back-projection relation and initial estimate (e.g. the coherence index).

The initial estimate can be rewritten as

$$X_0(k) = \sum_{n_i \in \mathbb{N}_A} x(n_i)\phi_{n_i}(k). \tag{2.1}$$

If all measurements are available, the initial estimate of an originally sparse signal $X(k)$ will be sparse and equal to the original signal transform. However, if the set of available measurements is reduced, the missing samples will produce noise in the initial estimate and cause its deviation from the original transform. Having less available samples will make the signal in the transformation domain more noisy, as illustrated in Fig. 2.1.

For an easier understanding, let us consider the STFT calculated at one instant using a rectangular window. The analysis of the transform then reduces to the DFT analysis of the signal samples within the window. For the DFT case, the Eq. (2.1) reads

$$X_0(k) = \sum_{n_i \in \mathbb{N}_\mathbb{A}} x(n_i)e^{-j2\pi n_i k/N}. \tag{2.2}$$

Firstly, let assume a simple single-component signal, i.e. $K = 1$, with amplitude A_0 at a position k_0,

$$X_0(k) = \sum_{n \in \mathbb{N}_A} A_0 e^{j\frac{2\pi}{N}(k-k_0)n}. \tag{2.3}$$

The expected value of $X_0(k)$, i.e., $E\{X_0(k)\}$, denoted by $\mu_{X_0(k)}$ is equal to

$$\mu_{X_0(k)} = A_0 \sum_{n \in \mathbb{N}_A} E\{e^{j\frac{2\pi}{N}(k-k_0)n}\}. \tag{2.4}$$

In [8, 53], it has be shown that the expected value is

$$E\{e^{j\frac{2\pi}{N}(k-k_0)n}\} = \delta(k-k_0), \tag{2.5}$$

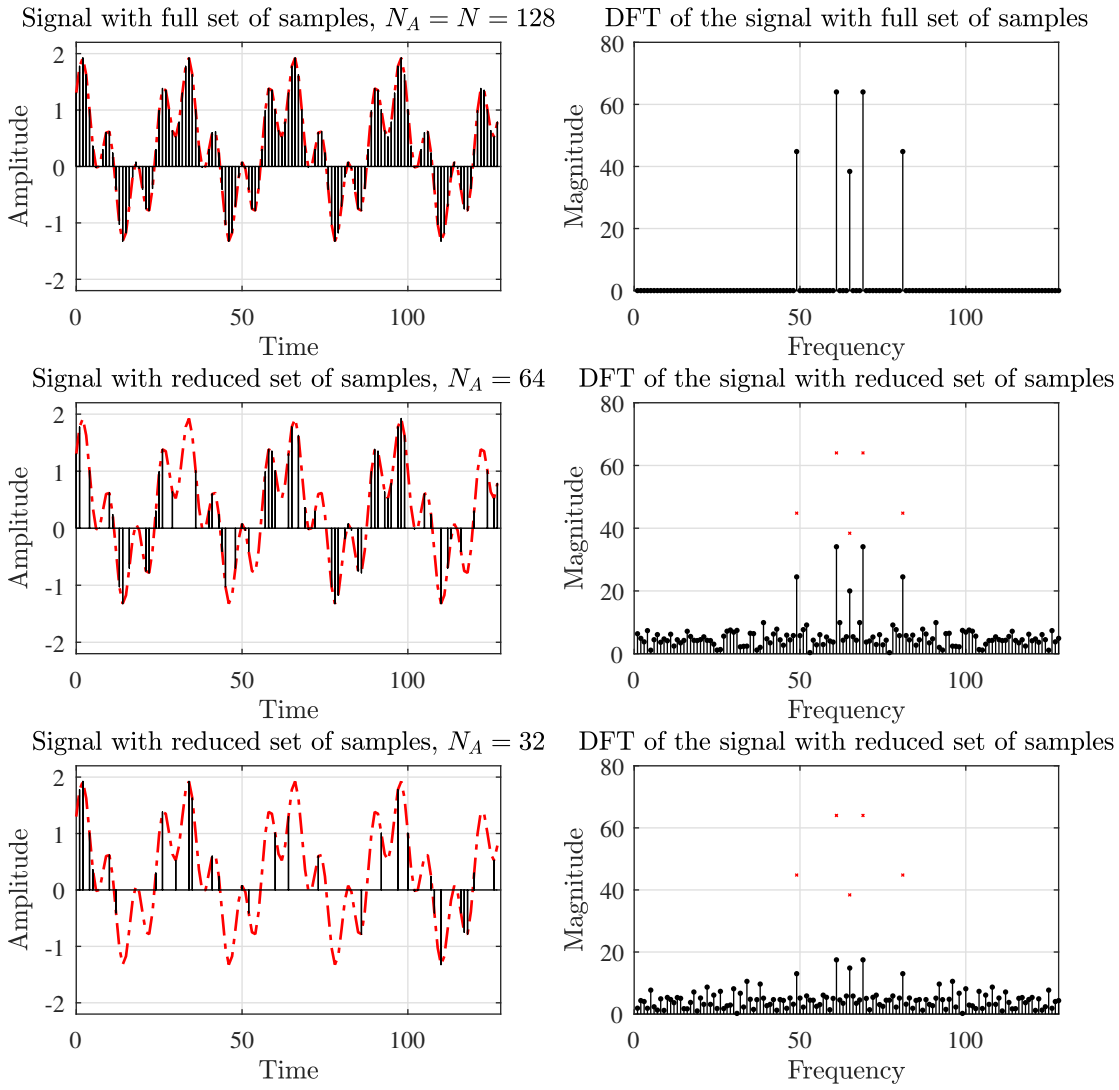

Figure 2.1: Initial estimate noise illustration: time domain (left); frequency domain (right). Top - signal with full set of measurements. Middle - signal with 50% of available samples with corresponding DFT. Bottom - signal with 25% of available measurements with corresponding spectrum. Red dots represent true values, black lines present available values.

where $\delta(k-k_0) = 1$ for $k = k_0$, and $\delta(k-k_0) = 0$ for $k \neq k_0$. Since there are N_A terms in (2.4), we get

$$\mu_{X_0(k)} = A_0 N_A \delta(k-k_0). \tag{2.6}$$

For the calculation of variance, the value at the position of the component, i.e. $k = k_0$, is $\sigma^2_{X_0(k)} = 0$. For the case when $k \neq k_0$, the variance of the initial estimate will be nonzero, while the mean value is zero. The variance is calculated using

$$\sigma^2_{X_0(k)} = \sum_{n\in\mathbb{N}_A} \sum_{m\in\mathbb{N}_A} |A_0|^2 E\left\{e^{j\frac{2\pi}{N}(k-k_0)(n-m)}\right\}. \tag{2.7}$$

It has been previously confirmed in [53] that, for random $n \neq m$ and $k \neq k_0$, variables $e^{j\frac{2\pi}{N}(k-k_0)n}$ are equally distributed, producing expectation equal to

$$E\left\{e^{j\frac{2\pi}{N}(k-k_0)(n-m)}\right\} = -\frac{1}{N-1}. \tag{2.8}$$

For $n = m$, the complex sinusoid is deterministic, and the relation $E\left\{e^{j\frac{2\pi}{N}(k-k_0)(n-m)}\right\} = 1$ holds.

Note that, in (2.7), there are N_A terms when $n = m$, and $N_A(N_A - 1)$ terms when $n \neq m$. Therefore, for $k \neq k_0$, the DFT coefficient variance becomes

$$\sigma^2_{X_0(k)} = |A_0|^2 \frac{N_A N_Q}{N-1}. \tag{2.9}$$

In the general case, i.e. when $K > 1$, the initial estimate is a summation of independent random variables

$$X_0(k) = \sum_{n\in\mathbb{N}_A} \sum_{l=1}^{K} A_l e^{j\frac{2\pi}{N}(k-k_l)n}. \tag{2.10}$$

According to (2.6), the mean value of a $K > 1$ sparse signal is then

$$\mu_{X_0(k)} = N_A \sum_{l=1}^{K} A_l \delta(k - k_l). \tag{2.11}$$

Since the random value at $k = k_l, l = p$, does not contribute to the noise, the variance of $X(k)$ will be

$$\sigma^2_{X_0(k)} = \sum_{\substack{l=1 \\ l\neq p}}^{K} N_A |A_l|^2 \frac{N_A N_Q}{N-1}. \tag{2.12}$$

This analysis can be applied on sparse time-varying signals in the joint time-frequency domain. The total variance of a STFT signal will be the average sum of the variances of each windowed instant of DFT.

2.2 Initial estimate analysis for random sampling

In some practical scenarios, signals are randomly sampled due to intentional strategy to increase randomness in sampling or due to the effect of high jitter in sampling. The jitter can be caused by lack of synchronisation, hardware or transmission problems. Random sampling affects the processing of signals under the CS framework, since the sample values are not on the grid anymore, i.e., at random positions $0 < t_n < N$. Then, the initial estimate of a signal with available samples at random positions $t_n \in \mathbb{N}_A = \{t_1, t_2, \ldots, t_{N_A}\}$ is

$$X_0(k) = \sum_{n\in\mathbb{N}_A} x(t_n) e^{-j2\pi t_n k/N}. \tag{2.13}$$

The mean value of such signal remains the same as for the uniform sampling case, i.e. the mean value is equal to the one from Eq. (2.11).

In the case of random sampling, it is interesting to notice that, unlike when the signal is uniformly sampled on the grid, the variance at the signal component of a signal will not be zero even when N signal samples are available. This will conclude that the all components in the initial estimate $X_0(k)$ are affected by a noise. The noise has a variance

$$\sigma^2_{X_0(k)} = \sum_{l=1}^{K} N_A A_l^2 [1 - \delta(k - k_l)]. \tag{2.14}$$

2.3 Error in time-frequency signal reconstruction

Intuitively, it can be seen that this idea is closely related to finding the exact error of the reconstruction of approximately sparse or nonsparse signals when they are reconstructed under the assumption that their nature is originally sparse. For a signal $x(n)$, with the corresponding transformation $X(k), k = 0, 1, \ldots, N-1$, the definitions of approximately sparse and nonsparse signals are given next.

Definition 2.1
*An **approximately sparse signal**, of length N, is a signal which consists of K significant non-zero components at $k \in \mathbb{K} = \{k_1, k_2, \ldots, k_K\}$ and $N - K$ small non-zero components $k \notin \mathbb{K}$, i.e.*

$$\min\Big\{|X(k_1)|, X(k_2)|, \ldots, |X(k_K)|\Big\} \gg \max\Big\{|X(k_{K+1})|, |X(k_{K+2})|, \ldots |X(k_{K+N})|\Big\} \tag{2.15}$$

Definition 2.2
*A **nonsparse signal**, of length N, is a signal which consists of N non-zero components of the same order of amplitude.*

Since the signal is considered as originally sparse in its nature, the reconstruction is performed under the constraint that it is K-sparse. This results that the remaining $N - K$ components, that are not reconstructed, will impact on the error of the reconstructed components. An analysis of the error in the reconstructed signal caused by this effect will be analyzed.

For the analysis, recall a time-varying $x(n)$, with a STFT of $\mathbf{S}_N(n)$, and its windowed version $x(n, n_w)$ of length N_w, as

$$S_N(n,k) = \mathrm{DFT}\{x(n+n_w)w(n_w)\} = \sum_{n_w=-N_w/2}^{N_w/2-1} x(n+n_w)w(n_w)e^{-j2\pi n_w k/N_w}. \tag{2.16}$$

Assuming sparsity K, the signal is reconstructed using the available measurements at positions $n + n_w \in \mathbb{N}_A$. Consequently, the number of missing measurements is $N_Q = N - N_A$.

Notice that using any CS reconstruction method (assuming that conditions for a successful and unique reconstruction are met), we detect and reconstruct K coefficients, with $A_l(n)$ corresponding to the reconstructed amplitudes at $k \in \mathbb{K}$. The amplitudes of the nonreconstructed components generate noise in the reconstructed coefficients $\mathbf{S}_R(n)$. The noise variance caused by the components that are not reconstructed is obtained from the variance of the initial estimate, given by Eq. (2.14) as

$$|A_l(n)|^2 \frac{N_A N_Q}{N-1}. \tag{2.17}$$

The amplitude values at the positions of the original nonzero coefficient in the initial estimate $\mathbf{S}_{N0}(n)$ are proportional to N_A. In the reconstruction process, the amplitudes should be reconstructed to their true values (i.e., when the full measurement set is available). Thus, the values of the recovered amplitudes should be proportional to N, instead of N_A. resulting in the scaling factor to be N/N_A. Therefore, the noise variance scaling factor in the reconstructed coefficients is $(N/N_A)^2$. Hence, the noise variance caused by one nonreconstructed component to the reconstructed coefficient will be

$$|A_l(n)|^2 \frac{N^2}{N_A^2} \frac{N_A N_Q}{N-1} \cong |A_l(n)|^2 N \frac{N_Q}{N_A}. \tag{2.18}$$

The noise energy in the K components of $\mathbf{S}_R(n)$ is the summation of the K variances of each reconstructed coefficient. The total energy of noise in the reconstructed coefficients generated by the $N-K$ nonreconstructed components is

$$\|\mathbf{S}_{NR}(n) - \mathbf{S}_{NK}(n)\|_2^2 = KN \frac{N_Q}{N_A} \sum_{l=K+1}^{N} |A_l(n)|^2, \tag{2.19}$$

where $\mathbf{S}_{NR}(n)$ is obtained from $\mathbf{S}_R(n)$ by adding zero values at the pisitions $k \notin \mathbb{K}$. The energy of the nonreconstructed elements in the STFT can be written as

$$\|\mathbf{S}_N(n) - \mathbf{S}_{NK}(n)\|_2^2 = \sum_{l=K+1}^{N} |NA_l(n)|^2, \tag{2.20}$$

where $\mathbf{S}_{NK}(n)$ is a signal of length N, which represents the amplitudes of $\mathbf{S}_N(n)$ at positions $\mathbb{K}$, and is zero-valued everywhere else. From (2.19) and (2.20), it can be concluded that the energy of error in the reconstructed components is proportional to the energy of the nonreconstructed components of the nonsparse signal in the form

$$\|\mathbf{S}_{NR}(n) - \mathbf{S}_{NK}(n)\|_2^2 = K \frac{N_Q}{N_A N} \|\mathbf{S}_N(n) - \mathbf{S}_{NK}(n)\|_2^2. \tag{2.21}$$

Note that, in the case when a randomly sampled signal is considered, the error is

$$\|\mathbf{S}_{NR}(t_n) - \mathbf{S}_{NK}(t_n)\|_2^2 = \frac{K}{N_A} \|\mathbf{S}_N(t_n) - \mathbf{S}_{NK}(t_n)\|_2^2. \tag{2.22}$$

If the signal is strictly sparse, we can conclude there is no reconstruction error, i.e.

$$\|\mathbf{S}_{NR}(t_n) - \mathbf{S}_{NK}(t_n)\|_2^2 = 0, \tag{2.23}$$

meaning that $\mathbf{S}_N(t_n) = \mathbf{S}_{NK}(t_n)$, whether the signal is sampled uniformly or randomly.

For uniformly sampled signal, the reconstruction error is zero-valued when all samples are available, i.e. $N_A = N$ and $N_Q = 0$.

2.3.1 Additive input noise

In a more realistic case, the received measurements are usually with some additive noise

$$\mathbf{y} + \varepsilon = \mathbf{AX}, \tag{2.24}$$

where ε is the additive noise with variance σ_ε^2. Having noisy measurements will provide that the initial estimate of the signal, $S_{N0}(t_n, k)$, is with an additional noise component as well. The variance in $S_{N0}(t_n, k)$, caused by the measurements input noise, is

$$\sigma^2_{S_{N0}(t_n,k)} = N_A\sigma_\varepsilon^2. \tag{2.25}$$

In the reconstruction process, as mentioned, the initial estimate is scaled by the factor N/N_A. The noise variance in one reconstructed component is then

$$\text{var}\{S_{NR}(t_n, k)\} = N_A\sigma_\varepsilon^2\Big(\frac{N}{N_A}\Big)^2 = \frac{N^2}{N_A}\sigma_\varepsilon^2. \tag{2.26}$$

That will result in the total MSE in K reconstructed coefficients, due to to the additive noise

$$\|\mathbf{S}_{NR}(t_n) - \mathbf{S}_{NK}(t_n)\|_2^2 = K\frac{N^2}{N_A}{\sigma_\varepsilon}^2. \tag{2.27}$$

The error energies, caused by the nonsparsity effects and the additive input noise independently, can be summed to produce a general relation for the expected squared error including both effects. The equation for the noisy and nonsparse signals case is given by [54]

$$\|\mathbf{S}_{NR}(t_n)-\mathbf{S}_{NK}(t_n)\|_2^2 = KC_K\,\|\mathbf{S}_N(t_n)-\mathbf{S}_{NK}(t_n)\|_2^2 + K\frac{N^2}{N_A}\sigma_\varepsilon^2, \tag{2.28}$$

with $C_K = N_Q/N_AN$ for uniform sampling ($t_n = n\Delta t$) and $C_K = 1/N_A$ for random sampling.

The accuracy of the theoretic result in Eq. (2.28) will be validated on different signals. The result for the error calculation will be compared with a statistically calculated error,

$$E_{statistical} = 10\log(||\mathbf{S}_{NK}(t_n) - \mathbf{S}_{NR}(t_n)||_2^2) \tag{2.29}$$

where $\mathbf{S}_{NK}(t_n)$ is the original K-sparse signal at positions $k \in \mathbb{K}$ and $\mathbf{S}_{NR}(t_n)$ is the reconstructed signal at $k \in \mathbb{K}$.

2.3.2 Error calculation examples

Example 1: Uniform sampling. Let assume a signal consisting of two main components which are linear frequency modulated (LFM)

$$x(t) = 1.3e^{j\pi\left(52\frac{t}{N}+32(\frac{t}{N})^2+2\pi\phi_1\right)} + 2.1e^{j\pi\left(4\frac{t}{N}-20(\frac{t}{N})^2+2\pi\phi_2\right)}, \tag{2.30}$$

with $N = 1024$. The values ϕ_1 and ϕ_2 are the random phases in the signal. The cases of uniform and random sampling are considered. The signal is sampled with sampling interval $\Delta t = 1$. The STFT of the signal with full set of measurements at $t = n\Delta t$ and with Hamming window of length $N_w = 256$ is presented in Fig 2.2 (top left).

A reduced number of available measurements/samples is considered next. The available samples are affected by a random Gaussian noise with zero-mean and variance $\sigma_\varepsilon = 0.1$. The STFT with the set of available samples of size $N_A = 2N/3$ is presented in Fig. 2.2 (top right). From the Figures it is seen that the signal is non-stationary, thus it is not strictly sparse. The reconstruction with sparsity level of $K = 8, 16, 32, 48$ is presented in the remaining subplots of Fig. 2.2, respectively. It is interesting to note that, by using only $K = 8$ the weakest component is not reconstructed. When $K = 16$, only few parts of the component are reconstructed. Only by using $K = 32$ or more we can get the recovery of all three components.

Using the calculation from Eq. (2.28), the theoretical error is calculated as

$$E_{theoretical} = 10\log\left(K\frac{N_Q}{N_A N}\left\|\mathbf{S}_N(n)-\mathbf{S}_{NK}(n)\right\|_2^2 + K\frac{N^2}{N_A}\sigma_\varepsilon^2\right). \tag{2.31}$$

The total reconstruction error assuming different number of available measurements N_A and various sparsities K is illustrated in Fig. 2.3. The results are averaged in 100 realizations. The statistical error is presented with the dots, while the theoretical error is shown with lines. The filled dots present that the reconstruction is performed successfully with high probability. In this case, the condition to consider a successful reconstruction is when $N_A > 4K$.

Example 2: Random sampling. Assume a LFM signal with three main components

$$x(t) = x_1(t) + x_2(t) + x_3(t) \tag{2.32}$$

where

$$x_1(t) = 0.7e^{j\pi\left(52\frac{t}{N}+32(\frac{t}{N})^2+2\pi\phi_1\right)} \tag{2.33}$$

$$x_2(t) = 1.3e^{j\pi\left(113\frac{t}{N}+46(\frac{t}{N})^2+2\pi\phi_2\right)} \tag{2.34}$$

$$x_3(t) = e^{j\pi\left(446\frac{t}{N}-54(\frac{t}{N})^2+2\pi\phi_3\right)} \tag{2.35}$$

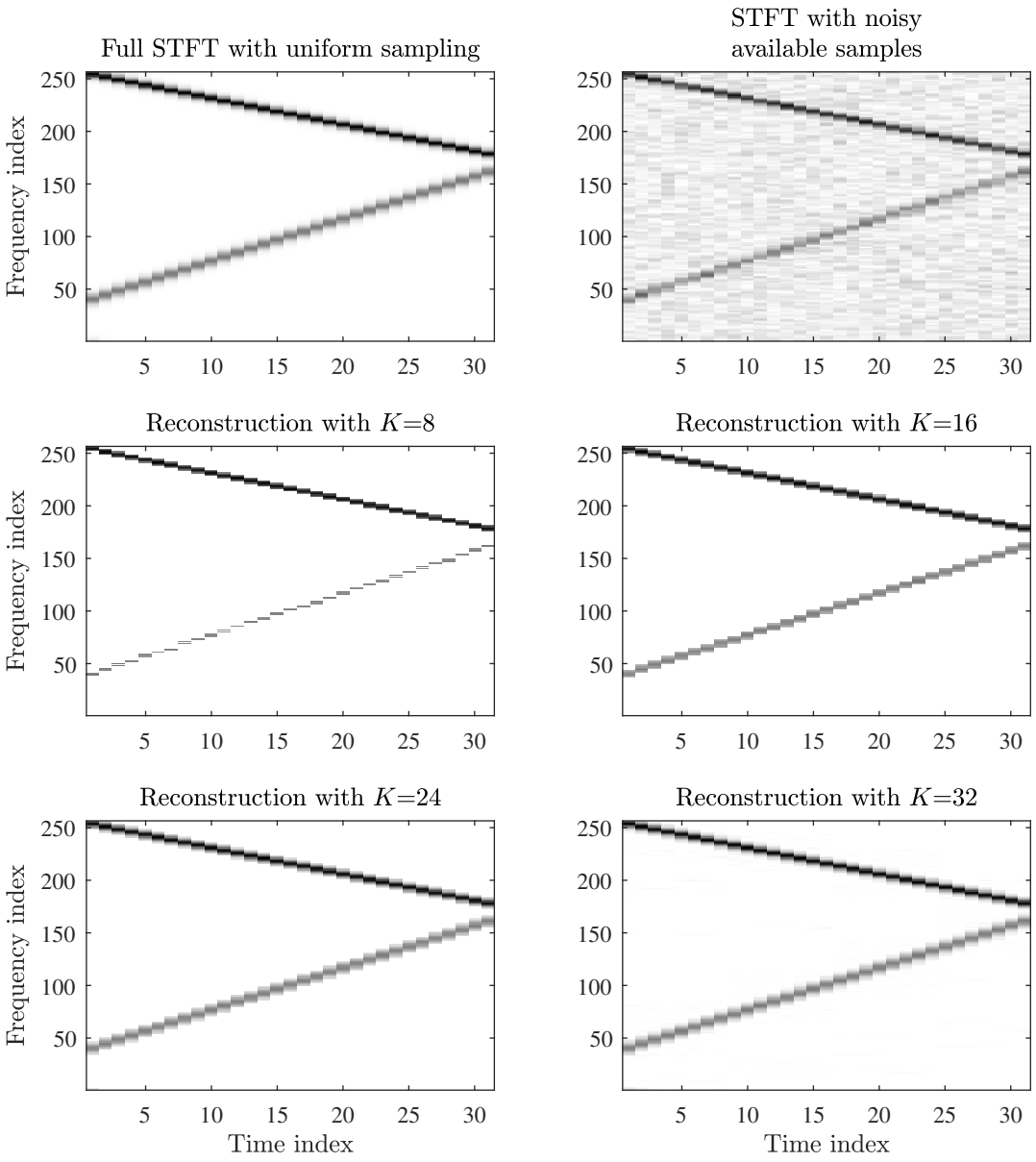

Figure 2.2: Sparse STFT reconstruction when signal is uniformly sampled: STFT with the full set of measurements (top left); STFT with the reduced set of noisy measurements with variance $\sigma_\varepsilon = 0.1$ (top right), the reconstruction with $K = 8, 16, 32, 48$ (remaining subplots).

with $N = 1024$ and random phases ϕ_1, ϕ_2, and ϕ_3.

In this case, a random set of N_A available samples at $0 \leq t_n \leq 1024$ is considered. The STFT, when the full set of measurements is considered, is shown in 2.4 (top left). It can be observed that random sampling of the signal adds to the nonsparsity of the signal, together with the reduced number of available samples, Fig. 2.4 (top right). The signal is reconstructed with assumed sparsity levels of $K = 16, 24, 32, 48$.

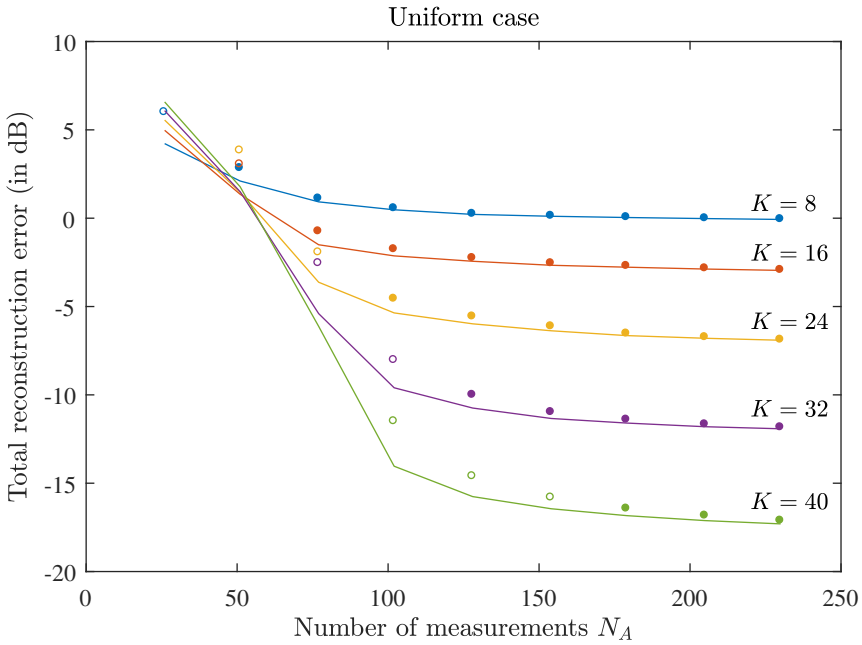

Figure 2.3: Total averaged reconstruction error asuming different number of available measurements N_A and various sparsity levels K. The error is averaged over 300 realizations. The signal is uniformly sampled. Lines present the theoretical results, while the dots are the statistical values. The filled dots show when the recovery is performed with a high probability, i.e. for $N_A > 4K$.

Using the calculation from Eq. (2.28), the theoretical error is

$$E_{theoretical} = 10 \log \left((\frac{K}{N_A} + 1) \, \|\mathbf{S}_N(n) - \mathbf{S}_{NK}(n)\|_2^2 + K \frac{N^2}{N_A} \sigma_\varepsilon^2 \right). \tag{2.36}$$

The total reconstruction error when $N_A = N/2, 2N/3, 3N/4$ is presented in Table 2.1. The total error is averaged in 100 realizations. The statistical results are presented with dots, and the theoretical error is presented with the lines. The filled dots present the results when the reconstruction success is of high probability. Note that the error in the random sampling case is larger than the one received in the uniform case. It is due to the fact that it causes higher nonsparsity than in the uniform sampling. Additionally to that, noise increases the nonsparsity in the signals. Our goal, however, is to find the exact error which is produced by the reconstruction. The statistical and the theoretical error show high agreement in the reconstruction, proving the exactness of the derivation.

Example 3: Application on audio signals. The audio signal "Train", included in the MATLAB software, is considered. Its original STFT, with full set of samples, is presented in Fig. 2.5 (top left). The STFT is perormed using a Hanning window with a 50% overlap, which allowes simple and direct reconstruction of the audio signal. Assume that the sparsity of the signal is $K = 55$ and that only half of the measurements are available. The STFT of the signal with the available set of measurements is presented in Fig. 2.5 (top right). The

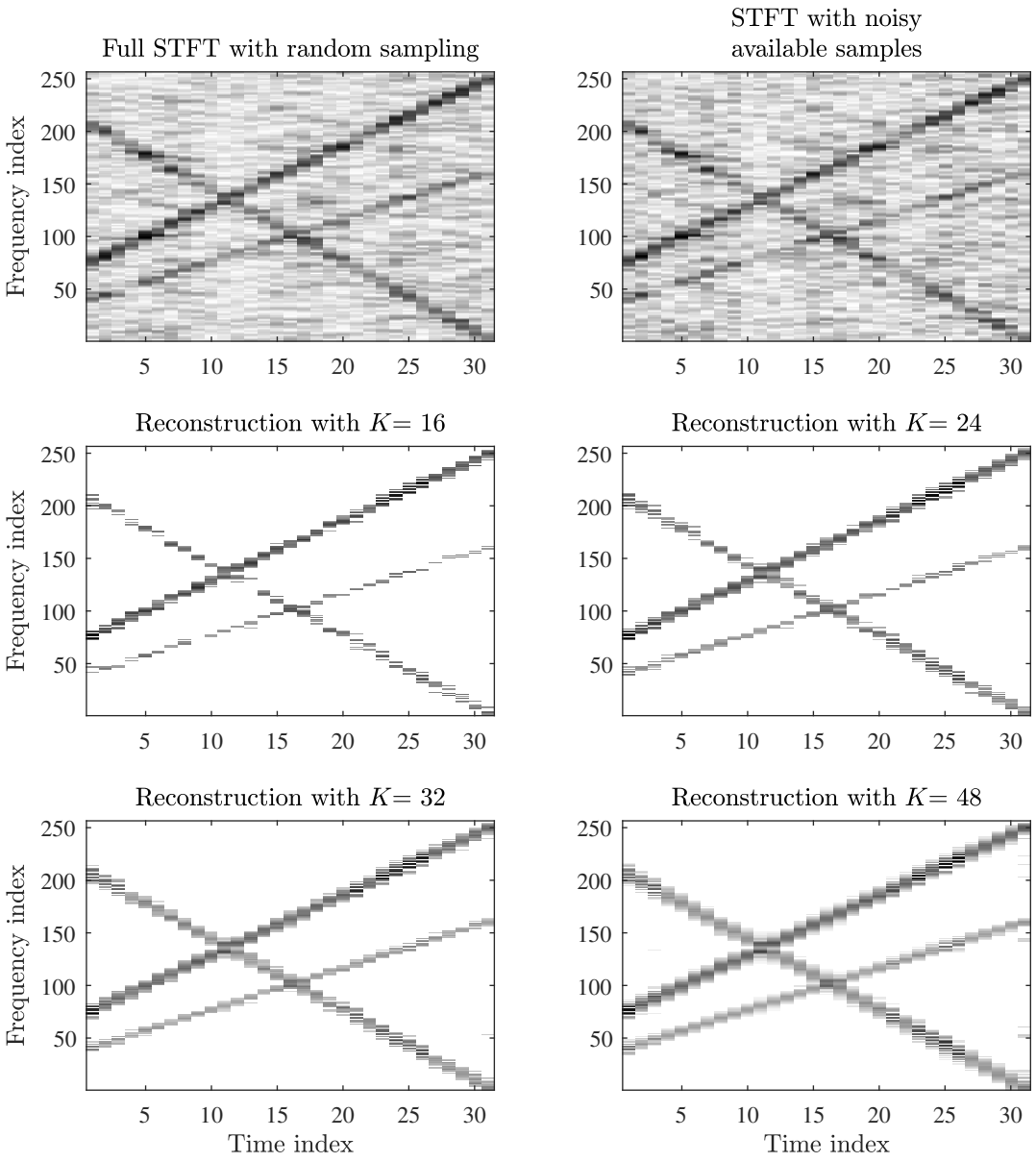

Figure 2.4: Sparse STFT reconstruction of a randomly sampled signal: STFT with the full set of measurements (top left); STFT with the reduced set of noisy measurements with variance $\sigma_\varepsilon = 0.1$ (top right), the reconstruction with $K = 8, 16, 32, 48$ (remaining subplots).

reconstructed STFT assuming the sparsity $K = 10$ is illustrated in Fig. 2.5 (bottom left). The reconstructed STFT with sparsity $K = 50$ is presented in Fig. 2.5 (bottom right).

Also, an audio signal with the words "You and I" is recorded. It was recorded on a MacBook Air laptop using the MATLAB software. The signal was sampled at a frequency $f_s = 44.1$ kHz, with 16-bit A/D conversion and single-channel mode. Assume that 50% of the samples are unavailable. Two sparsities are assumed, $K = 30$ and $K = 80$. The four subplots in Fig. 2.6 present the original STFT, the STFT with a reduced number of measurements, the

Table 2.1: Total averaged reconstruction error in the reconstructed coefficients (in dB) for $N_A = N/2, 2N/3, 3N/4$, and sparsity levels $K = \{16, 24, 32, 48\}$ when randomly sampled signal is used.

$N_A = N/2$	$K = 16$	24	32	48
Theory	-0.23	-0.58	-0.83	-1.07
Statistics	-0.35	-0.74	-1.01	-1.23
$N_A = 2N/3$				
Theory	-0.50	-0.93	-1.25	-1.57
Statistics	-0.61	-1.00	-1.28	-1.61
$N_A = 3N/4$				
Theory	-0.54	-0.96	-1.35	-1.64
Statistics	-0.65	-1.03	-1.37	-1.57

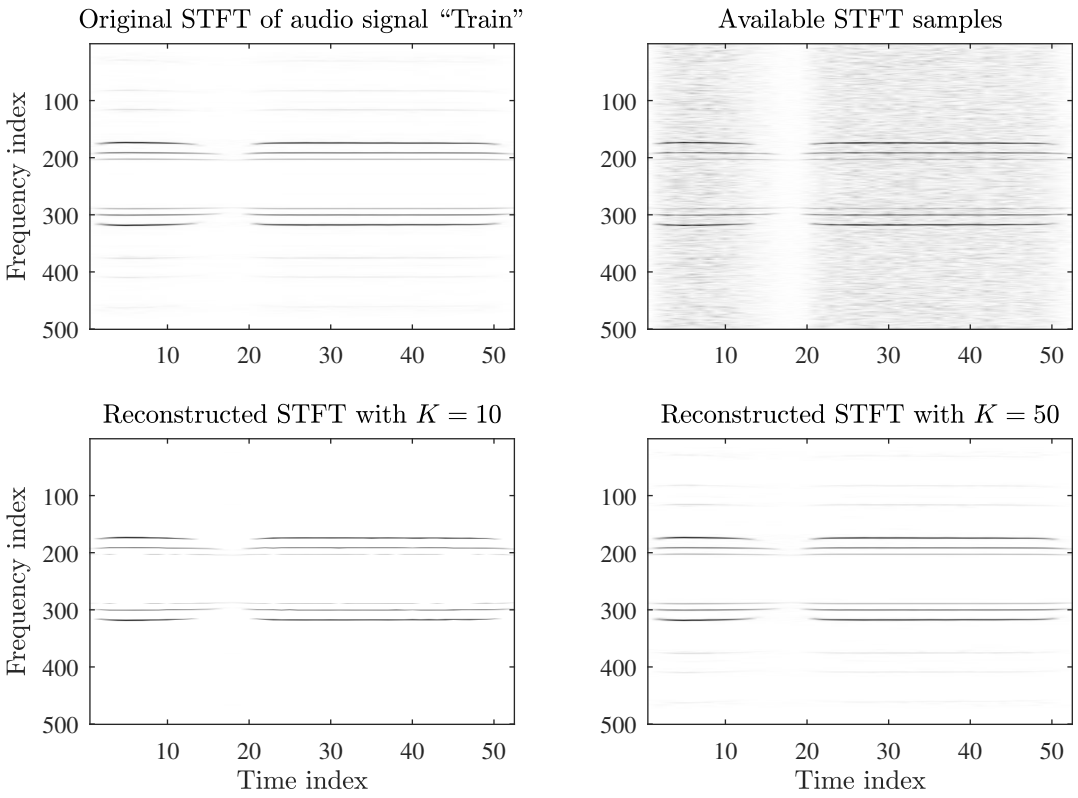

Figure 2.5: The recovery of the audio signal "Train": STFT with full set of measurements (top left); STFT with 50% of available samples (top right); Reconstructed STFT with $K = 10$ (bottom left); Reconstructed STFT with $K = 50$.

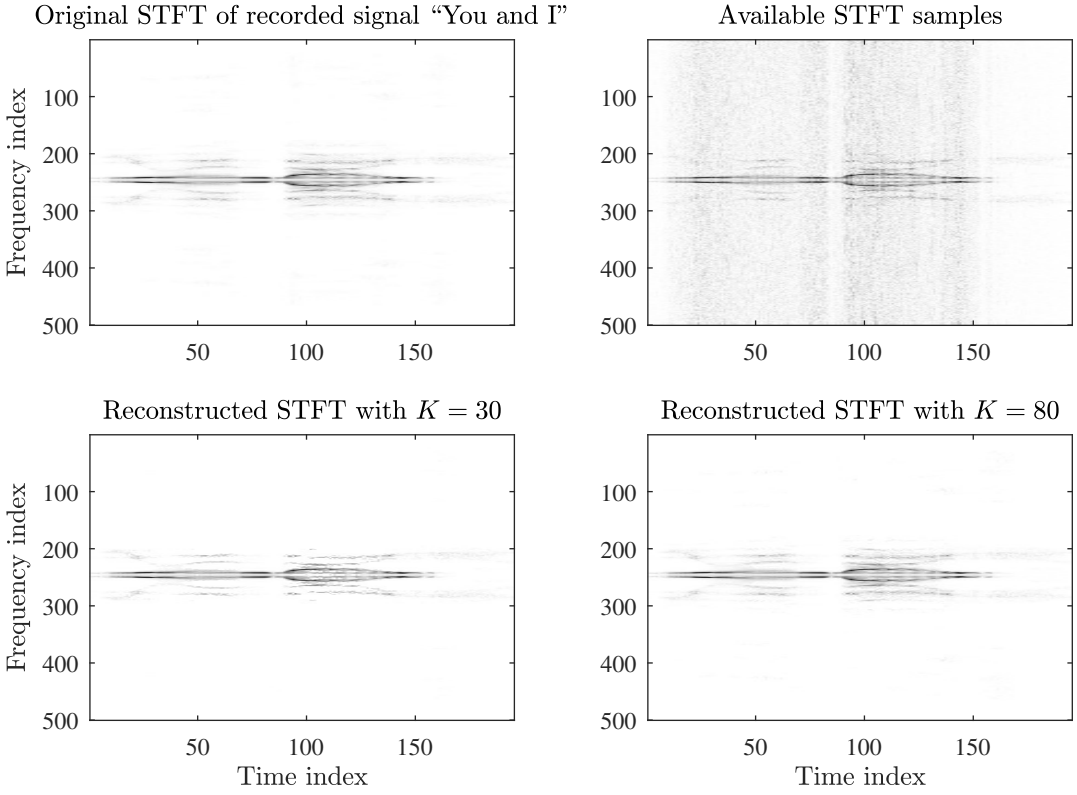

Figure 2.6: The recovery of the recorded audio signal "You and I": STFT with full set of measurements (top left); STFT with 50% of available samples (top right); Reconstructed STFT with $K = 30$ (bottom left); Reconstructed STFT with $K = 80$.

STFT reconstruction with $K = 30$, and the STFT reconstruction with $K = 80$, respectively.

The total error of the reconstruction using different sparsities K for the two audio signals is shown in Fig. 2.7. The error is calculated according to 100 realizations. The black solid line presents the the theoretical error. The red circles are the statistical results. We can conclude that in both cases, the results are similar, proving that the exact error equation is found and statistically confirmed.

Example 4: Radar signals. Another suitable application for the recovery of nonsparse signals assuming sparsity constraint is inverse synthetic aperture radar (ISAR) imaging [55–60]. In general, ISAR images require only few components for transmission and reception, which is sufficient for obtaining information the range and cross-range of a target. That makes them usually sparse in the 2D-DFT domain. Assuming sampling on the grid, an ISAR signal, of size $N \times M$, has reconstruction error

$$E_{theoretical} = 10 \log \left(K \frac{N_Q}{N_A NM} \|\mathbf{S}_N(n) - \mathbf{S}_{NK}(n)\|_2^2 + K \frac{(NM)^2}{N_A} \sigma_\varepsilon^2 \right). \tag{2.37}$$

where $N_Q = NM - N_A$.

The ISAR image of an airplane MIG-25 is considered [61]. It is approximately sparse in

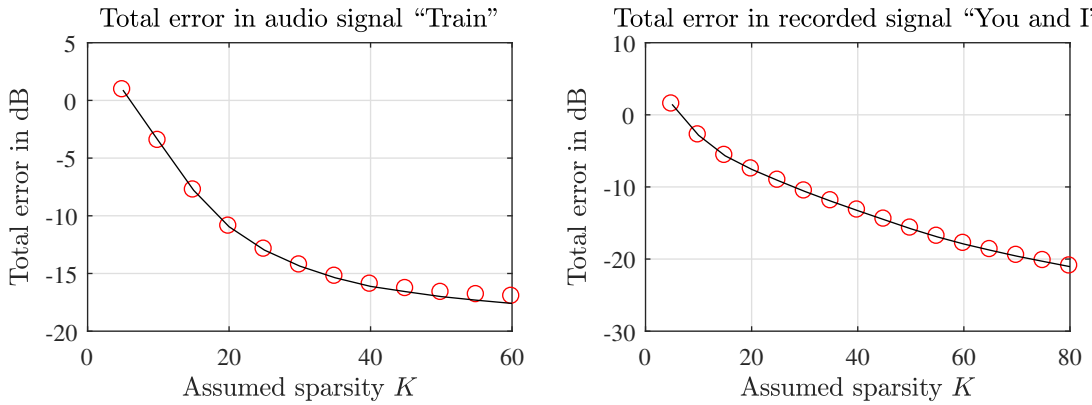

Figure 2.7: Total error in dB after the reconstruction in 100 realizations of "Train" (left) and "You and I" (right), with various sparsity levels. Black line represent the theoretical results, red circles is the statistical estimation.

the 2D-DFT domain. The ISAR image is shown in the top left subplot of Fig. 2.8. In the logarithmic scale (top right subplot), the nonsparsity is noticeable. Sparse reconstructions from $N_A = NM/2$ available samples, with $K = 50, 150, 250, 350$ are shown in the remaining four subplots of Fig. 2.8. The error calculation, according to Eq. (2.37), is presented in Table 2.2.

Table 2.2: The error in the ISAR reconstructed coefficients for MIG data for assumed sparsities $K = \{50, 150, 250, 350\}$.

$N_A = NM/2$	$K = 50$	150	250	350
Theory	-20.92	-24.72	-28.71	-31.60
Statistics	-20.19	-24.36	-28.17	-30.34

$N_A = 2NM/3$	$K = 50$	150	250	350
Theory	-16.36	-17.87	-20.12	-20.12
Statistics	-17.85	-19.32	-21.58	-21.58

2.4 Sampling generalization

For uniform sampling, the considered instants in the reduced set of measurements are defined by sampling theorem and a random subset of all such instants. The random sampling is done at a set of fully random instants within the considered time interval. These two cases can be considered as the special cases of the nonuniform (jittered) sampling at the instants $t_n = n + \nu_n$, where ν_n it the random variable causing the shift in the uniform sampling at instant n (unit sampling interval is assumed without loss of generality). the random variable (jitter) with a uniform distribution $-\Delta/2 \leq \nu_n \leq \Delta/2$ is assumed. The two special cases of

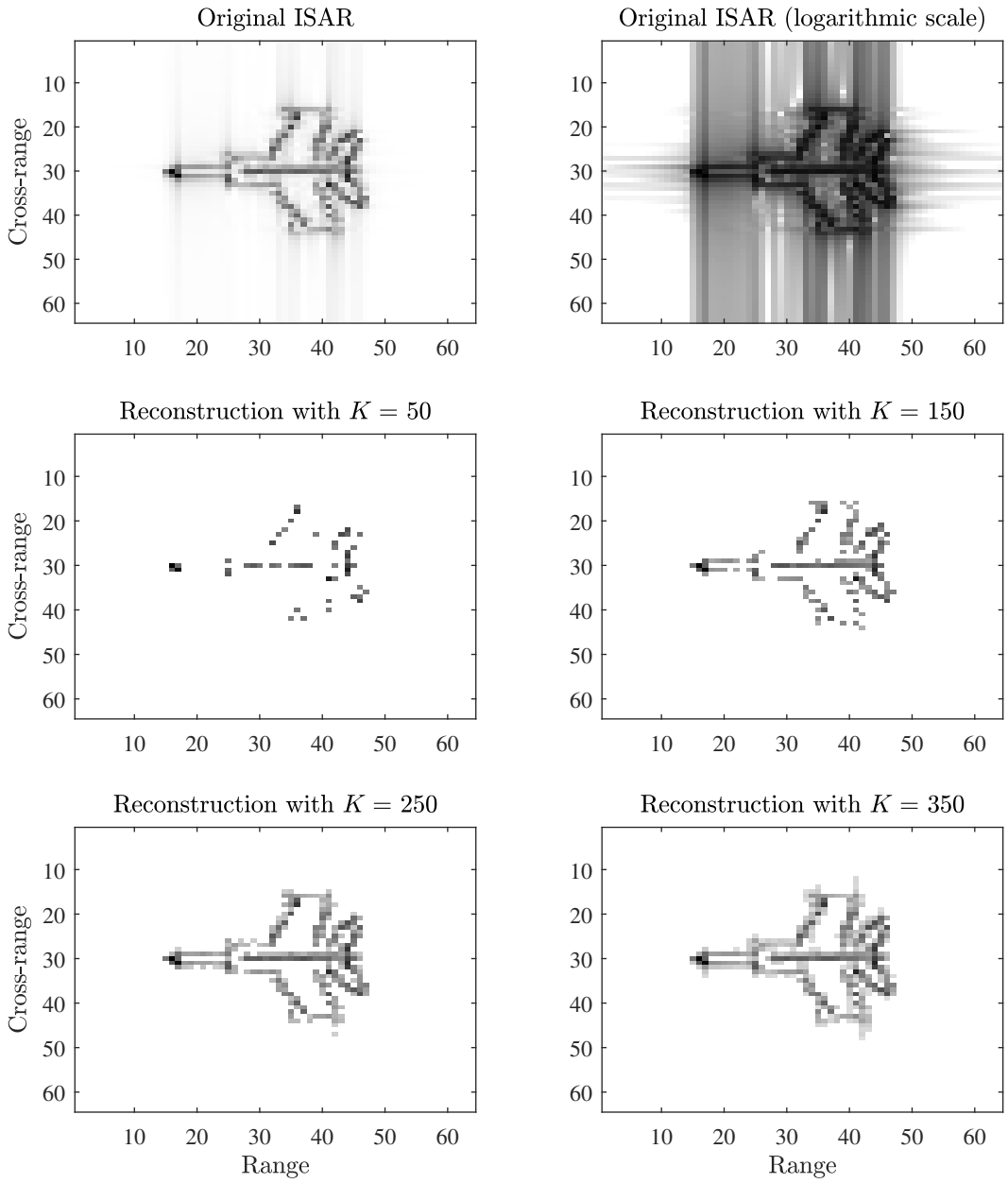

Figure 2.8: Reconstruction of the ISAR MIG 25 image: Original ISAR (top left); Original ISAR in dB (top right); the reconstruction with $K = 50, 150, 250, 350$.

this nonuniform sampling are: (i) the uniform sampling (when $\Delta = 0$) and (ii) the random sampling (when Δ is large). The resulting reconstruction depends on the degree of randomness in the nonuniform sampling, as it will shown next.

The general form of the expected squared error in the reconstructed coefficients is obtained using the initial estimate. Having a signal $x(t_n)$ sampled at $t_n = n + \nu_n$, its initial estimate

can be written as

$$X_0(k) = \sum_{n\in\mathbb{N}_A} A_0 e^{j\frac{2\pi}{N}kt_n} = \sum_{n\in\mathbb{N}_A} A_0 e^{j\frac{2\pi}{N}kn} e^{j\frac{2\pi}{N}k\nu_n}. \tag{2.38}$$

The initial estimate of a single-component $x(t_n)$, with amplitude A_0 at k_0, will then be

$$X_0(k) = \sum_{n\in\mathbb{N}_A} A_0 e^{j\frac{2\pi}{N}kn} e^{j\frac{2\pi}{N}(k-k_0)\nu_n}. \tag{2.39}$$

The mean value of $X_0(k)$ becomes

$$\mu_{X_0(k)} = A_0 \sum_{n\in\mathbb{N}_A} E\{e^{j\frac{2\pi}{N}(k-k_0)n}\} E\{e^{j\frac{2\pi}{N}(k-k_0)\nu_n}\}. \tag{2.40}$$

We have seen that for the first term, $A_0 \sum_{n\in\mathbb{N}_A} E\{e^{j\frac{2\pi}{N}(k-k_0)n}\}$, the mean value is $\mu_{X_0(k)} = A_0 N_A \delta(k-k_0)$. For the second term, caused by a random sampling jitter, the expected value is calculated as

$$\begin{aligned}\mu_\nu = E\{e^{j\frac{2\pi}{N}(k-k_0)\nu_n}\} &= \int_{-\Delta/2}^{\Delta/2} p(\Theta) e^{j\frac{2\pi}{N}(k-k_0)\Theta} d\Theta \\ &= \frac{\sin(\frac{\pi(k-k_0)\Delta}{N})}{\frac{\pi(k-k_0)\Delta}{N}} = \operatorname{sinc}\Big(\frac{\pi(k-k_0)\Delta}{N}\Big).\end{aligned} \tag{2.41}$$

The probability density function $p(\Theta) = \frac{1}{\Delta}$ is used for the uniform random variable $\Theta = \nu_n$, within the interval $[-\frac{1}{\Delta}, \frac{1}{\Delta}]$. When $k - k_0 = 0$, the expected value in Eq. (2.41) is 1.

The variance is calculated as,

$$\sigma^2_{X_0(k)} = \sum_{n\in\mathbb{N}_A} \sum_{m\in\mathbb{N}_A} |A_0|^2 E\{e^{j\frac{2\pi}{N}(k-k_0)(n-m)}\} E\{e^{j\frac{2\pi}{N}(k-k_0)(\nu_n-\nu_m)}\}. \tag{2.42}$$

For $k \neq k_0, n \neq m$, the second term is written as

$$E\{e^{j\frac{2\pi}{N}(k-k_0)(\nu_n-\nu_m)}\} = E\{e^{j\frac{2\pi}{N}(k-k_0)\nu_n}\} E\{e^{j\frac{2\pi}{N}(k-k_0)\nu_m}\}, \tag{2.43}$$

which, obviously, is equal to μ_ν^2, as the expectations over statistically independent ν_n and ν_m. For $n = m$, Eq. (2.43) produces the result equal to 1.

When all the available samples are considered, there are N_A terms in the sum when $m = n$, and $N_A(N_A - 1)$ terms when $n \neq m$. In the multicomponent case, i.e. $K > 1$, the variance is a sum of individual variances of each noise-only component $k \neq k_l$.

For $K > 1$, $k_l = k_1, k_2, \ldots, k_K$, the generalized variance of the components at $k_l \neq k_1, k_2, \ldots, k_K$ will be

$$\sigma^2_{X_0(k)} = \sum_{l=1}^{K} N_A |A_l|^2 \Big[1 - \frac{N_A - 1}{N - 1} \operatorname{sinc}^2\big(\frac{\pi(k-k_l)\Delta}{N}\big)\Big][1 - \delta(k-k_l)]. \tag{2.44}$$

The variance is frequency dependent. Its mean can be estimated as a frequency independent parameter

$$G(\Delta) = \frac{1}{N}\sum_{k=1}^{N} \operatorname{sinc}^2\Big(\frac{\pi k \Delta}{N}\Big). \tag{2.45}$$

Note that, in the same manner as in the analysis for the partial uniform DFT and the partial random DFT, we can define variances in other measurement matrices.

Example: Generalization. The nonuniform distribution analyzes the case when the signal is close to the uniform sampling, with a small-offset of the true value. This is known as the jittering effects, which affects many real-signals in their transmission.

Consider an approximately sparse signal in the DFT domain,

$$X(k_l) = \begin{cases} 1 + \kappa(l), & \text{for } l = 1, 2, \ldots, K, \\ -3l/2K, & \text{for } l = K+1, K+2, \ldots, N. \end{cases} \tag{2.46}$$

The sparsity level $K = 7$ and $\kappa(l)$ is a random variable. It is uniformly distributed between 0 and 0.4. The error in the reconstructed coefficients is calculated and given in Fig. 2.9. The cases with $N_A = 2N/3$ and $N_A = 3N/4$ available samples are considered. The error calculation is analyzed for the cases when $\Delta = 0$ (uniform sampling), $\Delta = 1$ (nonuniform sampling) and $\Delta \gg 0$ (random sampling). The assumed sparsity is varied $S_K = 1, 2, \ldots, 15$. Black color represents the statistical values

$$E_{statistical} = 10 \log\left(||\mathbf{X}_K - \mathbf{X}_R||_2^2\right), \tag{2.47}$$

while red color represents the theoretical results,

$$E_{theoretical} = 10 \log\Big(\frac{K}{N_A}\Big[1 - \frac{N_A - 1}{N - 1} G(\Delta)\Big] \|\mathbf{X} - \mathbf{X}_{K0}\|_2^2\Big). \tag{2.48}$$

We can see that, in all three cases, the error significantly drops when the assumed sparsity is $S_K = 7$ reached the signal approximate sparsity. The uniform sampling produces the best reconstruction results in all considered cases, while an increased randomness results in a higher reconstruction error. The theoretical and statistical results highly agree, proving that, in the general case, the accuracy of the derived error.

2.5 Quantization error in compressive sensing

So far, it has been assumed that the measurements can take as many bits as needed for their representation. If a non-quantized signal is strictly sparse, the error, calculated as a difference between the original and reconstructed signal, will be zero or negligible. However, the reconstruction will produce some error if a signal is reconstructed from quantized (digitized)

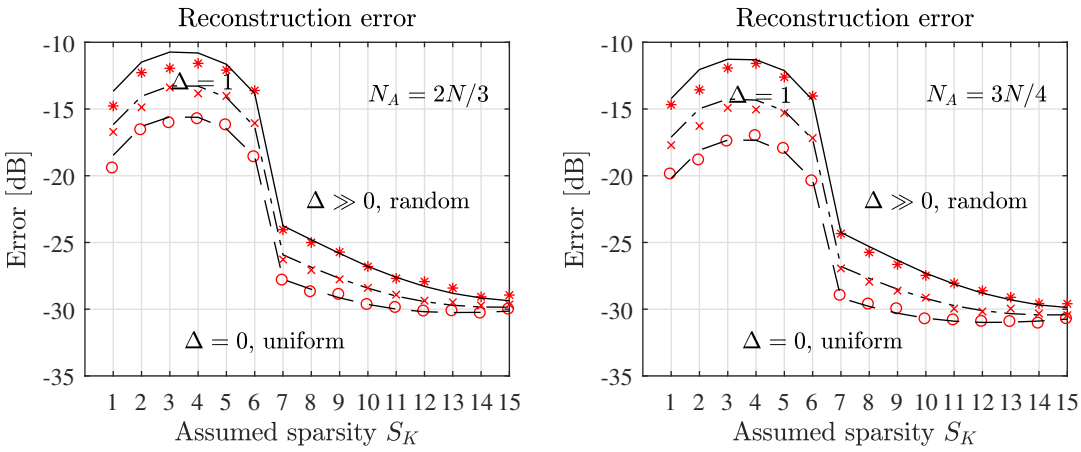

Figure 2.9: Reconstruction error as a function of various sparsity levels K for different values Δ: for $N_A = 2N/3$ of available samples (left) and for $N_A = 3N/4$ of available samples (right). Values for Δ used are $\Delta = 0$ (lower lines), $\Delta = 1$ (middle lines), and $\Delta \gg 0$ (higher lines).

measurements. After quantization, the input signal will be corrupted with uniform additive noise, whose values are between the bounds of the quantization levels.

Despite the effects the quantization is exploiting, it is of great importance in the hardware implementation. The samples measurements are stored into registers of $(B+1)$ bits, where B bits are for the measurement absolute value and the additional bit is for its sign. The samples are formed as

$$\mathbf{y}_B = \text{digital}_B\{\mathbf{AX}\} \tag{2.49}$$

or for complex-valued case, where both real and imaginary parts are quantized, as

$$\mathbf{y}_B = \text{digital}_B\{\Re\{\mathbf{AX}\}\} + j\text{digital}_B\{\Im\{\mathbf{AX}\}\}, \tag{2.50}$$

Considering the quantized measurements, the transformation coefficients $X(k)$ are reconstructed with the quantization error that depends on number of bits and number of measurements.

When a signal is quantized in the amplitude, the error which produced by the quantization is the quantization noise within the limits

$$|e(n_i)| < \Delta_q/2, \tag{2.51}$$

where Δ_q is related to B as

$$\Delta_q = 2^{-B}. \tag{2.52}$$

To achieve appropriate analysis, the quantization error of is assumed to be an uniformly distributed white noise, which affects the measurements in the form

$$\mathbf{y} = \mathbf{y}_B + \mathbf{e}, \tag{2.53}$$

where $\mathbf{e}$ is the vector of the quantization noise with elements $e(n_i)$. Note that the quantization errors must be uncorrelated with each other nor with the considered signal.

By definition, the mean and variance of that noise is [8]

$$\mu_{\mathbf{e}} = \mathrm{E}\{\mathbf{e}\} = 0, \tag{2.54}$$

$$\sigma_{\mathbf{e}}^2 = \Delta_q^2/12. \tag{2.55}$$

When a complex-valued signal is analyzed, both real and imaginary parts of samples add to the noise, resulting in a variance

$$\sigma_{\mathbf{e}}^2 = 2\Delta_q^2/12 = \Delta_q^2/6. \tag{2.56}$$

As mentioned in Section 2.3.1. (Additive noise), noisy $\mathbf{y}$ will lead to noisy $X_0(k)$ with variance $\sigma_{X_0(k)}^2 = \sigma_{\mathbf{e}}^2$. The noise variance of the reconstructed signal is then

$$\sigma_{X_R(k)}^2 = \sigma_{\mathbf{e}}^2. \tag{2.57}$$

The energy of the reconstruction error in the K reconstructed components is

$$\|\mathbf{X}_R - \mathbf{X}_K\|_2^2 = K\sigma_{\mathbf{e}}^2. \tag{2.58}$$

In this interesting to note that, the energy of error in the reconstructed components will remain unchanged if [52]

$$K\sigma_{\mathbf{e}}^2 = K\frac{2^{-2B}}{6} = \text{const.} \tag{2.59}$$

That is, reducing the number of B bits to $B-1$ bits will require reducing the number of sparsity components from K to $K/4$. The logarithmic expression of the error cane be written as

$$e^2 = 10\log\left(\|\mathbf{X}_R - \mathbf{X}_K\|_2^2\right) = 3.01\log_2 K - 6.02B - 7.78. \tag{2.60}$$

2.5.1 Quantization effect analysis

The effect of quantization will be examined in the next two examples.

Example 1: Sparse signal quantization error. The sparse signal reconstruction analysis is performed in this example. The signal is of the form

$$X(k_l) = \begin{cases} \frac{\sqrt{N_A}}{K}(1-\kappa(l)), & \text{for } l = 1,\ldots,K \\ 0, & \text{for } l = K+1,\ldots,N, \end{cases} \tag{2.61}$$

with length $N = 256$ and the random changes of coefficient amplitudes is uniformly distributed in between $0 \leq \kappa(l) < 0.2$. It is considered that $N_A = 128$ available measurements are quantized. The quantization levels to bits $B \in \{4, 6, 8, 10, 12, 14, 16, 18, 20, 24\}$ and sparsity levels $K \in \{3, 8, 13, 18\}$ are analyzed.

The average statistical and theoretical signal-to-nose ratios SNR_{st} and SNR_{th} values are shown in Fig. 2.10. The results are averaged over 300 realizations. The statistical error SNR_{st}

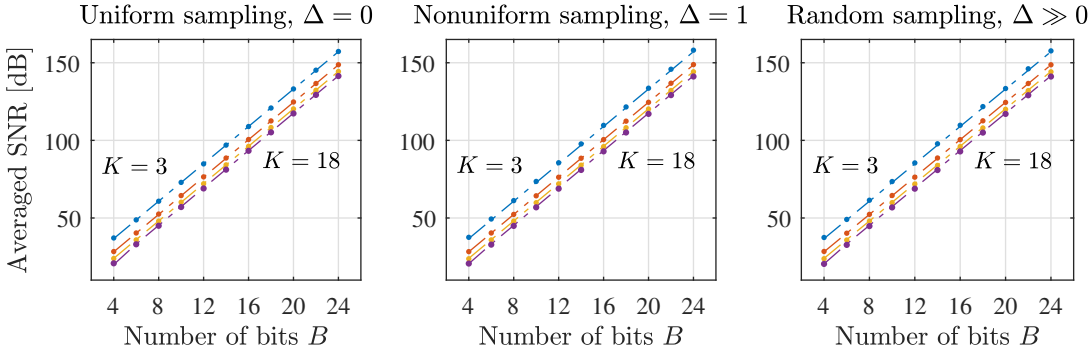

Figure 2.10: Average reconstruction SNR of sparse signals with quantized measurements as a function of number of bits B, for various numbers of measurements and sparsity levels $K \in \{3, 8, 13, 18\}$. The statistical error is presented with dots and the theoretical results are presented by dot-dashed lines: when the signal is uniformly sampled (left); nonuniformly sampled (middle); randomly sampled (right).

is presented with black dots, and the dash-dot lines are the theoretical errors, SNR_{th}. It can be concluded that the results are of high agreement.

Example 2: Nonsparse signal quantization error. The signal is modeled as

$$X(k_l) = \begin{cases} \frac{\sqrt{N_A}}{K}(1-\kappa(l)), & \text{for } l = 1, \dots, K \\ \frac{\sqrt{N_A}}{K}\exp(-l/8K), & \text{for } l = K+1, \dots, N. \end{cases} \tag{2.62}$$

The length of the signal is $N = 256$ and the andom uniform changes of coefficient amplitudes is assumed to be between $0 \leq \kappa(l) < 0.2$. In order to reduce its influence to the quantization level, the amplitudes of the coefficients $X(k)$ for $k_l \notin \mathbb{K}$ are $X(k_l) = \exp(-l/(8K))$. In that case, the effect of quantization influences the reconstruction procedure when up to $B = 14$ bits are used. The enery cause by the nonsparsity is dominant for the case when $B \geq 16$. The results are presented in Fig. 2.11, proving a similar results of the statistical results with the theoretical error.

2.6 Noise folding

Another important issue is the analysis of the quantization noise in the transform coefficients prior to taking the measurements [62]. This noise is called the quantization noise folding and it will be denoted by $\mathbf{z}$. Then, the measurements are of the form

$$\mathbf{y}_B + \mathbf{e} = \mathbf{A}(\mathbf{X} + \mathbf{z}), \tag{2.63}$$

which can be rewritten in the form of

$$\mathbf{y}_B + \mathbf{v} = \mathbf{A}\mathbf{X} \tag{2.64}$$

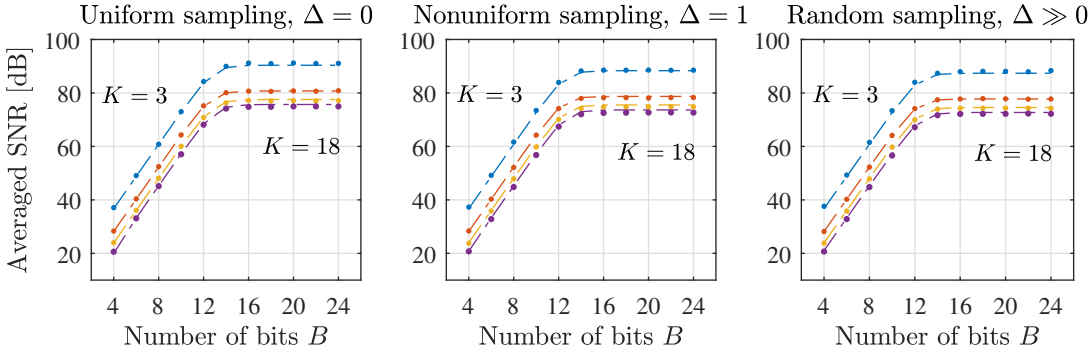

Figure 2.11: Average SNR of the reconstruction of nonsparse signals with quantized measurements as a function of number of bits B, for various numbers of measurements and sparsity levels $K \in \{3, 8, 13, 18\}$. The statistical error is presented with dots and the theoretical results are presented by dot-dashed lines: when the signal is uniformly sampled (left); nonuniformly sampled (middle); randomly sampled (right).

where $\mathbf{v} = \mathbf{e} - \mathbf{A}\mathbf{z}$. The value $\mathbf{e}$ is the quantization noise which affects the signal samples with covariance $\sigma_{\mathbf{e}}^2\mathbf{I}$. The noise vector $\mathbf{z}$ is random whose covariance is $\sigma_{\mathbf{z}}^2\mathbf{I}$. Note that it is independent of $\mathbf{e}$. Thus, the covariance matrix of the noise $\mathbf{v}$ is

$$\mathbf{C} = \sigma_{\mathbf{e}}^2\mathbf{I} + \sigma_{\mathbf{z}}^2\mathbf{A}\mathbf{A}^H. \tag{2.65}$$

For the partial DFT matrix, the relation $\mathbf{A}\mathbf{A}^H = \frac{N}{N_A}\mathbf{I}$ holds. The variance of $\mathbf{v}$ is then

$$\sigma_{\mathbf{v}}^2 = \sigma_{\mathbf{e}}^2 + \frac{N}{N_A}\sigma_{\mathbf{z}}^2, \tag{2.66}$$

with the covariance matrix $\mathbf{C} = \sigma_{\mathbf{v}}^2\mathbf{I}$.

However, when sparse signalas are considered, the quantization error only affects the K nonzero components of $\mathbf{X}$. It means that the noise $\mathbf{A}\mathbf{z}$ variance is $\frac{K}{N_A}\sigma_{\mathbf{e}}^2$ or

$$\|\mathbf{X}_R - \mathbf{X}_K\|_2^2 = K\sigma_{\mathbf{e}}^2 + \frac{K}{N_A}\sigma_{\mathbf{z}}^2. \tag{2.67}$$

Finally, for the nonsparse partial DFT matrix case, the error is calculated as

$$\|\mathbf{X}_R - \mathbf{X}_K\|_2^2 = K\sigma_{\mathbf{e}}^2 + \frac{K}{N_A}\sigma_{\mathbf{z}}^2 + \frac{K}{N_A}\left[1 - \frac{N_A - 1}{N - 1}G(\Delta)\right]\|\mathbf{X} - \mathbf{X}_K\|_2^2. \tag{2.68}$$

We assume that the quantization of the K main components in $\mathbf{X}$ moslty influences the corresponding part of the error calculation. This relation is statistically checked in the next example.

Example: Error calculation with noise folding. The simulation with nonsparse signals affects by noise folding is repeated for 300 realizations using the formulation from Eq. (2.68). The results are presented in Fig. 2.12, proving a close agreement theoretical and statistical results.

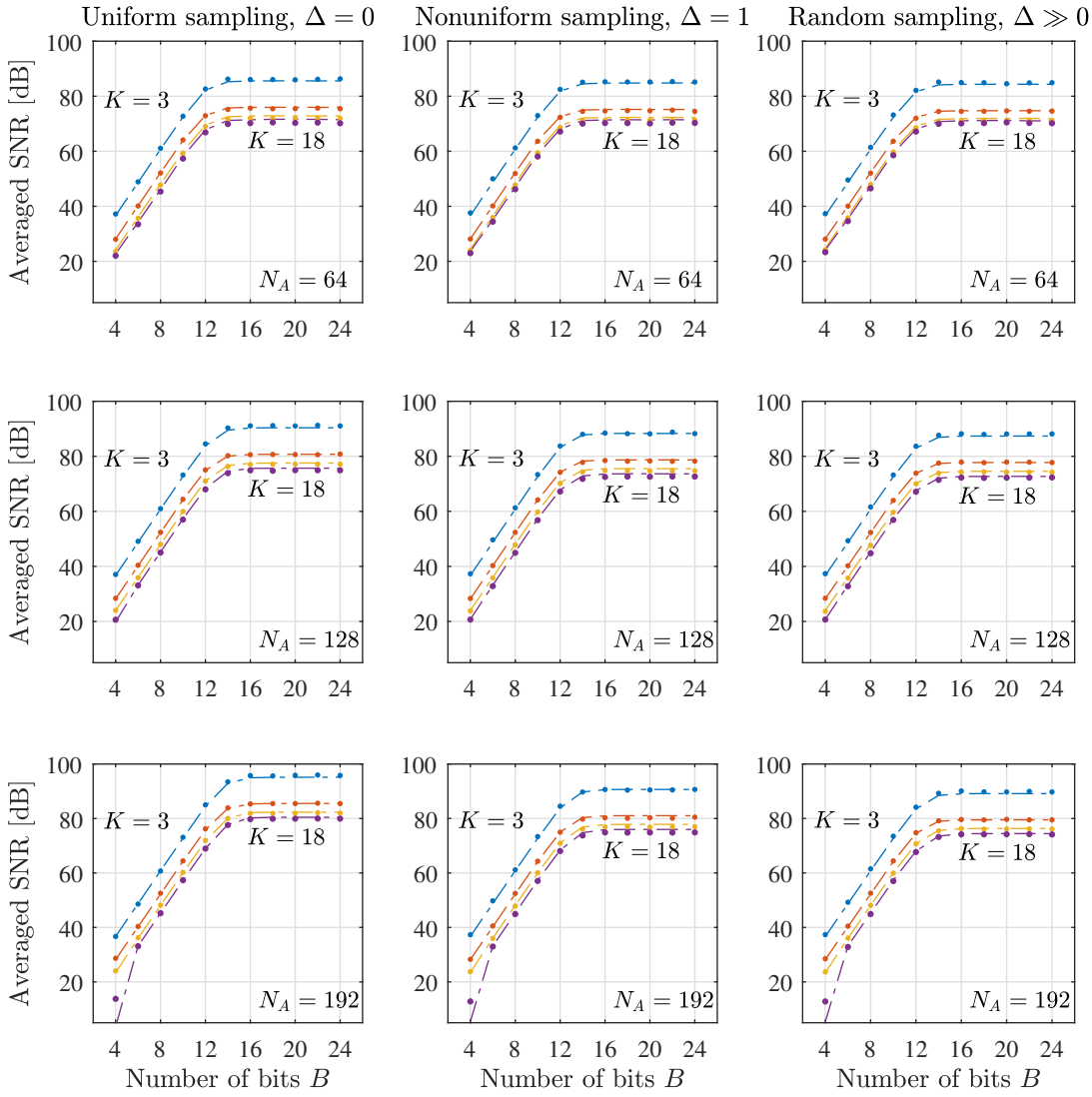

Figure 2.12: Average SNR of nonsparse signals reconstruction with noise folding when various number of available measurements is considered, for different sampling methods. Top subplots - $N_A = N/4$ available samples, middle subplots - $N_A = N/2$, bottom subplots - $N_A = 3N/4$. Left subplots - uniform sampling, middle subplots - nonuniform sampling when $\Delta = 1$, left subplots - random sampling when $\Delta \gg 0$.

Chapter 3

Wideband sonar signal reconstruction

Contents

Many radar systems are based on a few targets in the signal, showing the potential of using the compressive sensing algorithms for their processing. The idea of importing the CS theory to the detection of targets and their successful recovery in the radar systems was discussed previously in the literature [55, 63–66]. In the research, indeed, the CS framework is seen as a useful tool for the reconstruction of sparse radar signals. Even though radar and sonar systems have many common basic principles, yet the application of CS techniques is still relatively new in sonars. Despite the similarity in the rules, there are specific characteristics of the sonar systems that need to be considered for a successful analysis. The main difference is the environment in which they operate, mainly due to entirely different propagation characteristics. This will be discussed in more detail later in this thesis.

The complexity of the problem made it difficult for the transmitted signals to be anything more than basic forms of sonar signals to be analyzed and used in the recent literature. The usage of specific sequence form of these signals has already produced promising results in the reconstruction of sonar images. The implementation of CS idea to the underwater sonar signals was initially discussed in [67, 68]. However, only the Alltop sequence was considered a sequence used to form the transmitted signal and reconstruct the sonar image with a reduced number of measurements. In [69], the results in sonar imaging were improved using the M sequence, as an excellent alternative to the Alltop sequence, in forming the transmitted signal waveform.

In this Chapter, we will consider a whole spectrum of various sequences in the sonar imaging within the CS to find the best solution to the sonar signal reconstruction problem. The considered sequences are the random binary sequence, the random Gaussian, Bjorck, and Zadoff-Chu sequence, in addition to the Alltop and maximum length sequence (M sequence). All these sequences are studied and compared concerning the performances notable for sonar imaging within the CS framework.

The implementation of the radar systems was also expanded from narrowband [63] to wideband [66]. Although the Alltop and the M sequences were considered theoretically, in practice, only the basic forms were considered due to their simpler hardware implementation [70]. This challenge will also be taken into account in the analysis of real data in the next sections. The main results presented in this Chapter were published in [71–74]. In the analysis, it is common to consider the targets on the grid. However, in practice, they are off-grid, causing even the targets with a small number of reflecting points to be only approximately sparse when considered in sonar signals. This effect of image leaking due to the off-grid impacts influences the CS reconstruction. It has been examined by extending the analysis of approximately sparse and nonsparse signals from the previous section.

We tackle one more problem in this Chapter: the decomposition of two misaligned receivers for two close components. It will be shown that the problem can be successfully surpassed using high-resolution techniques in time-frequency analysis.

3.1 General sonar signal modelling

A typical model of a transmitted wideband sonar signal is of form

$$x(t) = s\Big(\frac{t}{\lambda}\Big)\exp\left(j2\pi f_c t\right), \tag{3.1}$$

where $s\big(\frac{t}{\lambda}\big)$ is the transmitted form of the sequence. The sequence is coded within the width λ, $0 \leq t < N\lambda$, and modulated with the carrier frequency f_c. The received signal is a delayed and attenuated version of $x(t)$. If one target is considered, i.e., if $K = 1$, the received (echoed) signal is formed as

$$r_1(t) = g\, s\left(\frac{\frac{c+\nu}{c-\nu}(t-\tau)}{\lambda}\right)\exp\Big(j2\pi f_c \frac{c+\nu}{c-\nu}(t-\tau)\Big), \tag{3.2}$$

where v is the velocity of the target, c is the underwater speed of sound, and g is a complex-valued scattering coefficient. Due to the Doppler effect, the received signal is scaled in frequency for $(c+v)/(c-v)$. Additionally, it is shifted in time for a value τ.

The signal is sampled according to the sampling theorem at instants $n\Delta t$, with Δt being the sampling interval. The discrete received signal, when $K > 1$ targets are considered, is the sum of K received discretized components of form (3.2). That is

$$r(n) = \sum_{i=1}^{K} g_{k_i} s(n - d_{k_i})\exp\Big(j\omega_{k_i} n\Big), \tag{3.3}$$

where $s(n - d_{k_i})$ is the circular shift of the sequence. The parameter d_{k_i} presents the time delay τ which is defined by the range of the targets. The parameter ω_{k_i} corresponds to the cross-range of targets corresponding to the frequency shift. If we consider the targets to be on the grid, the coordinates are then taken from the finite set

$$(d_p, \omega_q) \in \{d_1, d_2, \ldots, d_N\} \times \{\omega_1, \omega_2, \ldots, \omega_N\} \tag{3.4}$$

where d_p takes values from $d_p \in \{d_1, d_2, \ldots, d_N\}$ and $\omega_q \in \{\omega_1, \omega_2, \ldots, \omega_N\}$, making it a total of N^2 of possible positions of the targets. If the targets are off-grid, they will spread over several points, with the most significant influence on a few neighboring grid points. The off-grid effects cause the analyzed signals to be only approximately sparse. In the analysis we will first assume that the targets are on the grid, as it is common in literature, and then analyze the effects of sparsity degradation due to off-grid sampling.

For a pair $(d_p, \omega_q) = \left(p, \frac{2\pi}{N} q\right)$, the basis function can be calculated as

$$\phi_{p,q}(n) = s(n - p) \exp\left(j 2\pi q \frac{n}{N}\right). \tag{3.5}$$

and received is the signal

$$r(n) = \sum_{i=1}^{K} g_{k_i} \phi_{p_i, q_i}(n). \tag{3.6}$$

of the k-th scatterer. The relation between the indices for the scatterer k, and range and cross-range positions p and q is

$$\begin{aligned} k &= p + Nq, \\ p &= k - N\lfloor k/N \rfloor, \\ q &= \lfloor k/N \rfloor, \end{aligned} \tag{3.7}$$

where $p = 0, 1, \ldots, N-1$, $q = 0, 1, \ldots, N-1$, $k = 1, 2, \ldots, N^2 - 1$, and $\lfloor k/N \rfloor$ presenting the rounding of k/N to the closest lower integer value.

The periodic autocorrelation (AC) function of the sequence $s(n)$ is defined as

$$R_s(n) = \sum_{m=1}^{N} s(n + m) s^*(m) \tag{3.8}$$

Note that the AC function is associated to the coherence index μ from Eq. (1.50), as it will be seen later in the chapter.

3.1.1 Relation to compressive sensing

Taking into account the nature of the received signal, it can be analyzed as a signal in the representation domain with basis functions

$$\phi_k(n) = s(n - d_k) \exp\left(j \omega_{k_i} n\right), \tag{3.9}$$

and rewritten as

$$r(n) = \sum_{i=1}^{K} g_{k_i} \phi_{k_i}(n) \tag{3.10}$$

or in matrix form

$$\mathbf{r} = \mathbf{\Phi g}, \tag{3.11}$$

The vector $\mathbf{r}$ is the received column vector of the echoed signal, and $\mathbf{\Phi}$ is the matrix with basis functions. The scattering coefficients $g(k) = g_k$ are within the column vector $\mathbf{g} = [g(0), g(1), \ldots, g(N^2 - 1)]^T$.

In the compressive sensing sense, if the signal $\mathbf{g}$ consists of only few target points, it means that there are only K nonzero coefficients in the full $N \times N$ matrix, with $K \ll N$. Then, the signal is considered as sparse. Since it is sparse, it can be recovered from the received samples $\mathbf{y}$

$$\mathbf{y} = [r(n_1), r(n_2), \ldots, r(n_{N_A})]^T \tag{3.12}$$

or

$$\mathbf{y} = \mathbf{Ag} \tag{3.13}$$

where the elements of $\mathbf{A}$ are from (3.5), i.e.,

$$a_{k,l} = s(n_l - d_p) \exp\Big(j\omega_q n_l\Big), \tag{3.14}$$

For a given scattering k, d_p corresponds to the rearranged range coefficients and ω_q is for the rearranged cross-range coefficients. Note that, since N samples are transmitted, and the results lies in the area of $N \times N$ points, the number of measurements is naturally $N_A = N$.

As mentioned in previous chapters, the initial estimation of the signal is performed using the available observations

$$\mathbf{g}_0 = \mathbf{A}^H \mathbf{y} \tag{3.15}$$

or in element-wise form

$$g_0(k) = \sum_{n_i \in \mathbb{N}_\mathbb{A}} r(n_i) a^*_{k,n_i}. \tag{3.16}$$

If $r(n_i)$ is replaced according to (3.10), we get

$$g_0(k) = \sum_{n_i \in \mathbb{N}_\mathbb{A}} \sum_{i=1}^{K} g_{k_i} \phi_{p_i,q_i}(n_i) a^*_{k,n_i}. \tag{3.17}$$

Denoting the terms $\sum_{n_i \in \mathbb{M}} \phi_{p_i,q_i}(n_i) a^*_{k,n_i}$ by $\mu(k, k_i)$

$$\mu(k, k_i) = \sum_{n_i \in \mathbb{N}_\mathbb{A}} \phi_{p_i,q_i}(n_i) a^*_{k,n_i} = \sum_{n_i \in \mathbb{N}_\mathbb{A}} s(n_i - d_k) s^*(n_i - p_i) e^{j2\pi(q_i - q)n_i/N}, \tag{3.18}$$

the initial estimate will be

$$g_0(k) = \sum_{i=1}^{K} g_{k_i} \mu(k, k_i). \tag{3.19}$$

For a random set of measurements, the values $\mu(k, k_i)$ and $g_0(k)$ are random variables [53, 75]. If the calculation is performed over all samples, i.e., $n_i = 0, 1, 2, \ldots, N-1$, we get

$$\mu(k, k_i) = \sum_{n=0}^{N-1} s(n - d_k) s^*(n - p_i) e^{j2\pi(q_i - q)n/N}. \tag{3.20}$$

It is important to note that, even by taking all samples, the set with measurements is small. That demands the use of CS based reconstruction algorithms since the number of possible target positions is $N \times N = N^2 \gg N_A = N$.

The maximal absolute value $\mu(k, k_i)$, for $k \neq k_i$, is associated to the coherence index of the measurement matrix from (1.50), which, as mentioned, defines the condition for a unique signal reconstruction. The uniqueness condition, as seen in (1.52) is $K < (1 + 1/\mu)/2$.

In the case when all samples are taken, the analysis of the maximal absolute value $\mu(k, k_i)$ for $q_{k_i} = q_k$ is reduced to the analysis of the AC function (3.8)

$$\mu(k, k_i) = \sum_{n=0}^{N-1} s(n - d_k) s^*(n - p_i), \text{ for } q_i = q. \tag{3.21}$$

A good reconstruction performance in the compressive sensing sense can be expected when the maximum absolute value of side lobes of the AC function $|\sum_{n=0}^{N-1} s(n - d_k) s^*(n - p_i)|$ are minimized (for $d_k \neq p_i$). Although strict, the coherence index $\mu(k, k_i)$ can indicate the quality of recovery we may expect from a certain sequence.

The whole expression for $\mu(k, k_i)$ and $k \neq k_i$ reduces to the analysis of the ambiguity function (AF) [76] which is defined as

$$AF(n, r) = \sum_{m=0}^{N-1} s(n + m) s^*(m) e^{j2\pi rm/N}, \tag{3.22}$$

for all n and r. It can be seen that (3.22) equals the AF of the Rihaczek distribution of the sequence [5, 6]. Then, the analysis of $\mu(k, k_i)$ reduces to the estimation of the maximum value of $|AF(n, r)|$ for $(n, r) \neq (0, 0)$, For $(n, r) = (0, 0)$, the results is $AF(0, 0) = \mu(k, k) = 1$. This step will be important in the case of time-varying signals, which is discussed in Section 3.4.

3.1.2 Sequence forms and properties

In the literature, only the basic signal processing forms are used, such as the LFM signal, for underwater transmission [70]. Instead of the basic forms, there are a vast of other sequence forms which can be used for the transmission in sonar systems. Some of them will be represented with their key properties and further examined for the usefulness in the transmission.

Six of them are presented in the next definitions. Discrete-time sequence, of length N, is denoted by $s(n)$, $n = 0, 1, \ldots, N-1$.

Definition 3.1
*The **Gaussian sequence** is formed as*

$$s(n) \sim \frac{1}{\sqrt{N}}\mathcal{N}(0,1). \tag{3.23}$$

The Gaussian sequence is one of the most commonly used sequence forms, whose properties are well known in the literature. The auto-correlation (AC) of the Gaussian sequence is

$$R_s(n) = \mathrm{E}\{s(n+m)s(m)\} = \delta(n-m). \tag{3.24}$$

Note that the AC function takes an approximative form for finite-duration sequences.

Definition 3.2
*The **binary Gaussian sequence** is formed as [77]*

$$s(n) \sim \frac{1}{\sqrt{N}}\,\mathrm{sign}(\mathcal{N}(0,1)). \tag{3.25}$$

The signum of the Gaussian sequence is a simpler yet effective form of the Gaussian sequence, resulting in only the sign part of the measurement. It may be considered as a binary random sequence.

Definition 3.3
*The **Alltop sequence** is first presented in [63, 67]. It is formulated in the form of*

$$s(n) = \frac{1}{\sqrt{N}}e^{j2\pi\frac{n^3}{N}}. \tag{3.26}$$

The property of this sequence is the small intensity of the side lobes in the auto-correlation function, which are in the order of $1/\sqrt{L}$. For the aperiodic AC function, the side lobes are approximately similar to $1/\sqrt{L}$ as well.

Definition 3.4
*The **Bjorck sequence**, for a prime number $N > 2$, $N \equiv 1(\mod 4)$, is formulated as [78, 79]*

$$s(n) = \frac{1}{\sqrt{N}}\exp\Big(j[(n/N)]\arccos\Big(\frac{1}{1+\sqrt{N}}\Big)\Big), \tag{3.27}$$

where $[(n/N)]$ is the Legendre symbol that takes values ± 1 and 0 as

$$[(n/N)] = \begin{cases} 0, \ \textit{for } n = 0 \textit{ mod } N \\ +1, \ \textit{for } n \textit{ is a qudratic residue mod } N \\ -1, \ \textit{for } n \textit{ is a qudratic nonresidue mod } N. \end{cases}$$

*The **Bjorck sequence**, for a prime number $N > 2$, $N \equiv 3(\mod 4)$, is formulated as [78, 79]*

$$s(n) = \begin{cases} \frac{1}{\sqrt{N}} \exp\left(j \arccos\left(\frac{1-N}{1+N}\right)\right), & \text{if } [(n/N)] = -1 \\ 1, & \text{otherwise.} \end{cases} \tag{3.28}$$

Definition 3.5
*The **maximum length sequence** (or **M sequence**) is a pseudo-random binary sequence, generated with linear-shift register using the recursive formula [80]*

$$s(n) = \sum_{m=1}^{N} c_m s(n-m). \tag{3.29}$$

The M sequence is a commonly used tool in the area of spread spectrum techniques in digital communication systems. The two most frequently used systems are the direct-sequence and frequency-hopping spread spectrum. Usually, it is normalized to get the energy in the N samples equal to one. The values of the M sequence, $-1/\sqrt{N}$ and $1/\sqrt{N}$, occur approximately equal times. For the sequence of length $N = 2^m - 1$ the number of $1/\sqrt{N}$ values is $N/2$, while the number of $-1/\sqrt{N}$ values is $N/2 - 1$.

The periodic AC function of the M sequence is of the form

$$R_s(n) = \begin{cases} 1, \text{ for } n = kN \\ -1/N, \text{ elsewhere.} \end{cases} \tag{3.30}$$

In the CS theory sense, the coherence indices of the measurement matrices formed from the M sequences and the Alltop sequence are identical.

Definition 3.6
*The **Zadoff-Chu sequence** is formed as [81, 82]*

$$s(n) = \begin{cases} \frac{1}{\sqrt{N}} \exp\left(-j \frac{2\pi\gamma}{N} \frac{n(n+2Q)}{2}\right), & N \text{ even}, \\ \frac{1}{\sqrt{N}} \exp\left(-j \frac{2\pi\gamma}{N} \frac{n(n+1+2Q)}{2}\right), & N \text{ odd}. \end{cases} . \tag{3.31}$$

where γ is integer such that the greatest common divisor $\gcd(\gamma, N) = 1$ and Q is arbitrary integer.

The discrete sequence forms in one cycle are shown in Figure 3.1 (left). Their main properties depend on their AC functions, shown in Fig. 3.1 (right). Note that, except for the Bjorck sequence (where the imaginary part is taken), we take the real part of all of them. Also note that, the Bjorck and Zadoff-Chu are part of the group of the so-called constant amplitude zero auto-correlation (CAZAC) sequences, since the side lobes of their periodic auto-correlation function are almost zero-valued [83, 84].

The absolute values of the ambiguity functions of the six sequences are shown in Fig. 3.2 (left). Even though Zadoff-Chu is a CAZAC sequence, showing good AC properties, it

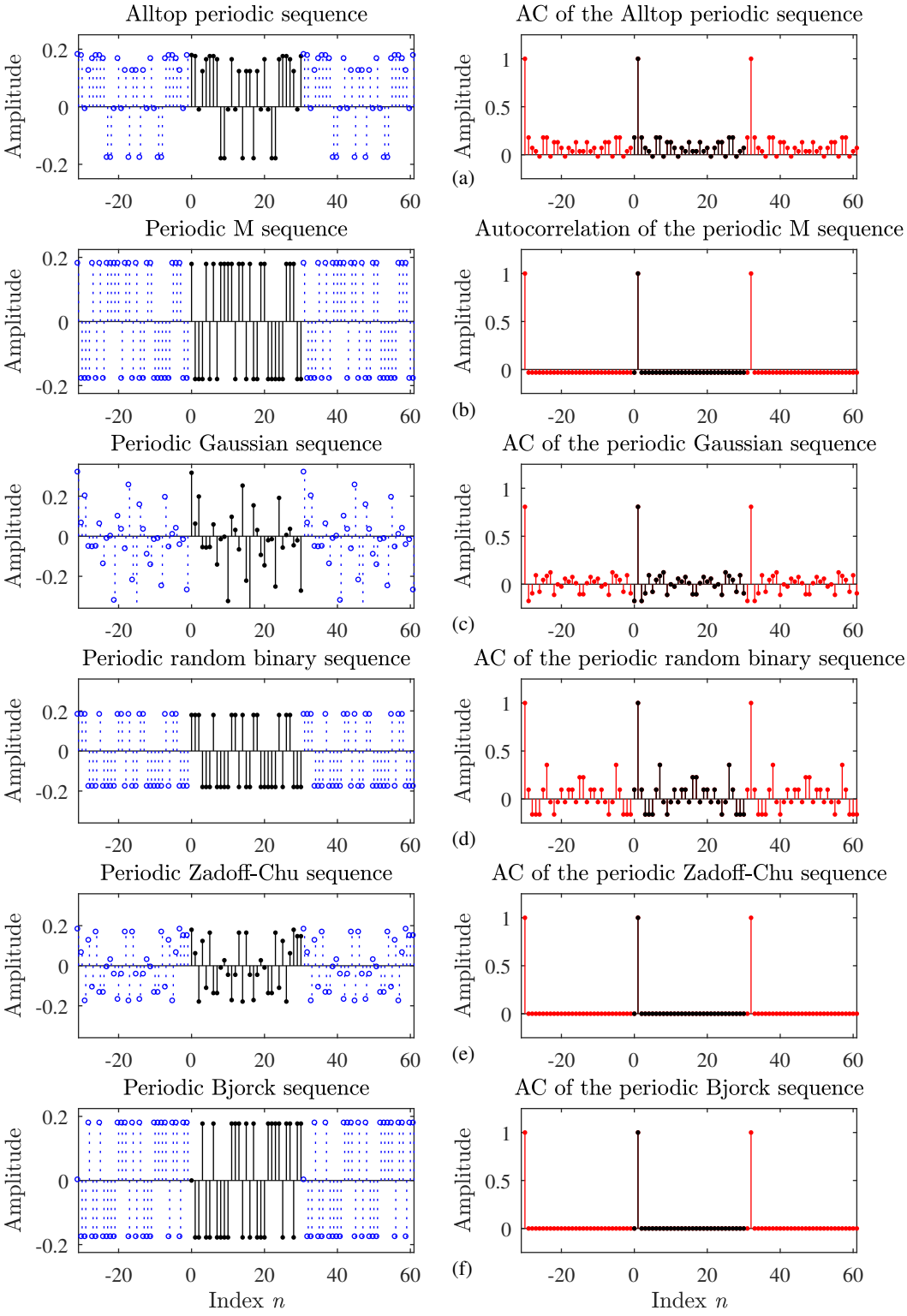

Figure 3.1: The transmitted disrete-time sequence forms $s(n)$ (left); The corresponding autocorrelation functions of the six sequences (right).

produces values $AF(m,r) = 1$ for $(m,r) \neq (0,0)$. It can be seen from Fig. 3.2 that it cannot be used for the analysis in the wideband sonar signal case. This will be further discussed. The sequence forms with a reduced set of measurements is shown in Fig. 3.2 (middle) and their corresponding AFs are shown in Fig. 3.2 (right).

3.2 Sequence selection

The selection of the sequences will be decided upon their reconstruction performances in various cases with different exhaustive statistical parameters. The sonar signal is represented by various number of components (sparsity level K) and different number of available measurements in a signal. Five cases for statistics were considered before taking the decision of the most convenient sequence form.

Case 1: Percentage of detected targets.

Since our goal is the right targetting of the objects, the first experiment is based on the precentage of detected components in the signals. Consider 1000 repetitions of the experiment using the signal of the form (3.1). We consider that the transmitted signal is of length $N = 31$, which is the equivalent to the number of available samples, i.e. $N_A = N$. The number of target components (which is equivalent to the sparsity level) is in the range $1 \leq K \leq 20$.

This case experimentally shows that the Zadoff-Chu sequence is not suitable for the detection of components. In the case when a small noise is present in the signals, the Bjorck and the M sequence show better results. In the case when the noise is high (i.e. SNR= 5dB and SNR=0dB), all sequences show similar results.

Case 2: Error calculation.

Many problems which can arise in practice will cause a signal to be nonsparse. The most realistic case is that the received signal is off the grid, making the targets randomly positioned. According to Chapter 2, for the sonar signal case, the theoretical error is

$$E_t = 10\log\Big(\big(\frac{K}{N_A}+1\big)\,\|\mathbf{g}-\mathbf{g}_K\|_2^2 + K\frac{N}{N_A}\sigma_\varepsilon^2\Big). \tag{3.32}$$

where $\mathbf{g}_K$ is the vector of the same length as $\mathbf{g}$, with the K nonzero targets at their positions and zero-valued everywhere else. The statistical error is calculated as

$$E_s = 10\log\big(\,\|\mathbf{g}-\mathbf{g}_R\|_2^2\,\big). \tag{3.33}$$

The test is performed with 100 random realizations of nonsparse images. The signal length is $N = 31$ with $K = 5$ target points. The available number of measurements is $N_A = N$. Table 3.1 presents the statistical and theoretical results for each sequence form and two different noise levels.

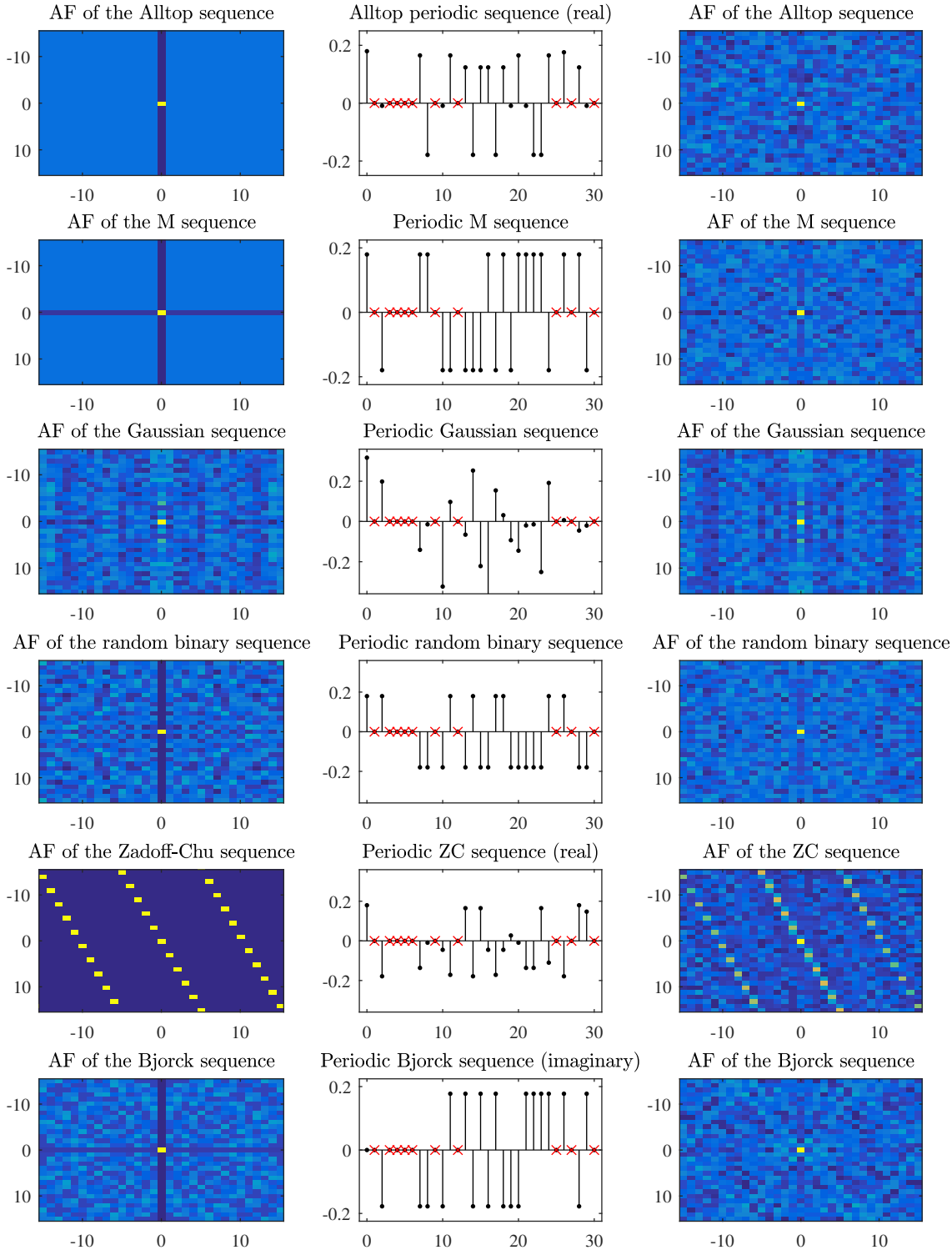

Figure 3.2: The ambiguity functions of the full sequences (left); Transmitted sequence forms with a reduced set measurements $N_A < N$ (middle); The AFs of the sequences with reduced set of available samples (right).

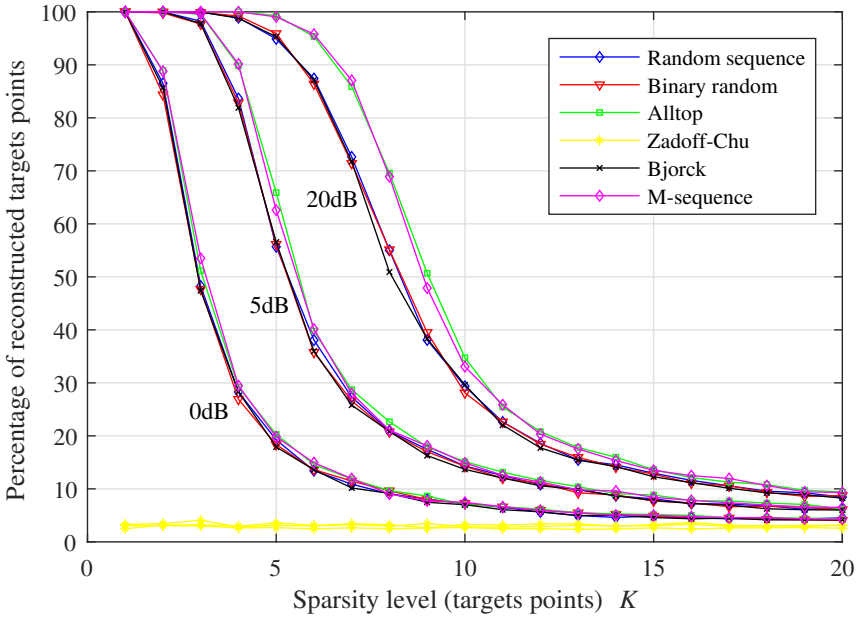

Figure 3.3: The percentage of successfully detected target positions in 1000 realizations, for $0 < K < 20$ and noise levels of SNRs$= 20, 5, 0$ dB.

Table 3.1: Average reconstruction error of nonsparse images with $K = 5$ target points, $N_A = N = 31$ and SNR$= 20, 5$dB.

SNR$= 20$dB	Gaussian	Binary	M seq.	Alltop	Bjorck
Statistics	-12.43	-12.35	-13.57	-13.42	-12.62
Theory	-12.35	-12.42	-13.62	-13.69	-12.88

SNR$= 5$dB	Gaussian	Binary	M seq.	Alltop	Bjorck
Statistics	-0.96	-0.88	-1.52	-1.37	-0.83
Theory	-0.83	-0.93	-1.61	-1.92	-1.01

Case 3: Robustness on number of available measurements.

In the previous cases we use $N_A = N$. Here, we will consider the number of available samples N_A that can be higher or lower than the length of the transmitted signal N. That is, we consider the case when $N_A \neq N$. Assume $N = 31$, with N_A varying as $N_A = 8, \ldots, 3N$, taking the prime numbers. The results in 100 realizations for the Bjorck, Alltop and M-sequence, are shown in Fig. 3.4, Fig. 3.5, and Fig. 3.6, respectively. For each sequence, noise levels of SNR$= 20, 5, 0$ dB are considered.

Case 4: Randomly positioned targets.

The three most robust sequence from the previous cases, Alltop, maximum-length and Bjorck, are further analyzed. Consider that six real targets are positioned randomly in an

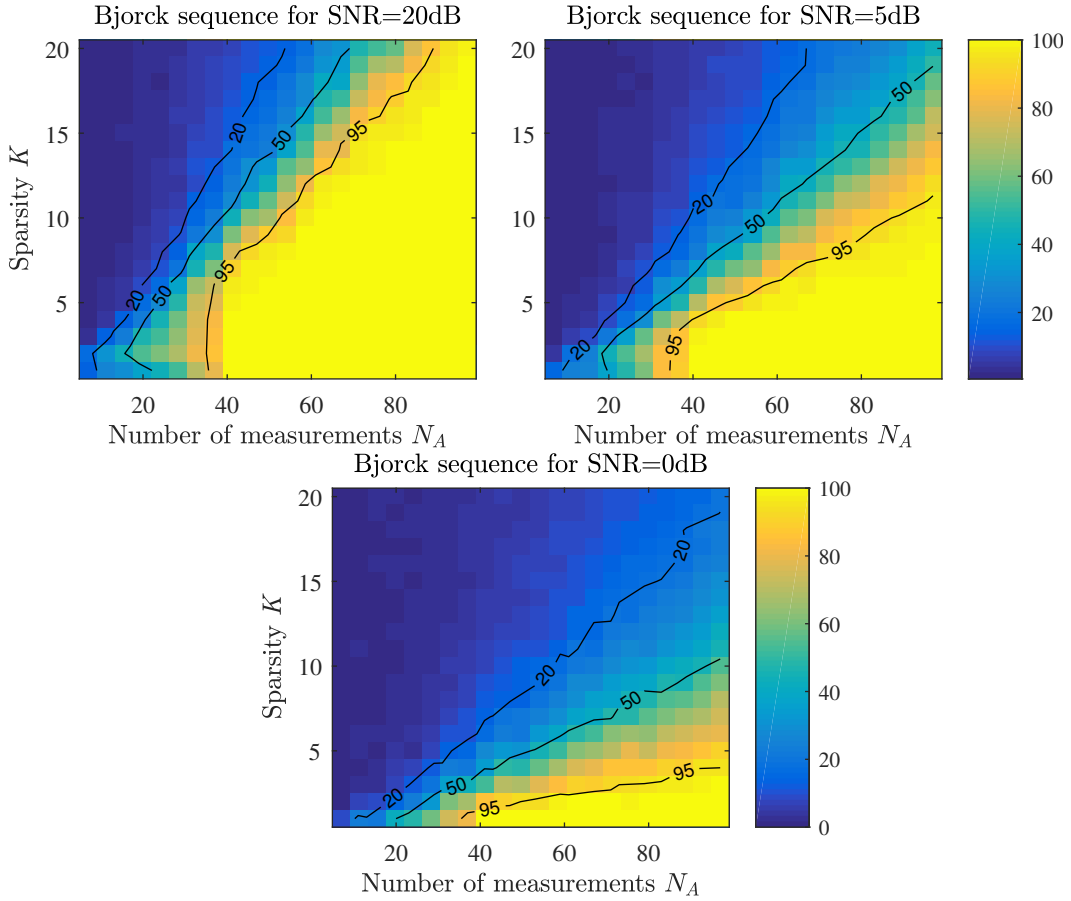

Figure 3.4: Successful reconstruction performance of the Bjorck sequence for different sparsity levels K, number of measurements taken N_A and noise levels with SNRs= $20, 5$ dB (upper row) and SNR=0 dB (lower row).

area of interest. More false targets are arriving due to different reasons, making the area nonsparse by nature. Additionally, the environment is noisy the level of SNR=10 dB. The noisy and nonsparse interest area is presented in Fig. 3.7 (top left). The reconstruction using the Bjorck sequence is illustrated in Fig. 3.7 (top right). The reconstruction when M sequence and Alltop sequences are used are presented in Fig. 3.7 (bottom).

Case 5: Real-world set-up.

In Fig. 3.8 (top left) an underwater boat set-up is modeled. We assume the sparsity level is the number of target points needed to model the boat. Assume the number is $K = 14$, as counted in Fig. 3.8 (top). Since the number of points is high, the sequence of length $N = 31$ cannot be used. The next available sequence length, satisfying the conditions for all three considered sequences (Alltop, Bjorck and M sequence) is $N = 127$. Assume a noise level of SNR=15 dB. The reconstruction when the M sequence is used is presented in Fig. 3.8 (top right). The reconstruction results with the Alltop and Bjorck sequences are shown in Fig. 3.8 (bottom).

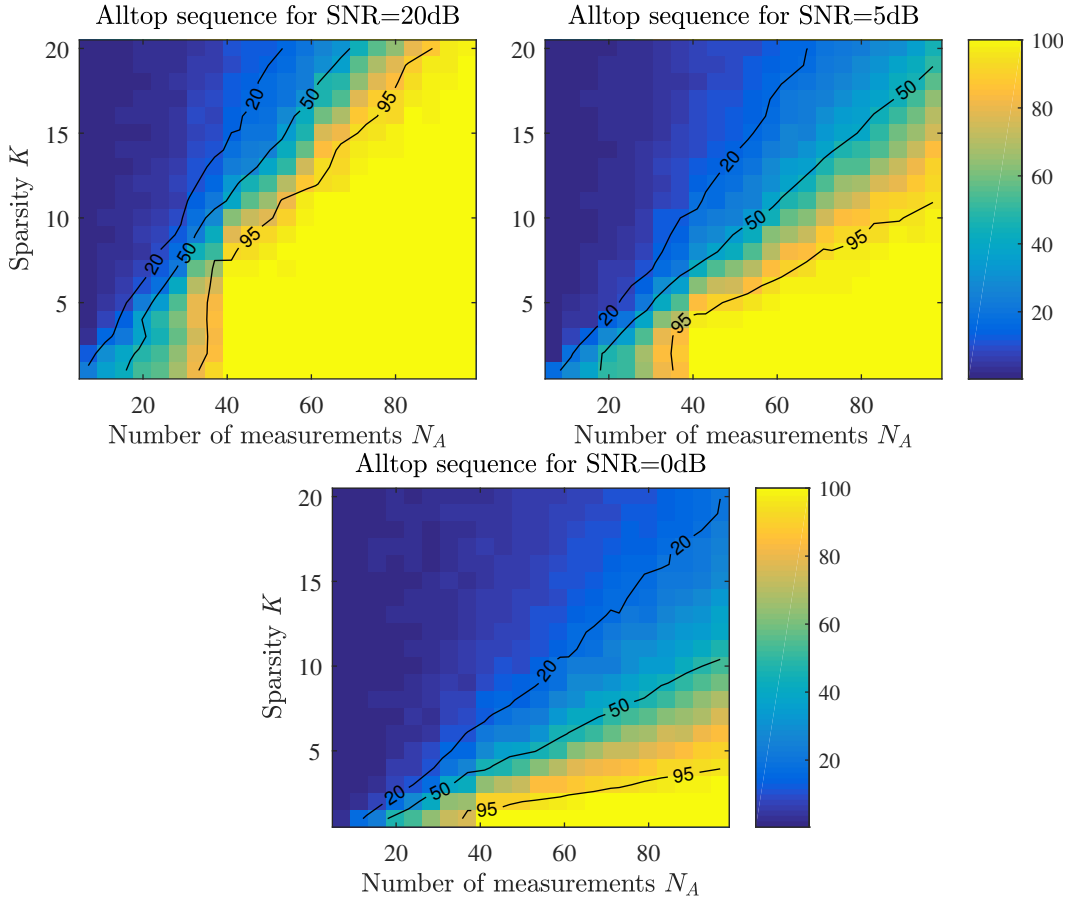

Figure 3.5: Successful reconstruction performance of the Alltop sequence for different sparsity levels K, number of measurements taken N_A and noise levels with SNRs= $20, 5$dB (upper row) and SNR=0dB (lower row).

3.3 Real-data reconstruction

In this section, the challenge of the real data is analyzed. In summary of Section 3.2, considering all cases, the Bjorck sequence resulted in the best solution for further work. Therefore, it will be used for the next experiments. It is concluded that the Zadoff-Chu sequence, due to its quadratic nature, failed in the reception and reconstruction. Also, the Alltop and M sequence performed very good and gave similar results. Therefore, for the practicality in the implementation, the Alltop and Bjorck sequences will be used for the next experiments.

An underwater experimental setup is created in the rooms of the GIPSA Laboratory at INP Grenoble. A water tank of 2 cubic meters was used for the experiment. An interferometer transducer is used for the transmission and reception of signals. The interferometer was supplied by the "ITER Systems" company from Annecy, France, with the operating frequency of 468 kHz, and 100 kHz bandwidth. Note that the sequences are modulated to satisfy the operating frequency range of the transducer. The transducer has one transmitter sensor and four receiver sensors. However, since the goal is to examine the robustness of the CS theory

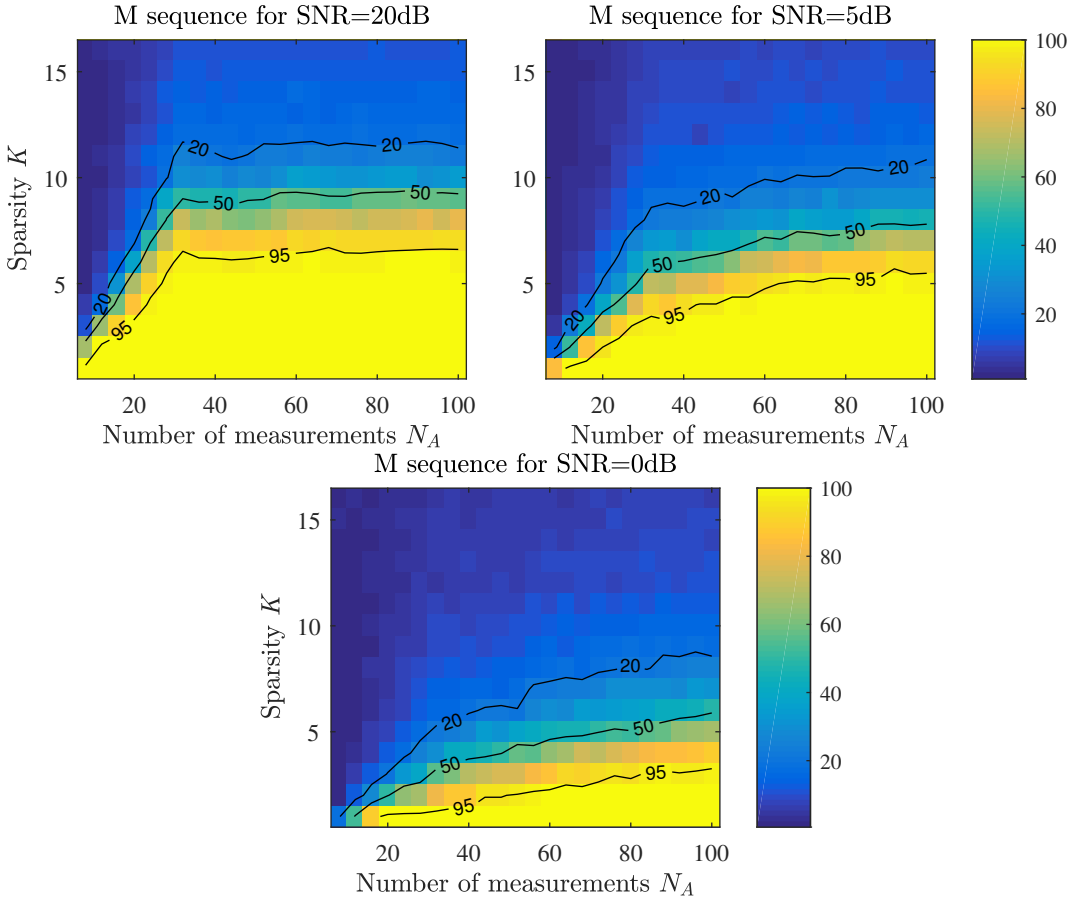

Figure 3.6: Successful reconstruction performance of the M sequence for different sparsity levels K, number of measurements taken N_A and noise levels with SNRs= $20, 5$dB (upper row) and SNR=0dB (lower row).

to the real data, the results will be analyzed from only one receiver. The transducer was fixed under the angle of 30^o close to the water surface. The setup of the water tank, and the individual instruments used for the experiment are presented in Fig. 3.9. The block diagram followed for the experiment is illustrated in Fig. 3.10. According to the block diagram, the setup includes steps such as the interpolation, modulation, filtering, and power amplifying of the sequence. When the signal is received, the CS methods are applied.

The target as in Fig. 3.9 (bottom left) was put at the tank floor. The position of the target to the transducer is illustrated in Fig. 3.11 and the real setup is shown in Fig. 3.9 (bottom right). The Alltop and the Bjorck sequences are transmitted, modulated and interpolated, as in Fig. 3.12. The received signals, when Alltop and Bjorck sequences are used, are shown in Fig. 3.13 (first two rows). For comparison, a chirp sequence as in [70] is transmitted also. The result, when the chirp sequence is used, is shown in Fig. 3.13 (third row). The reconstruction using the matched filter (MF) is shown in Fig. 3.13 (middle column). The reconstruction using the iterative version of the OMP algorithm is shown in Fig. 3.13 (right column).

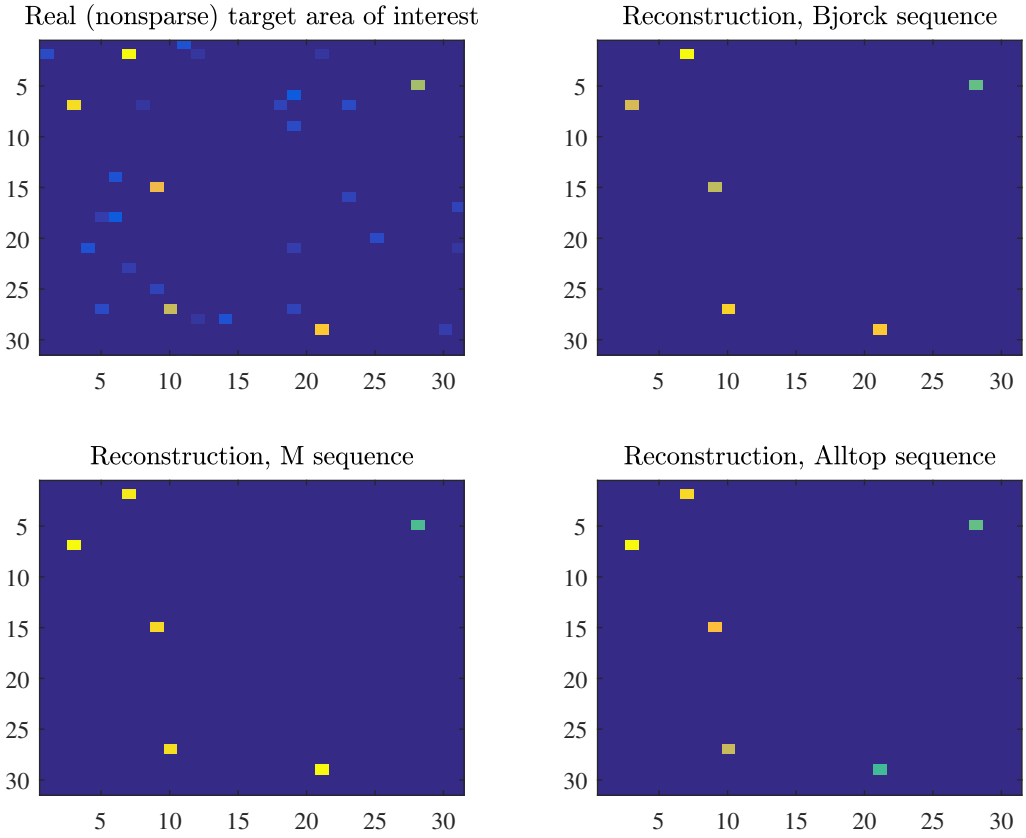

Figure 3.7: The reconstruction of a noisy nonsparse target area, with noise level of SNR=10dB and target points $K = 6$: The nonsparse area of interest (top right); Reconstruction when Bjorck sequence is used (top right), when M sequence is used (bottom left), and when Alltop sequence is used (top right).

3.4 Time-varying cross-range detection

In the examples considered in previous sections, the velocity is defined as constant, and therefore stationary. In more realistic cases, the cross-range (velocity) is varying and has to be detected so that the target can be successfully and truthfully found under this setup. If the cross-range parameter is misdetected, the exact position and velocity of the target will not be estimated accurately, leading to an incorrect reconstruction.

The time variations of target velocity can be written as $\nu+\alpha t$. Target velocity corresponds to the cross-range of the received signal. Having the received signal in the form

$$r(n) = \sum_{i=1}^{K} g_{k_i} \phi_{k_i}(n) \tag{3.34}$$

will have the basis functions as

$$\phi_{k_i}(n) = s(n - d_{k_i}) \exp\left(j\omega_{k_i} n + j\alpha_{k_i} n^2\right). \tag{3.35}$$

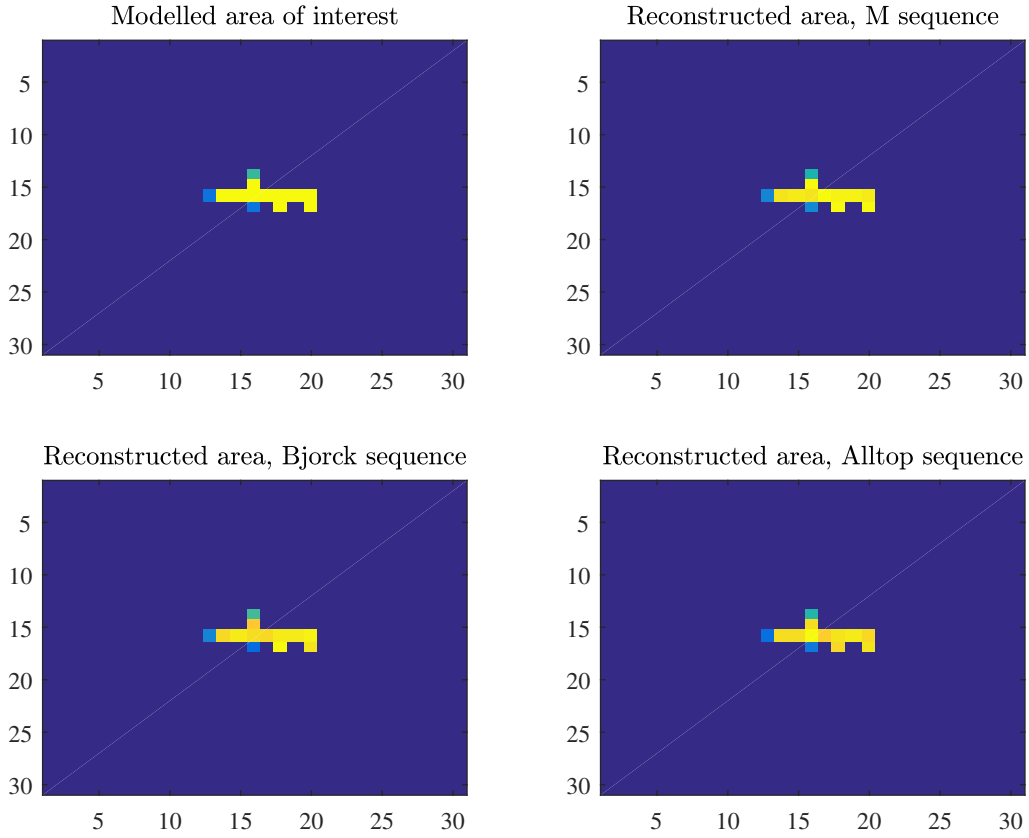

Figure 3.8: The reconstruction of an underwater boat set-up, with noise level of SNR=15dB and target points $K = 14$: The modelled area of interest (top right); Reconstruction when M sequence is used (top right), when Bjorck sequence is used (bottom left), and when Alltop sequence is used (top right).

According to (3.5), the basis function is

$$\phi_{p,q}(n) = s(n-p)\exp\left(j2\pi q\frac{n}{N} + j\alpha n^2\right). \tag{3.36}$$

for $(d_p, \omega_q) = (p, \frac{2\pi}{N}q)$. The elements of the measurement matrix are then

$$a_{k,l} = s(n_l - d_p)\exp\left(j\omega_q n_l + j\alpha n_l^2\right). \tag{3.37}$$

3.4.1 Decomposition and reconstruction

The technique for decomposition of targets in sonar signals is inspired by the idea of decomposition of time-varying signals using the polynomial Fourier transform (PFT) in [85]. The estimation of the parameter corresponding to the cross-range in wideband sonar signaks is the aim of this analysis. When $\alpha_i = \alpha$, the CS reconstruction will be successful. The parameter $\tilde{\alpha} \in \mathbf{a}$ in $\mu(k, k_i)$ is varied until the signal is maximally concentrated, i.e.,

$$\tilde{\alpha} = \arg\max_{(k,\alpha)} |g_{0\alpha}(k)|. \tag{3.38}$$

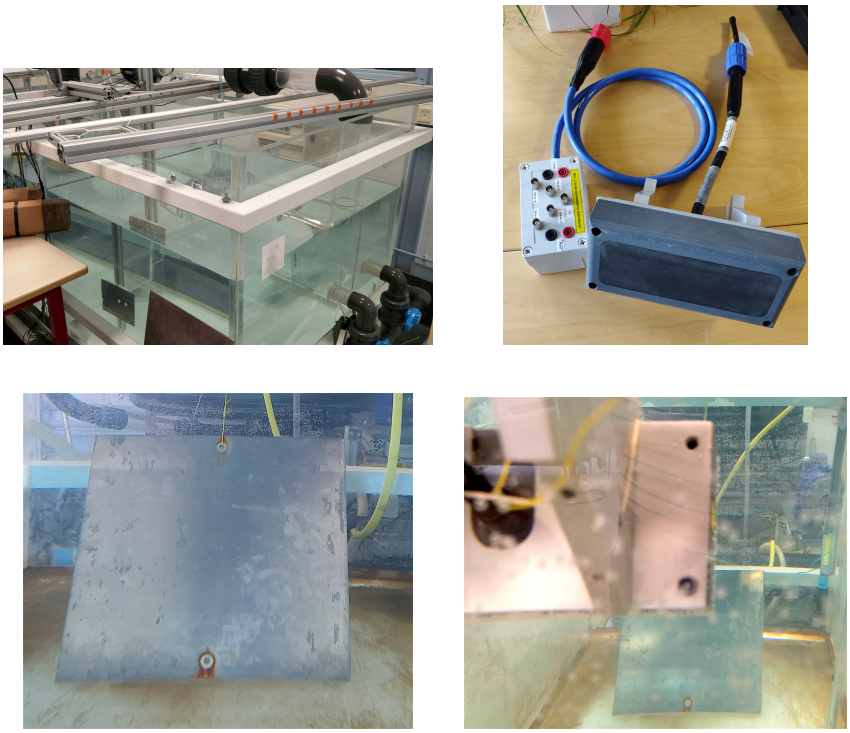

Figure 3.9: Real water tank setup: Water tank (top left); Transducer (top right); The shape of the target (bottom left); Position of the target and transducer in the water (bottom right).

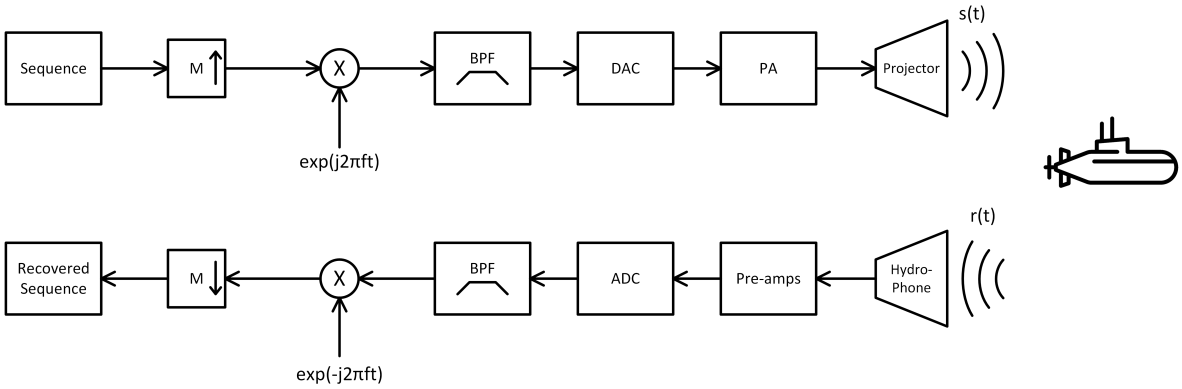

Figure 3.10: General block diagram of the experimental setup.

The solution of (3.38) is when $\tilde{\alpha}$ is equal or close to the true value of α. The set $\mathbf{a}$ represents the set of possible values for $\tilde{\alpha}$.

For more target points ($K > 1$), the procedure is as follows:

- The set of possible parameters $\mathbf{a}$ is defined.
- The initial estimate, $g_0(k)$, is calculated for each value $\tilde{\alpha} \in \mathbf{a}$.

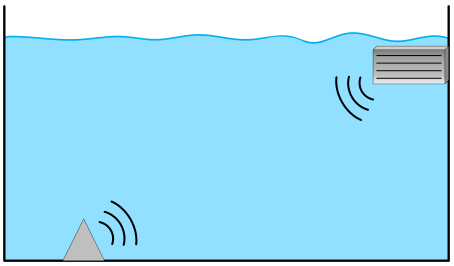

Figure 3.11: Illustration of the water tank setup: the position of the target to the transducer, with an elevation angle of 30^o.

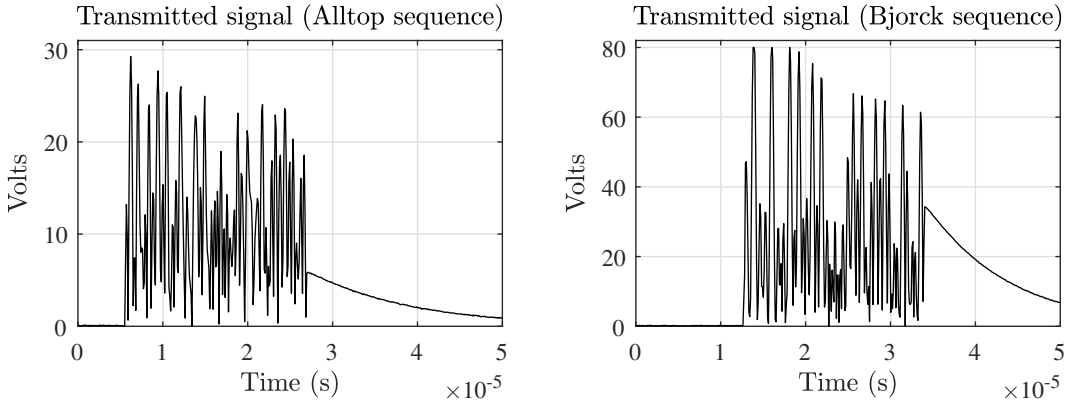

Figure 3.12: Real transmitted sequence forms, interpolated and modulated to operate under the transducer characteristics: Alltop sequence (left), and Bjorck sequence (right)

- The parameter $\tilde{\alpha}$ is found in such a way that the initial estimate is concentrated the best by using (3.38).
- The value of $\mu(k, k_i)$ is calculated using the determined parameter.
- The first component of $\mathbf{g}_R$ is reconstructed with $\mathbf{y}$ and $\mu(k, k_i)$.
- The reconstructed component is removed from the initial estimate, $\mathbf{g}_0 - \mathbf{g}_R$.
- The previous steps are repeated with the reconstructed component removed from $\mathbf{y}$, until all the parameters are determined and all K elements are reconstructed.

As an example, the analysis is performed using the Alltop sequence. The area of interest is nonsparse and noisy, with $K = 6$ important target points and SNR of 10 dB. The procedure is shown in Fig. 3.14. The original interest area is shown in Fig. 3.14 (top left). The reconstruction result is illustrated in Fig. 3.14 (bottom right). The steps of the initial estimates for each target point are presented in the remaining subplots of Fig. 3.14.

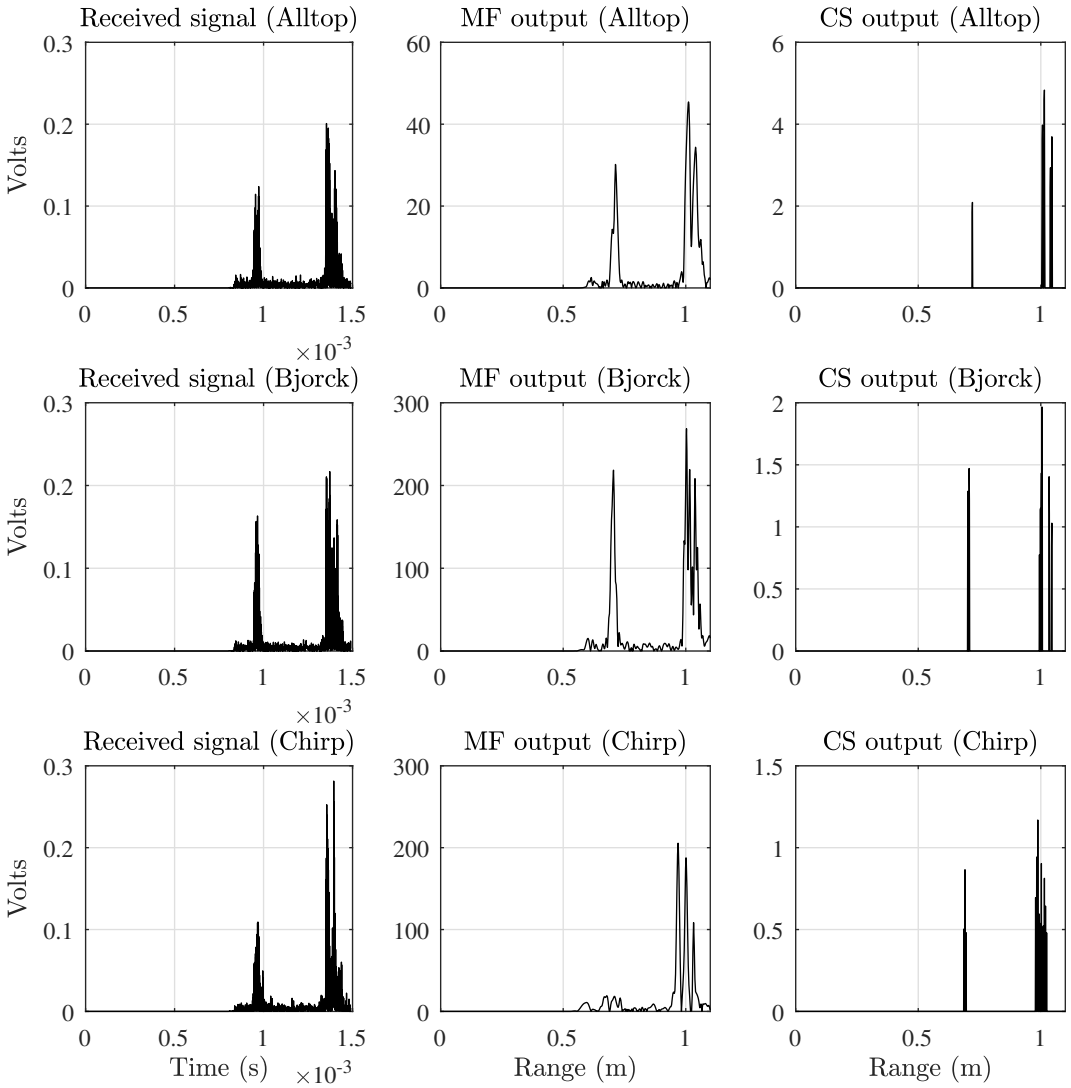

Figure 3.13: Received signal - real data: Received signals with different sequence forms (left), reconstruction with matched filter (middle), reconstruction with compressive sensing (right); when the Alltop sequence is transmitted (top); when the Bjork sequence is transmitted (middle); when the chirp sequence is transmitted (bottom).

3.5 High-resolution decomposition

Another issue in the decomposition of signals is the separation of closed components (targets). This can be solved by using high-resolution techniques developed for that matter. In practice, the high-resolution techniques are frequenlty used in the direct-of-arrival (DOA) estimation in the field of array signal processing [7, 85]. They can also be used in various engineering problems [7, 86–89], such as the misalignment of the sensors [90]. Two of the methods, which have shown in the literature to produce reliable results in separation, are Capon's method and Music Signal Classification (MUSIC) technique. They will be presented in the form that is

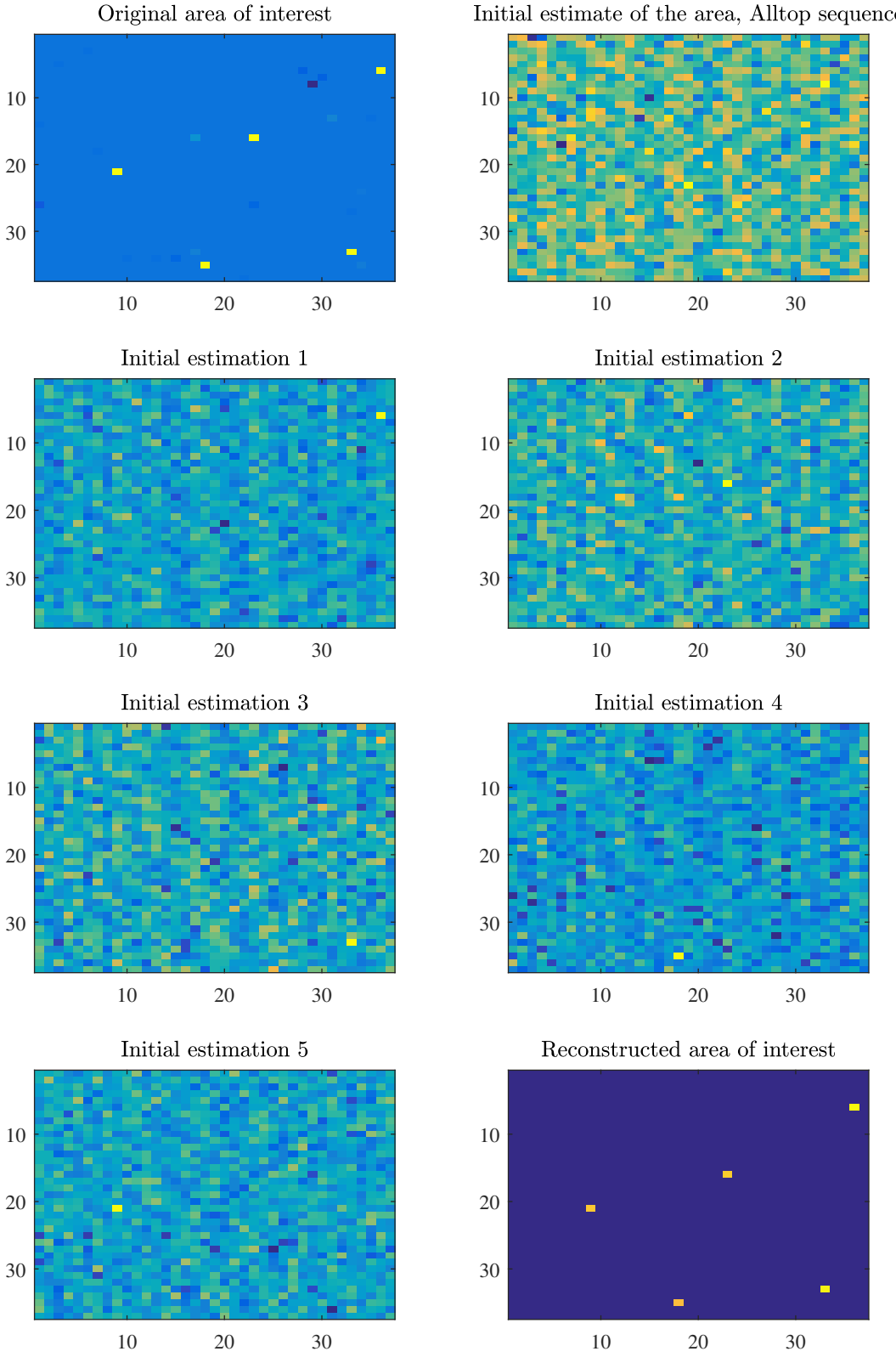

Figure 3.14: The reconstruction of a nonsparse target area, with $K = 6$ main target points.. The noise level of the area is SNR=10dB: Original nonsparse area (top left); Reconstructed target area (bottom right); Initial estimations for each target points (remaining subplots).

adjusted for implementation using the time-frequency representations.

3.5.1 Problem formulation

Consider a LFM signal as a common case of a transmitted signal form

$$s(t) = A(t) \exp\left(j2\pi(\Omega_0 t + c_h t^2)\right) \tag{3.39}$$

where $A(t)$ is the amplitude (slow-varying), Ω_0 is the initial frequency and c_h is the chirp rate. The discrete signal $s(n)$ with sampling interval Δt is of the form

$$s(n) = A(n\Delta t) \exp\left(j2\pi(n\Omega_0 \Delta t + n^2 c_h (\Delta t)^2)\right). \tag{3.40}$$

In Fig. 3.15, two schemes are presented. When the receiver is properly aligned with transmitter, as shown in Fig. 3.15 (a), the received signal will be an attenuated and delayed version of the transmitted signal. The problem arises when the receiver is not properly aligned with the transmitter. This is shown in Fig. 3.15 (b). The solid line represents how the signal was received, while the dashed line illustrates how the signal was supposed to be received.

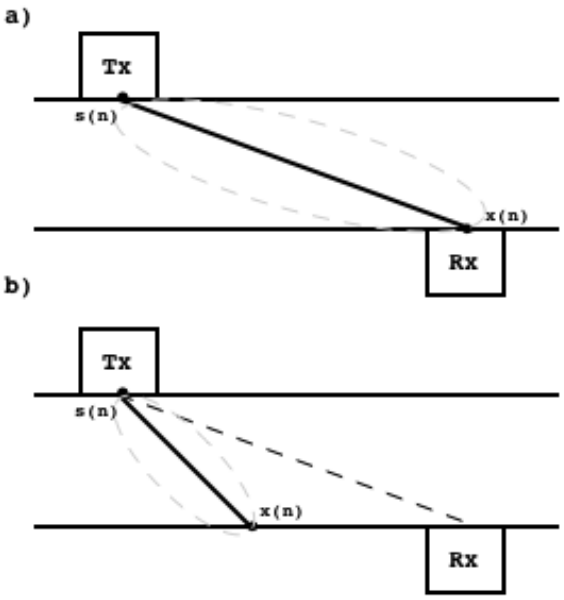

Figure 3.15: The positions of the sensor: when the sensor is properly aligned with the receiver (top); when the sensor is misaligned (bottom). Solid line represents the actually received signal.

The misalignment causes false estimation of positions of the physical sensors [90]. Also, vibrations in the environment can cause the sensors to misalign. The signal will then change through the channel due to the dispersive nature. The received signal will change in both

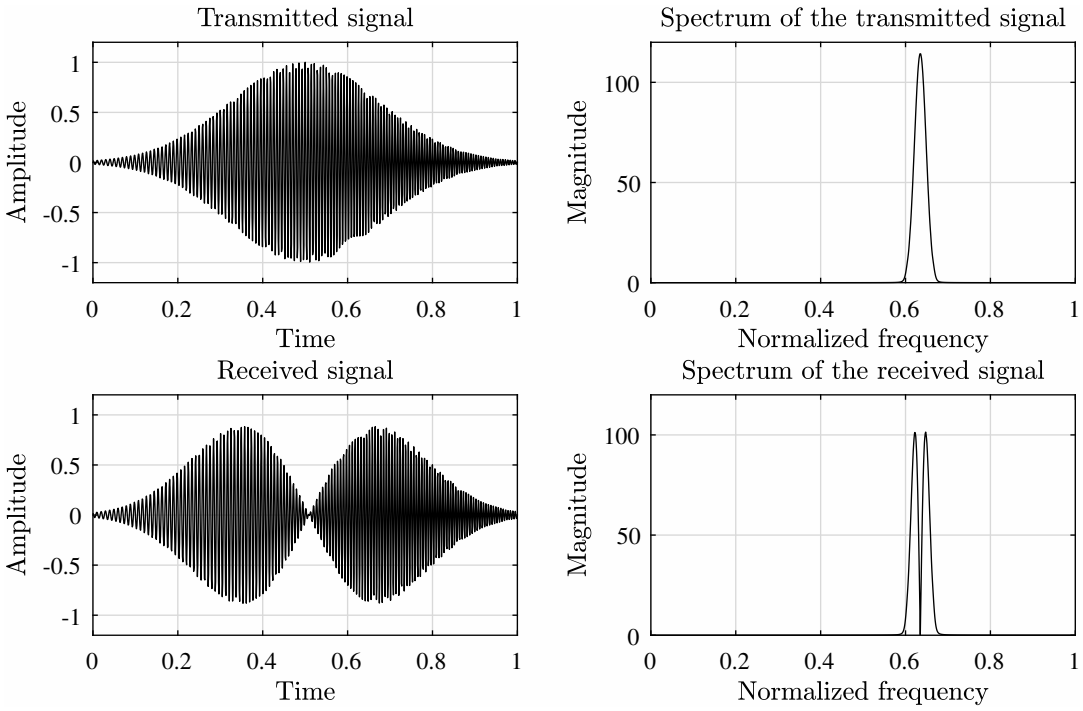

Figure 3.16: Transmitted signal with its spectrum (top); The received signal when the sensors are misaligned (bottom).

time and frequency. If the received signal is assumed from two propagation paths, it will be received as

$$r(n) = s_r(n) * h_1(n) + s_r(n) * h_2(n) \tag{3.41}$$

where $'*'$ is the convolution of $s_r(n)$ with two transfer functions $h_1(n)$ and $h_2(n)$, coming from the two propagation paths, respectively.

In general case, for two transfer functions, the received signal consists of two components. For $t_1 \approx t_2$, the recieved signal is a modulated version of the transmitted signal, i.e.,

$$r(t) \approx 2A(t)\cos\big(2\pi c(t_1 - t_2)t + \phi_1\big)\cos\big(2\pi(\Omega t + ct^2)\big). \tag{3.42}$$

A special case is when the recieved signal is consists of two time-shifted versions of the transmitted signal

$$r(t) = s_r(t - t_1) + s_r(t - t_2). \tag{3.43}$$

The signal, with its corresponding spectrum, is presented in Fig. 3.16 (top). The received signal and its corresponding DFT domain, are shown in Fig. 3.16 (bottom). As seen, the two received components are closely positioned in both time and frequency. The aim is to separate them in order to successfully reconstruct the original (transmitted) signal. Note that the signal attenuation is neglected since our main interet is the signal form, which will make the calculation of the attenuation caused during the transmission easier.

3.5.2 High-resolution techniques

Recall the normalized STFT with a rectangular window of the width N

$$STFT(\omega, n) = \frac{1}{N}\sum_{m=0}^{N-1} x(n+n_w)e^{-j\frac{2\pi}{N}n_w\omega} = \frac{1}{N}\mathbf{a}^H(\omega)\mathbf{x}(n), \tag{3.44}$$

where the vector notation of the basis functions and the signal are

$$\mathbf{a}(\omega) = [1, e^{-j\omega}, e^{-2j\omega}, \ldots, e^{-(N-1)j\omega}]^T$$
$$\mathbf{x}(n) = [x(n), x(n+1), \ldots, x(n+N-1)]^T.$$

Note that the value ω is introduced instead of $\frac{2\pi}{N}k$ to increase the frequency axis density in order to achieve high resolution.

Definition 3.7
*The **averaged Capon's STFT** is defined as [91, 92]*

$$S_{CAPON}(n, \omega) = \frac{1}{\mathbf{a}^H(\omega)\hat{\mathbf{R}}_x^{-1}(n)\mathbf{a}(\omega)} \tag{3.45}$$

where

$$\hat{\mathbf{R}}_x(n) = \frac{1}{N}\sum_n \mathbf{x}(n)\mathbf{x}^H(n), \tag{3.46}$$

is the autocorrelation matrix over N samples (ergodicity over N samples around n is assumed), which comes from the power of the signal in the STFT representation domain.

By the eigenvector decomposition, the autocorrelation matrix can be written as

$$\hat{\mathbf{R}}_x(n) = \frac{1}{N}\sum_n \mathbf{x}(n)\mathbf{x}^H(n) = \mathbf{\Lambda}(n)\mathbf{V}^H(n), \tag{3.47}$$

where $\mathbf{\Lambda}(n)$ is the diagonal matrix with eigenvalues on its diagonals and $\mathbf{V}(n)$ is the matrix whose columns are eigenvectors of the matrix $\hat{\mathbf{R}}_x(n)$.

Definition 3.8
*The **averaged MUSIC STFT** is defined as [93]*

$$S_{MUSIC}(n, \omega) = \frac{1}{\mathbf{a}^H(\omega)\mathbf{V}_{S_e}^H(n)\mathbf{V}_{S_e}(n)\mathbf{a}(\omega)} \tag{3.48}$$

where $\mathbf{V}_{S_e}(n)$ is the eigenvector matrix with S_e eigenvectors with lowest S_e eigenvalues.

For a signal with time-varying component, the local form of the PFT and corresponding STFT (local polynomial FT - LPFT) should be used with any of the high-resolution techniques [7]. Let us consider a signal with quadratic phase

$$x(n) = Ae^{j(\alpha_0 n^2 + \omega_0 n + \phi_0)}. \tag{3.49}$$

As in the case of polynomial Fourier transform, the Capon high-resultion method can be further expanded to the LPFT by calculating the autocorrelation matrix with a signal multiplied by an exponential factor $\exp(-j\alpha n_w^2)$, i.e.

$$x_\alpha(n_w) = x(n_w)e^{-j\alpha n_w^2}. \tag{3.50}$$

The parameter α is estimated as the maximal concentration value of

$$LPFT_\alpha(k,n) = \frac{1}{N}\mathbf{a}^H(\omega)\mathbf{x}_\alpha(n) \tag{3.51}$$

as

$$\alpha = \arg\max_\alpha |LPFT_\alpha(\omega,n)|. \tag{3.52}$$

For the optimization of the parameter, we can use the concentration measures such as $\alpha = \arg\min_\alpha ||LPFT_\alpha(\omega,n)||_1$. Since the LPFT is biased in amplitude when greatly concentrated, it would not be appropriate to use it for the concentration comparison of different parameters α. Therefore, for the comparison, the standard LPFT is used. The local AC function is calculated using a sliding window function with the optimally found parameter α

$$\hat{\mathbf{R}}_x(n,N_w,\alpha) = \frac{1}{N_w+1}\sum_{n_w=n-N_w/2}^{n+N_w/2}\mathbf{x}_\alpha(n_w)\mathbf{x}_\alpha{}^H(n_w) \tag{3.53}$$

where N_w is the width of a symmetric sliding window.

Definition 3.9
The optimal ***local Capon's representation*** *is defined by [7, 92]*

$$LPFT_{CAPON}(n,\omega) = \frac{1}{\mathbf{a}^H(k)\hat{\mathbf{R}}_x^{-1}(n,N_w,\alpha)\mathbf{a}(\omega)}. \tag{3.54}$$

In the same way, the local representation of the MUSIC algorithm can be presented by using the eigenvectors of the autocorrelation function of the windowed signal $x(n_w)$.

3.5.3 Examples

Assume that a signal of the form (3.40) is transmitted, with frequency range between $f_{min} = 40$ Hz and $f_{max} = 98$ Hz, sampled at frequency $f_s = 1024$ Hz. The decomposition of the signal is performed and compared using the standard, Capon's and MUSIC spectrogram, together with their local forms. A rectangular window is used for the analysis of local forms. The window is of length $N_w = 64$. For the MUSIC calculation, we have used the $S_e = 100$ lowest eigenvectors for the STFT decomposition, and $S_e = 2$ for each windowed function in the LPFT decomposition. The decomposition of the signal is presented in Fig. 3.17. An one time-instant of Fig. 3.17 is presented in Fig. 3.18, where it is visible that the two components can be separated using the local forms of Capon's and MUSIC high-resolution techniques.

From Fig. 3.17, it can be seen that two components are successfully separated by the local forms of the high-resolution techniques, i.e. Capon's and MUSIC, while other approaches

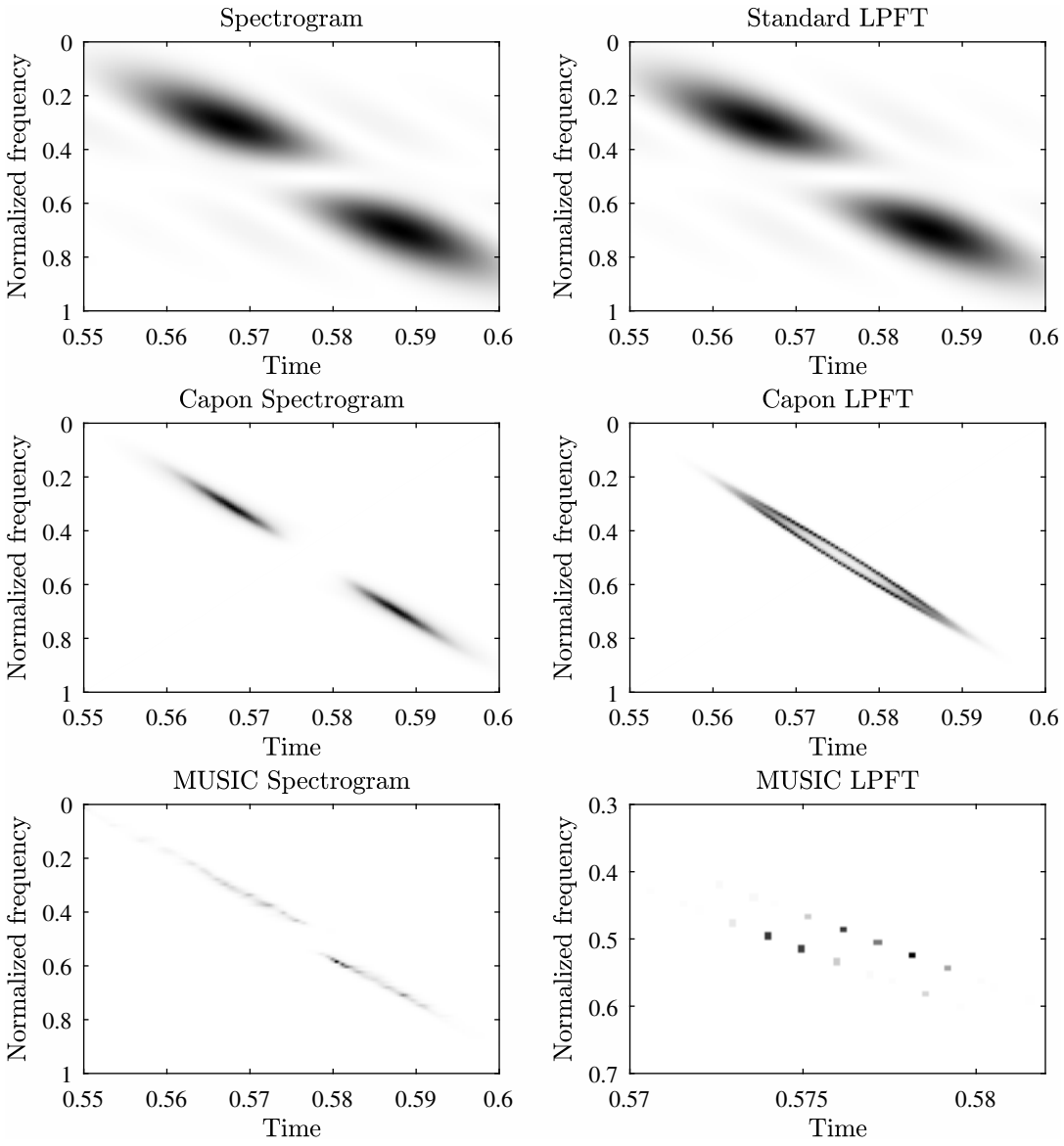

Figure 3.17: Decomposition of the signal using high-resolution techniques: standard STFT, i.e., the spectrogram (top left), standard LPFT (top right), Capon's STFT (middle left), and Capon's LPFT (middle right), standard MUSIC STFT (bottom left), and MUSIC LPFT (bottom right).

result in aa modulated single component signal. The local MUSIC representation shows the best result in the sense of distinguishing the two components. However, the local Capon's representation is much stronger and computationally more efficient for any further analysis.

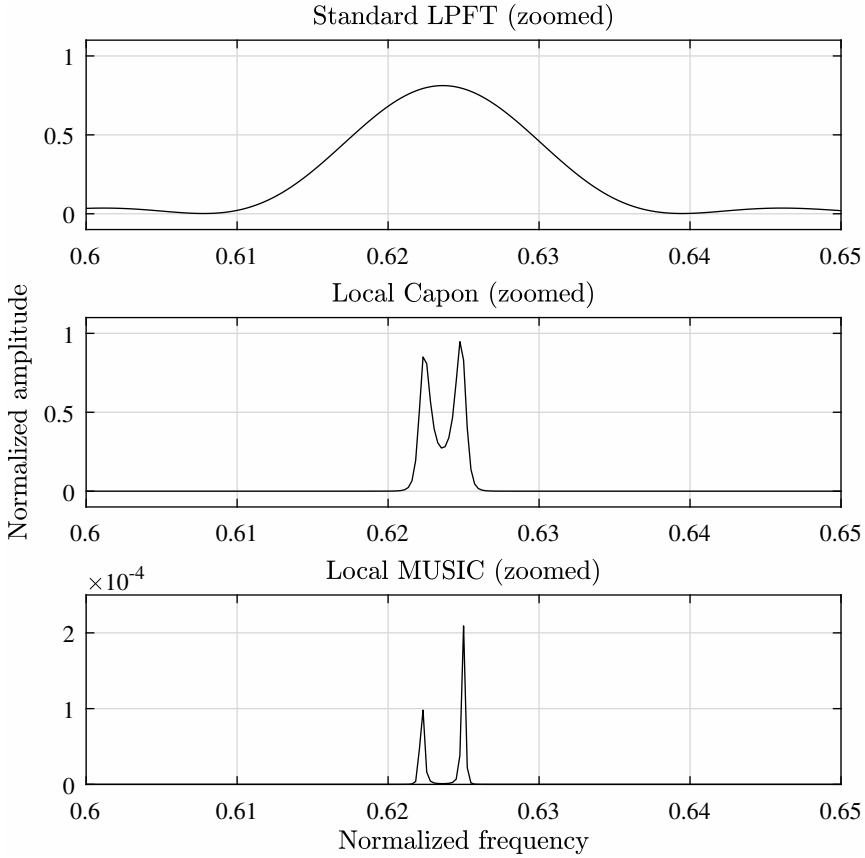

Figure 3.18: The spectrum of one time-instant (zoomed) in the standard LPFT (top); in the local Capon's representation (middle) and in the local MUSIC representation (bottom).

Chapter 4

Decomposition in dispersive channels

Contents

The decomposition and reconstruction of signals transmitted through a dispersive channels are analyzed in this Chapter. Dispersive channels are characterized by multi-component and multi-phase signals, even when the transmitted signal is of a simple form. The problem of the decomposition and localization of signal component in dispersive channels is an intensively studied research topic. The warping techniques have showed interesting and promising results in the decomposition and reconstruction of normal modes of the signal. The characterization of the signal propagating trough dispersive channels was also analyzed in [94]. The problem of localization of these signal using the phase-continuity of the signals was studied in [95].

After the transmission through a dispersive environment, the signal consists of several components called modes. These modes are non-stationary due to frequency dependent properties of the media for signal propagation. Therefore, the standard Fourier transform is not suitable for the implementation on such signals. Since the frequency variations can be approximated by a polynomial function, the natural choice for the methods developed in this thesis is the polynomial Fourier transform (PFT). Since the number of important modes is small, the non-stationary signals in dispersive channels can be considered as sparse in the PFT domain. The analysis of the sparse signals in the PFT domain is quite specific since the transformation basis functions are not orthogonal [96]. After the PFT analysis, it has be found that the dual form of the PFT is a more appropriate domain for the analysis of the

signal in dispersive channels. This form of the PFT is examined and the sparsity property is employed reconstructing the signal with a small number of available samples.

Since the dual PFT is only an approximation of the signal modes, the next step was to use the exact normal mode form as the sparsity domain and the domain of analysis of dispersive channel signals. Therefore, the second considered approach is based on the decomposition of the exact modes of the dispersive channel signals. The modal-function based decomposition is adapted and used in the analysis at last.

4.1 Shallow water theory and dispersive channels - background

Shallow waters are of great research interest for many years [94, 97–108]. Typically, shallow waters are defined by the depth of the sea/ocean which is not greater than $D = 200$ meters. Also, signals traveling through water have a faster speed than signal traveling through air (where the speed is $c = 380\text{m/s}$). The exact speed of sound in water depends on many factors such as the salinity or the temperature of the water, but it can be generally approximated at $c = 1500\text{m/s}$. This, consequently, makes their wavelengths λ much shorter, usually $D \gg \lambda$, with D being the shallow water channel depth. The reason they attract the researches is the extremely complex analysis of such setups.

The complexity of the problem depends on many factors, such as the volume and bottom properties. Further, the noise in shallow water occurs due to the many activities happening on the coastlines and surface of the sea, which causes cavitations in the sea itself. Thus, it can be concluded that shallow waters are more dispersive than deep waters. Dispersivity occurs in underwater channels due to the roughness of the bottom, the strength of the waves, the cavity level of the water and many other reasons. The main characteristics of dispersive channels is that they are frequency dependent. The frequency characteristics (phase and spectral content) change during the transmission of the signal.

The propagation of sound in shallow water environment is mathematically represented by the wave equations. For the analysis, let consider the wave equation of the displacement potential ψ in free space [99, 109]

$$\nabla^2\psi + \frac{1}{c^2}\frac{\partial\psi}{\partial t^2} = 0, \tag{4.1}$$

where ∇ presents the Laplacian operator for the considered coordinate system. If the Cartesian coordinate $\mathbf{r} = (x, y, z)$ system is assumed, the Laplacian operator is defined by

$$\nabla^2\psi = \frac{\partial^2\psi}{\partial x^2} + \frac{\partial^2\psi}{\partial y^2} + \frac{\partial^2\psi}{\partial z^2}. \tag{4.2}$$

Accordingly, for the cylindrical coordinates system, with coordinates (r, θ, z), the Laplacian operator will be

$$\nabla^2 = \frac{1}{r}\frac{\partial}{\partial r}\left(r\frac{\partial}{\partial r}\right) + \frac{1}{r^2}\frac{\partial^2}{\partial\theta^2} + \frac{\partial^2}{\partial z^2}. \tag{4.3}$$

It is usual in the theory that the displacement potential is not azimuth dependent, reducing the analysis from (r, θ, z) to (r, z).

If we assume a pressure term of a point source (for example, an underwater source, i.e., a target), the wave equation becomes inhomogeneous

$$\nabla^2 \psi(\mathbf{r}, t) - \frac{1}{c^2} \frac{\partial^2 \psi(\mathbf{r}, t)}{\partial t^2} = f(\mathbf{r}, t), \tag{4.4}$$

where $f(\mathbf{r}, t)$ presents the volume injection in coordinate system $\mathbf{r}$ at time t. Using the Fourier transform pair

$$f(t) = \frac{1}{2\pi} \int_{-\infty}^{\infty} F(\omega) e^{-j\omega t} d\omega \tag{4.5}$$

$$F(\omega) = \int_{-\infty}^{\infty} f(t) e^{j\omega t} dt \tag{4.6}$$

we can get a frequency and space domain wave equation

$$\nabla^2 \Psi(\mathbf{r}, \omega) + \frac{\omega^2}{c^2} \Psi(\mathbf{r}, \omega) = F(\mathbf{r}, \omega), \tag{4.7}$$

where $\Psi(\mathbf{r}, \omega)$ is the Fourier transform of $\psi(\mathbf{r}, t)$ and $F(\mathbf{r}, \omega)$ is the Fourier transform of $f(\mathbf{r}, t)$. Note that the Fourier transform of $\frac{\partial^2 \psi(\mathbf{r}, t)}{\partial t^2}$ is equal to $-\omega^2 \Psi(\mathbf{r}, \omega)$. Using the notation

$$k = \frac{\omega}{c}, \tag{4.8}$$

the Helmholtz equation

$$\nabla^2 \Psi(\mathbf{r}, \omega) + k^2 \Psi(\mathbf{r}, \omega) = F(\mathbf{r}, \omega), \tag{4.9}$$

is obtained.

As an example, we can consider a plane in the Cartesian coordinates along x-axis, which does not depend on the coordinates x and z, when the wave equation Eq. (4.9) with $F(\mathbf{r}, \omega) = 0$, assumes the form

$$\frac{\partial^2 \Psi(x, \omega)}{\partial x^2} + k^2 \Psi(x, \omega) = 0. \tag{4.10}$$

It results in the solution

$$\Psi(x, \omega) = A e^{jkx} + B e^{-jkx} \tag{4.11}$$

where $k = \omega / c$ is the wave vector as in Eq. (4.8). When $B = 0$, the wave is propagating directly in direction of $\mathbf{r}$. When $A = 0$, the wave propagates against the direction $\mathbf{r}$ [99, 109].

In the cylindrical case, if we assume that only the range r changes, the homogeneous wave equation reduces to

$$\left[\frac{1}{r} \frac{\partial}{\partial r} \left(r \frac{\partial}{\partial r} \right) + k^2 \right] \Psi(r, \omega) = 0 \tag{4.12}$$

resulting in Bessel functions

$$\Psi(x, \omega) = A J_0(kr) + B Y_0(kr) \tag{4.13}$$

The result can be related to the Hankel functions as

$$\Psi(x,\omega) = CH_0^{(1)}(kr) + DH_0^{(2)}(kr) \tag{4.14}$$

$$= C[J_0(kr) + jY_0(kr)] + D[J_0(kr) - jY_0(kr)], \tag{4.15}$$

where

$$H_0^{(1)}(kr) \approx \sqrt{\frac{2}{\pi kr}} e^{j(kr-\pi/4)} \tag{4.16}$$

$$H_0^{(2)}(kr) \approx \sqrt{\frac{2}{\pi kr}} e^{-j(kr-\pi/4)}. \tag{4.17}$$

These results can be approximated as

$$\Psi(r,\omega) = A\frac{e^{jkr}}{r} + B\frac{e^{-jkr}}{r}. \tag{4.18}$$

Assuming only direct wave (when $B = 0$), we can write that

$$\Psi(r,\omega) = A\frac{e^{jkr}}{r}, \tag{4.19}$$

and, by using the derivation of the surface displacement [99], calculate that

$$\Psi(r,\omega) = -S_\omega \frac{e^{jkr}}{4\pi r}, \tag{4.20}$$

where S_ω is the strength of the source. Note that

$$g_\omega(r,0) = \frac{e^{jkr}}{4\pi r} \tag{4.21}$$

is the definition of the Green's function. For a source at $\mathbf{r}_t = (r_t, z_t)$, the general Green's function is defined by

$$g_\omega(\mathbf{r},\mathbf{r}_t) = \frac{e^{jk|\mathbf{r}-\mathbf{r}_t|}}{4\pi|\mathbf{r}-\mathbf{r}_t|}. \tag{4.22}$$

4.1.1 Normal mode solution

In the underwater acoustics, there are four main methods of deriving the solution for a wave equation: fast field program, normal modes, ray theory, and the parabolic equation model [99,104]. In this thesis, normal mode solution will be analyzed, as one of the most widely used solutions in underwater acoustics. It is based on solving depth-dependent equations using the method of variable separation.

The general model of the environment is presented in Fig. 4.1. The boundary of the bottom depends on the nature of the ocean, such as the roughness, depending on the weather conditions and different environment in the ocean itself. This will introduce more layers of the seabed. Also, the scattering of the transmitted signal can cause a non-ideal environment for

the analysis. The isovelocity waveguide model, which is presented in Fig. 4.2, characterizes a rigid boundary of the seabed. This yields to an ideally spread velocity of c. All channel models are based on the fact that the structure of the channel is a waveguide, with multiple normal-modes received, representing delayed versions of the transmitted signal. The goal is to estimate and decompose the received signal, by finding each mode separately.

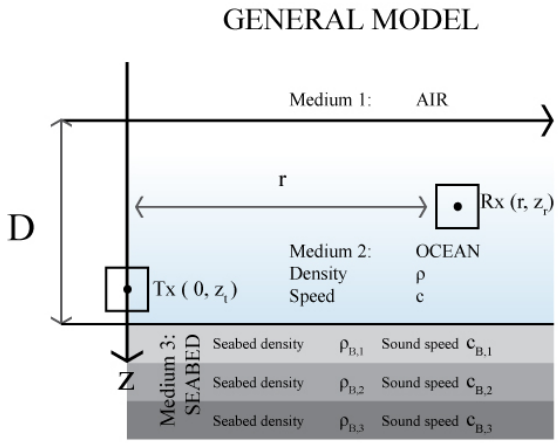

Figure 4.1: The general model of a shallow water environment [106].

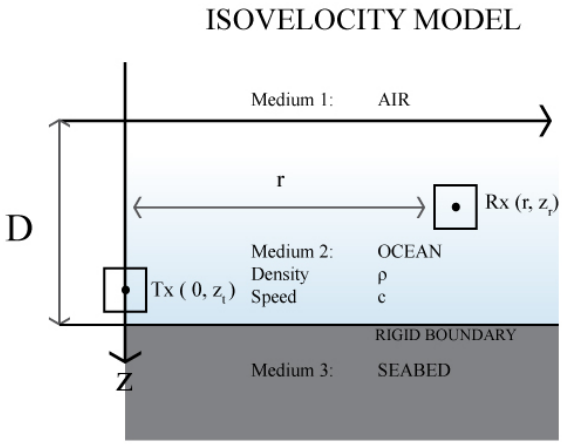

Figure 4.2: The isovelocity model of a shallow water environment [106].

The one-point received pressure field y from a point source located at depth z_t and range $r = 0$ is defined by the Helmoltz equation

$$\frac{1}{r}\frac{\partial}{\partial r}\Big(r\frac{\partial y}{\partial r}\Big) + \rho(z)\frac{\partial}{\partial z}\Big(\frac{1}{\rho(z)}\frac{\partial y}{\partial z}\Big) + \frac{\omega^2}{c^2(z)}y = -\frac{\delta(r)\delta(z-z_t)}{2\pi r}. \tag{4.23}$$

Using the method of variable separation, we can write the pressure as product of two functions one dependent on range r and another one dependent on depth z

$$y(r,z) = Q(r)G(z). \tag{4.24}$$

By substituting this form into Eq. (4.23) and considering only its homogeneous part, we get

$$\frac{1}{Q}\left[\frac{1}{r}\left(r\frac{dQ}{dr}\right)\right]+\frac{1}{G}\left[\rho(z)\frac{d}{dz}\left(\frac{1}{\rho(z)}\frac{dG}{dz}\right)+\frac{\omega^2}{c^2(z)}G\}\right]=0. \tag{4.25}$$

Note that this equation has two terms $\frac{1}{Q}\left[\frac{1}{r}\left(r\frac{dQ}{dr}\right)\right]$ and $\frac{1}{G}\left[\rho(z)\frac{d}{dz}\left(\frac{1}{\rho(z)}\frac{dG}{dz}\right)+\frac{\omega^2}{c^2(z)}G\}\right]$. The first term is a function of coordinate r only, while the second term is a function of coordinate z only. Their sum can be zero only if both of them are constant and do not depend on r and z. This constant is called the separation constant and denoted by k_{rm}^2, where m presents the mode index.

Now, by equating the second part of the last wave equation with this constant k_{rm}^2 we get

$$\frac{1}{G_m}\left[\rho(z)\frac{d}{dz}\left(\frac{1}{\rho(z)}\frac{dG_m}{dz}\right)+\frac{\omega^2}{c^2(z)}G_m\right]=k_r^2(m,\omega) \tag{4.26}$$

or

$$\rho(z)\frac{d}{dz}\left[\frac{1}{\rho(z)}\frac{dG_m(z)}{dz}\right]+\left[\frac{\omega^2}{c^2(z)}-k_{r,m}^2(m,\omega)\right]G_m(z)=0. \tag{4.27}$$

Note that $G(0)=0$ and $\frac{dG}{dz}|_{z=D}=0$, where D is the ideal rigid bottom. It is interesting to note that the modal equation is a Sturm-Liouville problem [110] whose properties are well-studied. The modes are orthogonal and the pressure function can be written as their sum

$$y(r,z)=\sum_{m=1}^{\infty}Q_m(r)G_m(z). \tag{4.28}$$

The modal equation, for this sum of the modes, can be written as

$$\sum_{m=1}^{\infty}\left\{\frac{1}{r}\frac{d}{dr}\left(r\frac{dQ_m(r)}{dr}\right)G_m(z)+k_r^2(m,\omega)Q_m(r)G_m(z)\right\}=-\frac{\delta(r)\delta(z-z_t)}{2\pi r}. \tag{4.29}$$

By multiplying this equation with $G_n(z)$ and using the property that the modes are normal for the considered interval of z, the following equation is obtained

$$\frac{1}{r}\frac{d}{dr}\left(r\frac{dQ_n(r)}{dr}\right)+k_r^2(n,\omega)Q_n(r)=-\frac{\delta(r)G_n(z_t)}{2\pi r}. \tag{4.30}$$

Its solution is given by the Hankel function

$$Q_n(r)=\frac{j}{4\rho(z_t)}G_n(z_t)H_0^{(1,2)}(k_r(n,\omega)r). \tag{4.31}$$

Ignoring the time dependence for now, we can conclude that

$$y(r,z)=\frac{j}{4\rho(z_t)}\sum_{m=1}^{\infty}G_m(z_t)G_m(z)H_0^{(1)}(k_r(m,\omega)r). \tag{4.32}$$

By approximating the Hankel function, the final value for pressure will be

$$y(r,z) \approx \frac{j}{4\rho(z_t)\sqrt{8\pi r}} e^{-j\pi/4} \sum_{m=1}^{\infty} G_m(z_t) G_m(z) \frac{e^{jk_r(m,\omega)r}}{\sqrt{k_r(m,\omega)}}. \tag{4.33}$$

In terms of signal processing [105, 106], considering the time dependence of the solution, with a source pressure field $x(t)$, the normal-mode solution to the Helmholtz equation in Eq. (4.23) can be rewritten for the pressure release as

$$\nabla\left(\frac{1}{\rho(z)}\nabla y(r,z,t)\right) - \frac{1}{\rho(z)c^2(z)}\frac{\partial^2 y(r,z,t)}{\partial t^2} = -x(t)\frac{\delta(r)\delta(z-z_t)}{2\pi r}. \tag{4.34}$$

When the range and the depth parameters are known, the acoustic pressure of the received signal can be reduced to $y(t)$. Following the approximation of the Hankel function to the received pressure in Eq. (4.33), the corresponding FT is

$$Y(\omega) = X(\omega)\frac{C}{\rho(z_t)} \sum_{m=1}^{\infty} C_m(\omega) \frac{e^{jk_r(m,\omega)r}}{\sqrt{k_r(m,\omega)r}}. \tag{4.35}$$

where the constant C is

$$C = \frac{j}{4\sqrt{8\pi r}} e^{-j\pi/4} \tag{4.36}$$

and the frequency-dependent shape function $C_m(\omega)$ is

$$C_m(\omega) = G_m(z_t) G_m(z). \tag{4.37}$$

since $G_m(z_t), G_m(z)$ are dependent on ω. In the isovelocity case, the general solution is

$$G_m(z) = A\sin(k_z z) + B\cos(k_z z), \tag{4.38}$$

where

$$k_z = \sqrt{\left(\frac{\omega}{c}\right)^2 - k_r^2}, \tag{4.39}$$

is the vertical wavenumber. The aim of this thesis is to introduce a novel approach of decomposition, reconstruction and analysis of the modes using techniques of compressive sensing, described in Chapter 2.

4.2 Problem formulation - signal processing approach

For the practical setup, it is assumed that the transmitter is placed in water at the depth z_t. This wave is assumed to be transmitted through an isovelocity channel as in [94,95,97,101–103]. The setup is presented in Fig. 4.3. The receiver is places at z_r meters in water. The value r presents the distance from the transmitter to the receiver. Considering the received spectrum Eq. (4.35), the transfer function of the channel in the normal-mode case is

$$H(\omega) = \sum_{m=1}^{+\infty} G_m(z_t) G_m(z_r) \frac{\exp(jk_r(m,\omega)r)}{\sqrt{k_r(m,\omega)r}} = \sum_{m=1}^{+\infty} A_t(m,\omega)\exp\big(jk_r(m,\omega)r\big), \tag{4.40}$$

where $G_m(z_t)$ is the transmitter modal function of the m-th mode and $G_m(z_r)$ is the modal function of the m-th mode corresponding to the receiver [95,105,111]. The rate of attenuation is $A_t(m,\omega) = A(m,\omega)/\sqrt{r}$. The multi-component structure of the transfer function depends on the number of modes. Note that the dispersive characteristic of the signal depends on the wavenumbers $k_r(m,\omega)$ $k_r(m,\omega)$ [95]

$$k_r^2(m,\omega) = \left(\frac{\omega}{c}\right)^2 - \left((m-0.5)\frac{\pi}{D}\right)^2. \tag{4.41}$$

The speed of sound in underwater communications is $c = 1500$ m/s. The response to a monochromatic signal,

$$s(n) = \exp(j\omega_0 n) \tag{4.42}$$

at the m-th mode, is

$$s_m(n) \approx A_t(m,\omega_0)\exp(j\omega_0 n - jk_r(m,\omega_0)r). \tag{4.43}$$

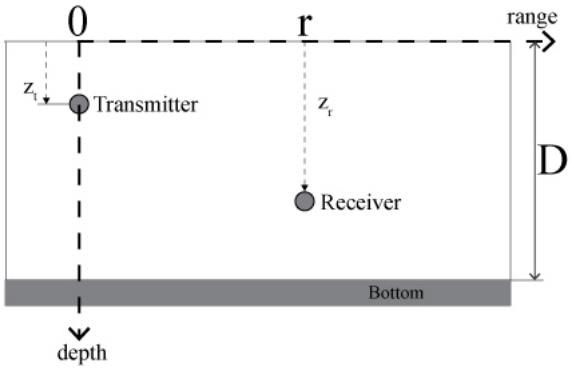

Figure 4.3: The isovelocity setup under water with depth D. The transmitter is located at position z_t, the receiver is positioned at z_r, with the transmitter-receiver range r [95].

The phase velocity of this signal is

$$\nu_m = \frac{\omega}{k_r(m,\omega)} = \frac{\omega}{\sqrt{\left(\frac{\omega}{c}\right)^2 - \left((m-0.5)\frac{\pi}{D}\right)^2}}, \tag{4.44}$$

and presents the horizontal velocity of the corresponding phase in the representation of the m-th mode.

The group velocity represents the energy propagation of the component of the signal. Considering the time dependence of the signal,

$$y(t) = \int_{\omega-\epsilon}^{\omega+\epsilon} Y(\omega)e^{-j[\omega t - k_r(m,\omega)r]}d\omega, \tag{4.45}$$

and the fact that the phase must stay the same in order to have the signal remain unchanged through the whole time interval, the group velocity is defined as

$$u_m = \frac{dr}{dt} = \frac{d\omega}{dk_r(m,\omega)} = \frac{1}{\frac{dk_r(m,\omega)}{d\omega}} = \frac{1}{\frac{d}{d\omega}\sqrt{\left(\frac{\omega}{c}\right)^2 - \left((m-0.5)\frac{\pi}{D}\right)^2}}. \tag{4.46}$$

Since the received signal can be written in the Fourier transform domain as

$$X(\omega) = S(\omega)H(\omega), \tag{4.47}$$

where $H(\omega)$ is the transfer function of the channel in the normal-mode form and $S(\omega)$ is the transmitted signal Fourier transform, within signal processing framework the time-domain form of the received signal is then equal to the convolution of the transmitted signal and the impulse response of (4.40), that is

$$x(n) = s(n) * h(n), \tag{4.48}$$

where $h(n)$ is the impulse response of (4.40).

Amplitude of the first four modes of the impulse response of a dispersive channel environment and its ideal time-frequency representation is calculated and shown in Fig. 4.4. Our first goal is to present efficient tools for decomposition of mode functions. This will help to easier detect and estimate the signal parameters. The detection approaches related to this kind of problems will be introduced in the next sections.

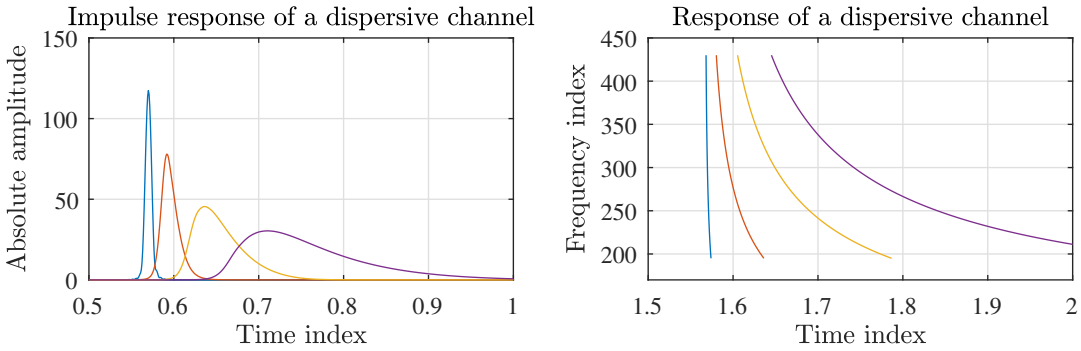

Figure 4.4: The ideal response of the four considered modes.

4.3 Polynomial Fourier transform (PFT)

The standard Fourier transform is spread in the frequency domain for the signal with polynomial phase function. The idea behind the polynomial Fourier transform (PFT) is to introduce a polynomial function in the Fourier transform whose adjustment would improve a polynomial phase signal concentration in the frequency domain.

Let assume a polynomial phase signal (PPS). The signal is of order P, presented in the form of

$$x(n) = Ae^{j\frac{2\pi}{N}\sum_{l=1}^{P} a_l n^l}. \tag{4.49}$$

The standard Fourier transform of $x(n)$ is

$$X(k) = \sum_n x(n)e^{-j\frac{2\pi}{N}kn}, \tag{4.50}$$

would contain all frequencies defined by the instantaneous frequency variations of the polynomial phase signal.

Definition 4.1
The PFT is defined starting from DFT and introducing an additional polynomial phase parameters [112–114]

$$X_{\alpha_2,\alpha_3,...,\alpha_P}(k) = \sum_n x(n)e^{-j\frac{2\pi}{N}(\alpha_2 n^2+\alpha_3 n^3+...+\alpha_P n^N)}e^{-j\frac{2\pi}{N}kn}. \tag{4.51}$$

The PFT parameters are denoted by $\alpha_2, \alpha_3, ..., \alpha_P$.

The aim is to estimate the parameters $\alpha_2, \alpha_3, ..., \alpha_P$ when the transformation of the signal is largely concentrated. The signal components can be extracted and localized following this procedure [7, 85].

When the largest component of the transform is found, the signal will be maximally concentrated in the PFT representation domain. That is, when the PFT signal is best concentrated, we can find optimal PFT parameters as

$$(\hat{a}_2, \hat{a}_3, ..., \hat{a}_P) = \arg \max_{(k,\alpha_2,...,\alpha_P)} |X_{\alpha_2,...,\alpha_P}(k)|. \tag{4.52}$$

to achieve the maximum sparsity. In the ideal scenario, the PFT of $x(n)$ will have the highest concentration when $(\alpha_2, ..., \alpha_P) = (a_2, ..., a_P)$. In reality, the goal is to calculate the values to be as close as possible to the ideal parameters, i.e., $a_2 \approx \hat{a}_2$, ..., $a_P \approx \hat{a}_P$.

4.3.1 Local polynomial Fourier transform (LPFT)

For time-varying signals, when the parameters may change in time, a localized versions of the PFT is introduced in the same way as the STFT is defined by using the Fourier transform. Spectral localization of the signal is achieved applying a window and calculating the PFT of the windowed signal to get the local PFT (LPFT).

Definition 4.2
The LPFT is defined as [7, 115]

$$X_{\alpha_2,\alpha_3,...,\alpha_P}(k,n) = \sum_m x(n+m)w(n_w)e^{-j\frac{2\pi}{N}(kn_w+\alpha_2 n_w^2+...+\alpha_P n_w^N)}. \tag{4.53}$$

where $w(n_w)$ is the window function for the localized signal analysis.

In the same way as for the PFT, the maximum of LPFT is achieved when

$$(\hat{a}_2, \hat{a}_3, ..., \hat{a}_P) = \arg \max_{(k,\alpha_2,...,\alpha_P)} |X_{\alpha_2,...,\alpha_P}(k, n)|, \tag{4.54}$$

where $\alpha_2, \alpha_3, ..., \alpha_P$ are the parameters that can now be adapted for each considered instant n. However, in order to simplify the notation we will not use argument n in the parameters in this case.

4.4 Dual form of PFT (DPFT)

The dual form of PFT (DPFT) is introduced as a more suitable representation for the decomposition of signals when their spectral content is localized within a short time-interval, while the changes of their spectral content are significant. As it is the case for both PFT and LPFT, the idea is to estimate the parameters where the maximal concentration of the DPFT is calculated.

The signal model is a polynomial-phase in the frequency domain,

$$X(k) = Ae^{-j\frac{2\pi}{N}\sum_{l=1}^{P} b_l k^l}. \tag{4.55}$$

The discrete DPFT will then be

$$x_{\beta_2,\beta_3...,\beta_P}(n) = \sum_k X(k) e^{j\frac{2\pi}{N}(nk+\beta_2 k^2+...+\beta_P k^P)}. \tag{4.56}$$

The maximum of DPFT is achieved when

$$(\hat{b}_1, \hat{b}_2, ..., \hat{b}_P) = \arg \max_{(n,\beta_2,...,\beta_P)} |x_{\beta_2,...,\beta_P}(n)|. \tag{4.57}$$

The highest concentration is calculated when the estimated values are equal to the true ones, i.e., $(\beta_2, ..., \beta_P) = (b_2, ..., b_P)$. For a successful decomposition, the parameters should be estimated such that $\hat{b}_2 \approx b_2, \ldots, \hat{b}_P \approx b_P$.

Note that a local version of the DPFT may be used for the analysis of more complex time-varying signals. The local DPFT uses a window in the frequency domain $W(k)$ and it is defined as

$$x_{\beta_2,\beta_3...,\beta_P}(n, k) = \sum_l W(l) X(k+l) e^{j\frac{2\pi}{N}(nl+\beta_2 l^2+...+\beta_P l^P)}. \tag{4.58}$$

4.4.1 Sparsity in DPFT

Signals with a small number of polynomial phase components, considered in the previous section, may be considered as sparse in the DPFT. These signals can be efficiently decomposed and analyzed using the compressive sensing methods. Note that the CS approach can be

applied even in the cases when not all signal samples in the Fourier transform are available, allowing application in denoising of acoustic signals corrupted with high sinusoidal interferences (clutter). These frequency samples are removed, declared as unavailable, and the signal is reconstructed using the undisturbed frequency values, as it will be shown in the examples.

Consider that the Fourier transform of a signal $\mathbf{X}$ has a reduced number of available samples, for example, due to denoising procedure on harmonic disturbances. Let consider the PPS from (4.55)

$$X(k) = Ae^{-j\frac{2\pi}{N}\sum_{l=1}^{P} b_l k^l} = Ae^{-j\frac{2\pi}{N}(b_1 k + b_2 k^2 + \cdots + b_P k^P)} \tag{4.59}$$

and its samples at $k \in \{k_1, k_2, \ldots, k_{N_A}\} = \mathbb{N}_{\mathbb{A}}$. The initial estimate of the P-order DPFT of a signal whose Fourier transform is $X(k)$, using a reduced set of its samples, is

$$x_{\beta_2,\ldots,\beta_P}(n) = \sum_{k\in\mathbb{N}_{\mathbb{A}}} X(k)e^{j\frac{2\pi}{N}(nk+\beta_2 k^2+\cdots+\beta_P k^P)} \tag{4.60}$$

Assume that the parameters $\beta_2, \beta_3, \ldots, \beta_P$ are correctly estimated, so that the DPFT achieves the maximum concentration. The DPFT of a single-component signal is then

$$x_{b_2,\ldots,b_P}(n) = \sum_{k} Ae^{j\frac{2\pi}{N}k(n-b_1)} = A\delta(n-b_1). \tag{4.61}$$

Having only one component, with the rest of the spectrum being zero-valued, we can conclude that it is sparse. In the multicomponent signals case

$$X(k) = \sum_{m=1}^{M} A_m e^{-j(b_{1m}k+b_{2m}k^2+\cdots+b_{Pm}k^P)}, \tag{4.62}$$

set of parameters is iteratively estimated separately for each component individually. Without loss of generality, we consider that the component amplitudes are decreasing, i.e. $A_1 > A_2 > \cdots > A_M$. The first component is matched with

$$(\beta_{21}, \ldots, \beta_{P1}) = (b_{21}, \ldots, b_{P1}). \tag{4.63}$$

After the first match, other components are considered as insignificant. The measurements matrix is found from (4.60) assuming only the available samples at $k \in \mathbb{N}_{\mathbb{A}}$. The relation for various values of n is

$$\begin{bmatrix} x_{b_{21},\ldots,b_{P1}}(n_1) \\ x_{b_{22},\ldots,b_{P2}}(n_2) \\ \vdots \\ x_{b_{2K},\ldots,b_{PK}}(n_K) \end{bmatrix} = \mathbf{A}_K^H \begin{bmatrix} X(k_1) \\ X(k_2) \\ \vdots \\ X(k_{N_A}) \end{bmatrix} \tag{4.64}$$

where the matix $\mathbf{A}_K$ is defined by

$$\mathbf{A}_K = \begin{bmatrix} e^{-j\frac{2\pi}{N}(n_1k_1+\phi_1)} & \ldots & e^{-j\frac{2\pi}{N}(n_Kk_1+\phi_1)} \\ \vdots & \ddots & \vdots \\ e^{-j\frac{2\pi}{N}(n_1k_{N_A}+\phi_{N_A})} & \ldots & e^{-j\frac{2\pi}{N}(n_Kk_{N_A}+\phi_{N_A})} \end{bmatrix} \tag{4.65}$$

with

$$\phi_i = k_i^2 b_{21} + \cdots + k_i^P b_{P1} \tag{4.66}$$

for $i = 1, \ldots, N_A$. Using the available coefficients of $X(k)$, $k \in \mathbb{N}_{\mathbb{A}}$, the nonzero values in time $[x_{b_{21},\ldots,b_{P1}}(n_1), x_{b_{22},\ldots,b_{P2}}(n_2), \ldots, x_{b_{2K},\ldots,b_{PK}}(n_K)]$ are reconstructed using the CS algorithm from Section 1.3.1. The first component is calculated as

$$\mathbf{x}_1 = (\mathbf{A}_1^H \mathbf{A}_1)^{-1} \mathbf{A}_1^H \mathbf{y}. \tag{4.67}$$

When the first DPFT component at n_1 is recovered, the remaining coefficients of $X(k)$ are estimated for the first element. Then, the first component is deleted from the set of available measurements and the algorithm is repeated for the next coefficient. After its parameters are found and denoted by $(\beta_{22}, \ldots, \beta_{P2}) = (b_{22}, \ldots, b_{P2})$, both the first and second component are reconstructed simultaneously. The components are reconstructed using

$$(\beta_{21}, \ldots, \beta_{P1}) = (b_{21}, \ldots, b_{P1}), \text{ and } (\beta_{22}, \ldots \beta_{P2}) = (b_{22}, \ldots, b_{P2}) \tag{4.68}$$

and the components are removed for the further estimation of the remaining components. The procedure is repeated for all n_i. Note that, if the DPFT values are off-grid, we may use few samples around the position n_i for a more accurate reconstruction. The stopping criterion of the reconstruction is defined by the desired error rate.

The results of the decomposition are single components of a non-stationary signal. The analysis of the signal will be done in the frequency domain, using the dual version of the STFT, since all examined modes are spread over a broad spectrum of frequencies. The dual STFT is defined by

$$STFT_D(k,n) = \sum_{p=-N_s/2}^{N_s/2-1} X(p-k) W(p) e^{j\frac{2\pi}{N_s}pn}. \tag{4.69}$$

where N_s is the length of the window in the frequency domain.

Following the form of the S-method (1.19), the dual S-method is then

$$SM_D(k,n) = \sum_{i=-L}^{L} STFT_D(k,n+i) STFT_D^*(k,n-i). \tag{4.70}$$

4.4.2 Results

Three examples, showing the efectivness of the proposed method, are presented. The algorithm used for the reconstruction is the OMP algorithm explained in Section 2.1.

Example 1: Ideal polynomial phase signal with sinusoidal disturbances.

Let consider the case when the polynomial phase structure of signal is fully satisfied (4.55). Assume that the received signal consists of four components (modes).

$$X(k) = X_1(k) + X_2(k) + X_3(k) + X_4(k), \tag{4.71}$$

where

$$X_1(k) = e^{j\frac{2\pi}{N}(150k+0.06k^2)},$$
$$X_2(k) = e^{j\frac{2\pi}{N}(180k+0.015k^2+0.00009k^3)},$$
$$X_3(k) = e^{j\frac{2\pi}{N}(300k+0.00008k^3)},$$
$$X_4(k) = e^{j\frac{2\pi}{N}(480k+0.035k^2+0.0001k^3)}.$$

The frequency index range is $k = 0, \ldots, N-1$ with $N = 1024$. The time domain of the signal is presented in Fig. 4.5 (top left). The corresponding frequency domain of the signal (4.71), is shown in Fig. 4.5 (top right). Assume that $N_Q = 256$ of samples in the frequency domain are corrupted by strong sinusoids, resulting in the signal

$$x_d(n) = x(n) + \sum_{l=1}^{N_Q} B_i e^{j(\omega_l n+\psi_l)}. \tag{4.72}$$

Time and frequency domains of the corrupted signal are illustrated in Fig. 4.5 (middle). The first goal is to detect and remove the strong periodic disturbances from the signal. In order to filter the signal, a simple notch filter is used to set to zero the disturbed components (i.e., hard thresholding). The filtered signal, in time and frequency domain, is illustrated in Fig. 4.5 (bottom).

The decomposition is performed using the DPFT according to the definition (4.60), assuming the third-order DPFT. The parameter β_2 is varied between -0.2 to 0.2 and β_3 between -0.3 to 0.3. The parameter values where the DPFT gives the best concentration for each mode are detected in an iterative way. When the first set of parameters β_2, β_3 is found, the peak in the DPFT corresponds to a single component with these parameters. The component can be dismissed from the DPFT and the estimation of the remaining components is continued. The DPFT decomposition of the four modes is shown in Fig. 4.6, with the estimated β_2, β_3 presented in Table 4.1.

Table 4.1: Parameters β_2, β_3 for each mode corresponding to the DPFT where the maximal concentration is achieved in the ideal case.

Parameters/Mode	**1**	**2**	**3**	**4**
β_2	0.1232	0.1888	0.0600	0.1536
β_3	0.0132	0.0168	0.0000	0.0144

For the TF representation, we have used the S-method with $L = 31$ and Hanning window of length $N_w = 256$. The S-method of the received signal is showin in Fig. 4.7 (top left). The decomposition of the four reconstructed components in the S-method represantion is presented the next four subplots of Fig. 4.7. The sum of the normalized representations of the four modes is presented in Fig. 4.7 (bottom right). For the comparison, the original (without noise) and the reconstructed signal in time-domain are shown in Fig. 4.8.

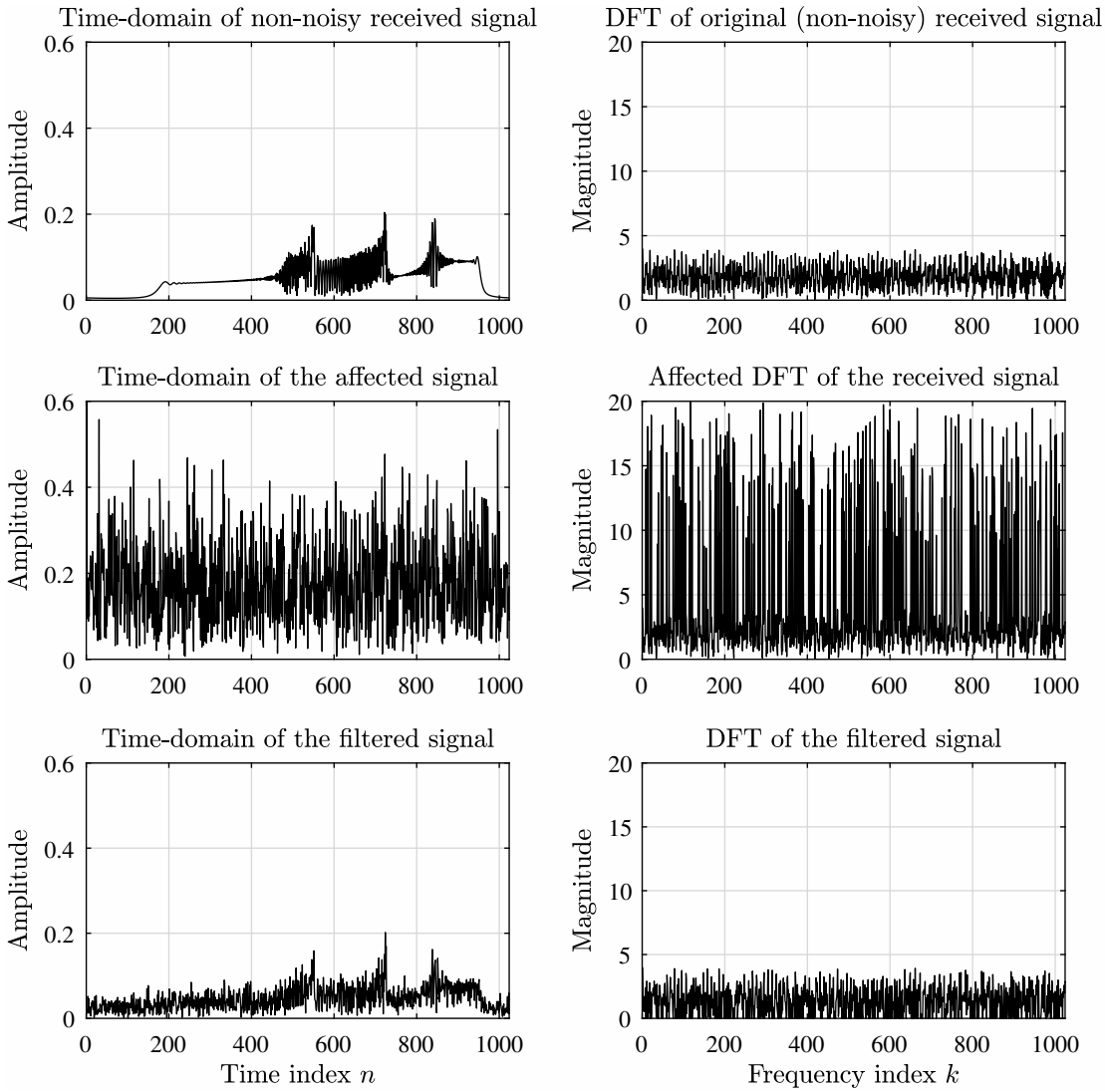

Figure 4.5: Ideal case scenario: Time domain received signal (left); received signal in the frequency domain (right): the recieved signal without disturbance (top), the recieved signal with disturbance (middle), the signal with filtered disturbances (bottom).

Example 2: Decomposition of a simulated acoustic signal.

The acoustic signal, interpreted in Section 4.2. will be used for the decomposition. Note that this signal is not characterized by the ideal polynomial phase structure, but rather it can be approximated by a polynomial phase signal.

A simple one-component LFM as in (4.42) is transmitted over a dispersive media. The dispersive channel consists of $M = 4$ modes. The received signal is of form (4.48). It depends on (4.40) and (4.41). The amplitude attenuates by $A_m = (6 - m)W(f)$, where $W(f)$ is the frequency response of the Hanning window of length $N_w = 256$. The depth of the dispersive channel is assumed to be $D = 20$ meters. The distance between the transmitter and receiver

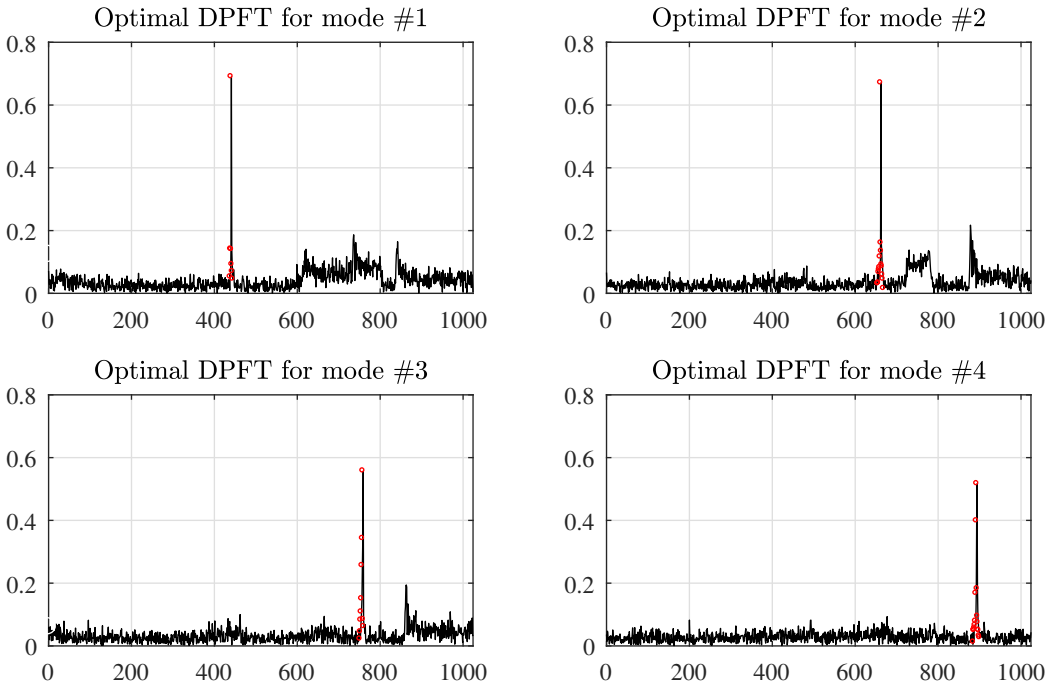

Figure 4.6: Decomposition of the components using DPFT in the ideal case.

is $r = 2350$ meters. The frequency range is $f_{min} = 195$ Hz and $f_{max} = 430$ Hz. The received signal is presented in Fig. 4.9 (top left).

The DPFT of the third order is used for the analysis, and the parameters β_2, β_3 are varied between -0.2 to 0.2 and -0.3 to 0.3, respectively. The estimated parameters are presented in the Table 4.2. The DPFT mode decomposition is illustrated in Fig. 4.9.

Table 4.2: Parameters corresponding to the maximal DPFT values for each mode in the simulated acoustic case without disturbances.

Parameters/Mode	**1**	**2**	**3**	**4**
β_2	-0.0380	-0.0400	0.1780	0.1240
β_3	-0.0180	-0.0420	-0.1530	-0.2340

The Hanning window of size $N_w = 512$ is used for the dual STFT, while for the dual S-method $L = 63$ is used. The S-method of the received modes is shown in Fig. 4.10 (top left). The sum of the four normalized component representations is presented in Fig. 4.10 (bottom right). The S-method decomposition of the four modes, obtained by the DPFT before the CS theory, is presented in the remaining subplots of Fig. 4.10.

Example 3: Acoustic signal with strong disturbances.

Assume the signal Example 2, affected by high sinusoidal interferences according to (4.72).

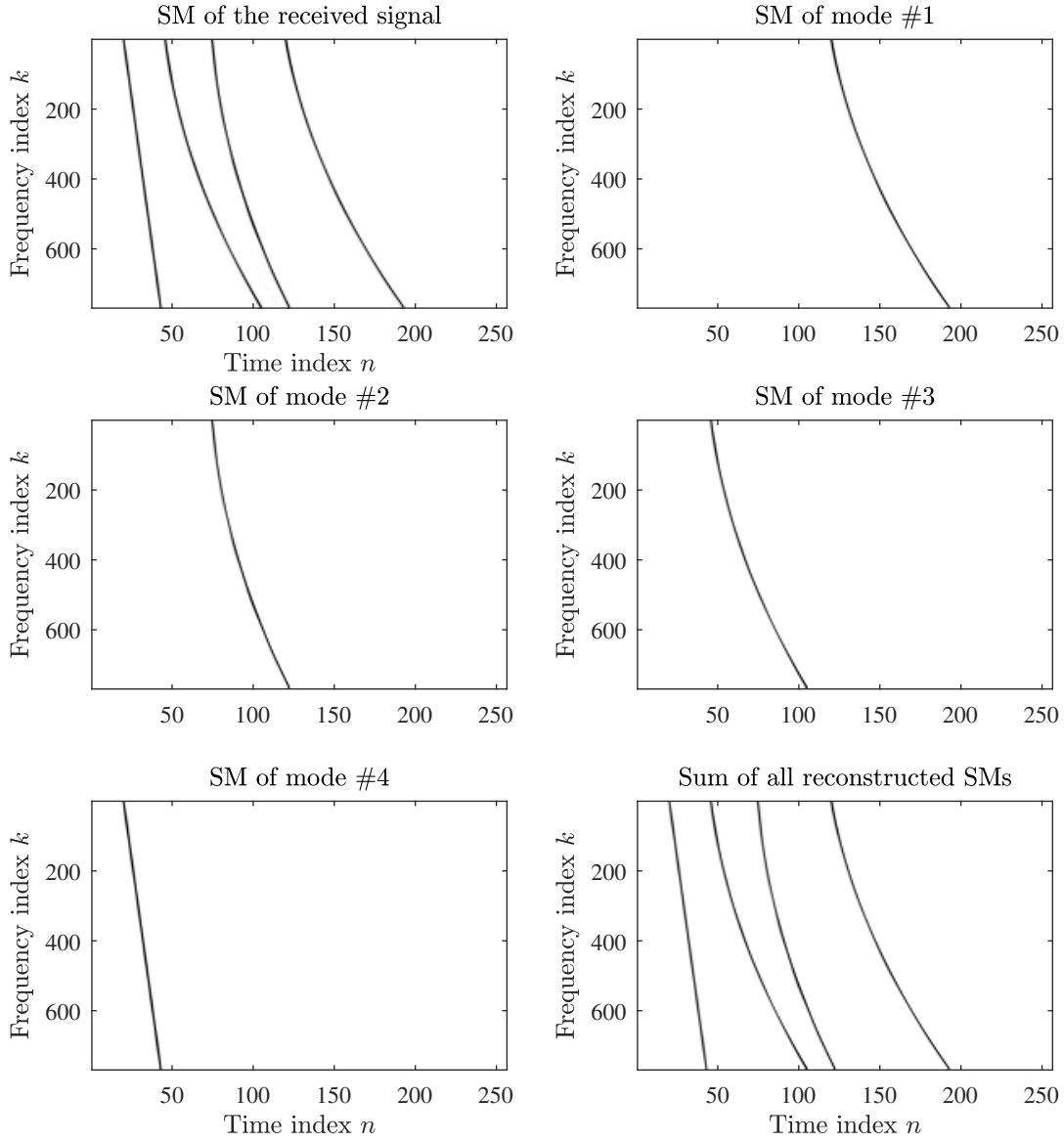

Figure 4.7: S-method decomposition of the components in the ideal case.

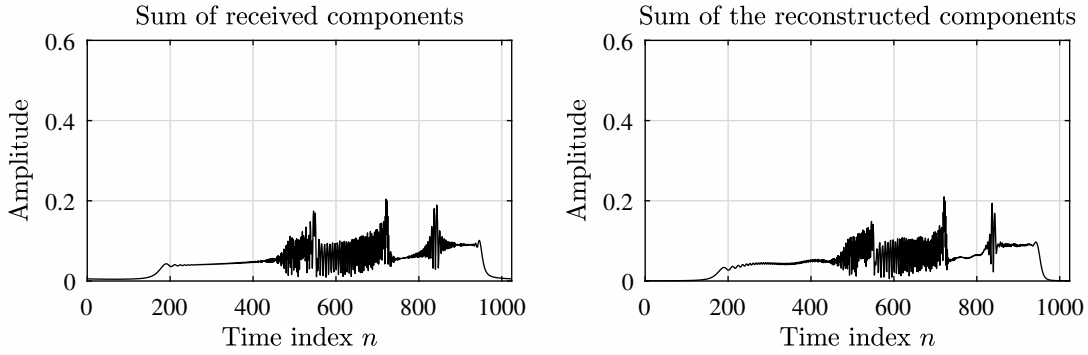

Figure 4.8: Comparison of the signals in the ideal case: The original signal (left); the reconstructed signal (right).

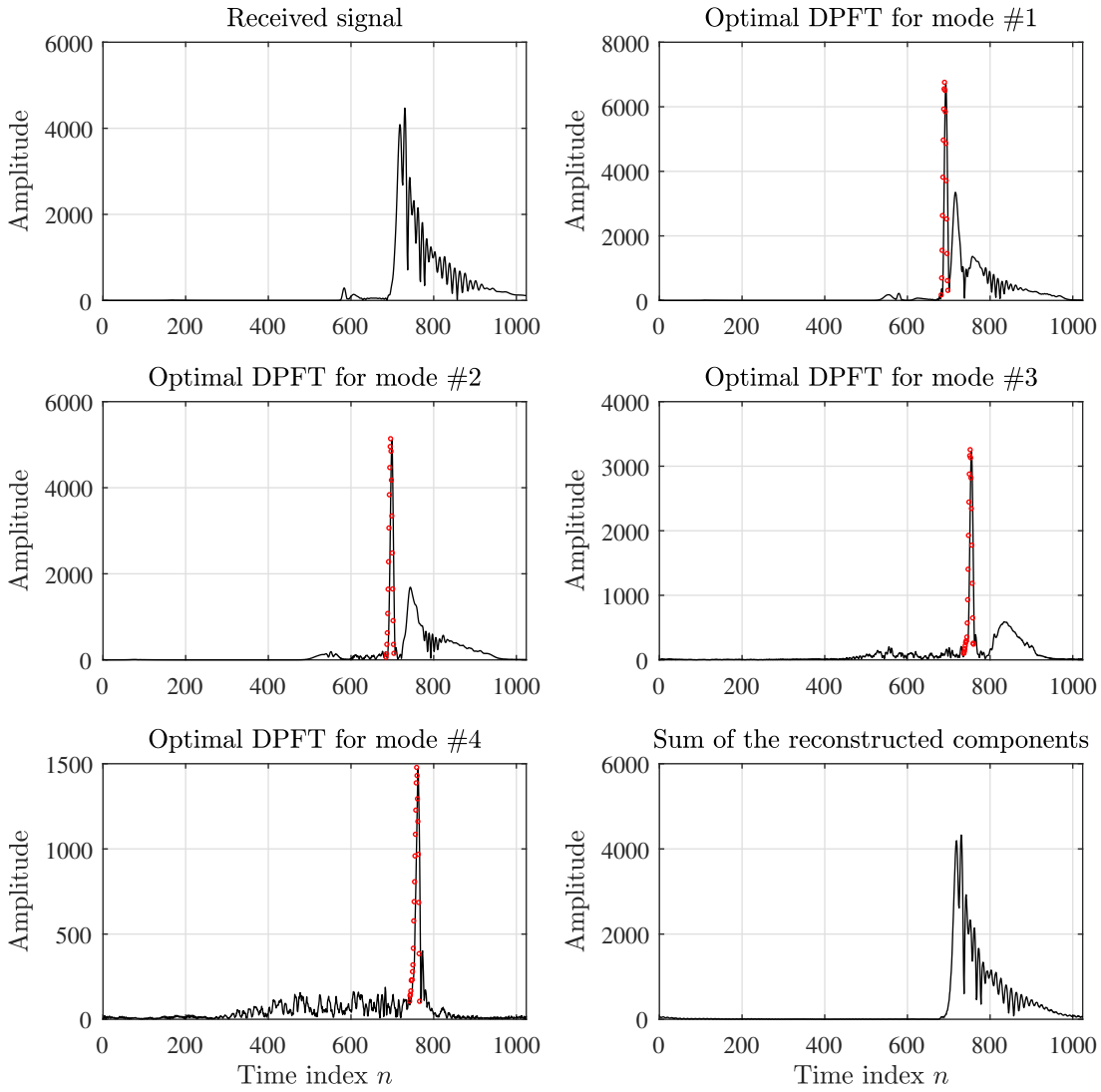

Figure 4.9: Time-domain mode decomposition: Received signal (top left); Sum of the reconstructed modes (bottom right); Optimal DPFT estimation for each mode separately (remaining subplots). Red circles - samples related to the corresponding mode.

Assume the case same as in previous example, with $A_m = 1$. The received signal without intereferences is illustrated in Fig. 4.11 (top). It is assumed that the received signal has high-impulse intereferences in the frequency domain in 25% of the spectrum. The corrupted received signal is shown in Fig. 4.11 (middle).

As in Example 1, the affected components are removed using hard thresholding, and the corrupted spectral sampled are considered as not available. Time and frequency domains of the filtered received signal are presented in Fig. 4.11 (bottom).

After filtering, the estimation of the parameters is achieved using a third-order DPFT, illustrated in Fig. 4.12. The parameters β_2 and β_3 are varied within the range -0.7 to 0.7.

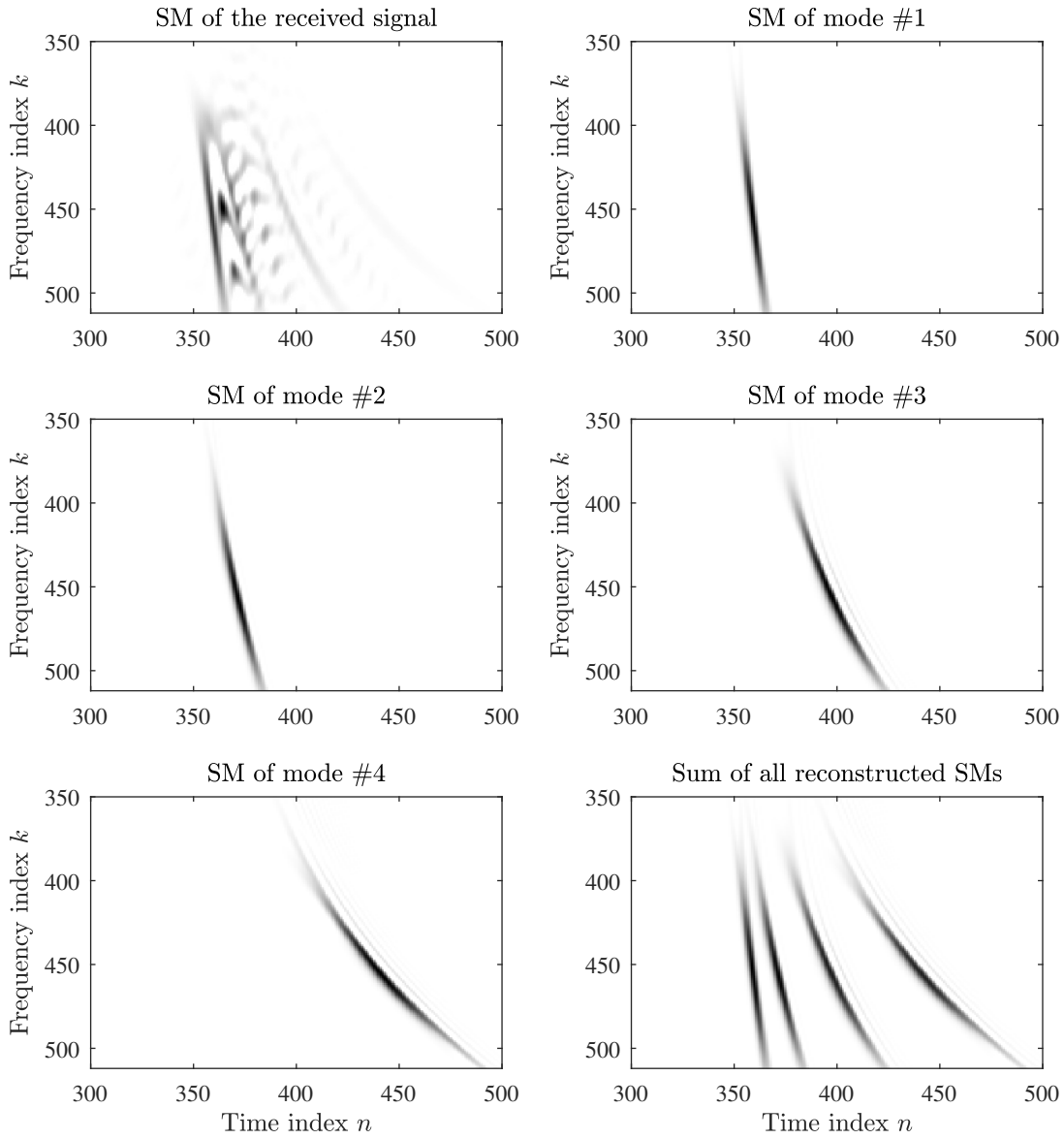

Figure 4.10: S-method of the decomposed modes and sum of the normalized representations of all modes in the simulated acoustic case without disturbances

The estimated DPFT parameters β_2, β_3 can be found in Table 4.3.

The S-method of whole signal and individual modes given in Fig. 4.13. The comparison between the received signal, when no noise is present, and the final reconstructed signal are presented in Fig. 4.14.

It can be concluded that it is possible to decompose and recover original values of the acoustic samples using the CS techniques for reconstruction of reduced set of samples in the frequency domain. It is seen that the obtained results are similar to the results obtained in Example 2, i.e., when the signal without intereferences is examined.

Table 4.3: Parameters corresponding to the maximal DPFT values for each mode in the acoustic simulated case with disturbances.

Parameters/Mode	**1**	**2**	**3**	**4**
β_2	0.2576	0.3556	0.5712	0.1288
β_3	-0.1764	-0.1232	-0.3584	-0.0812

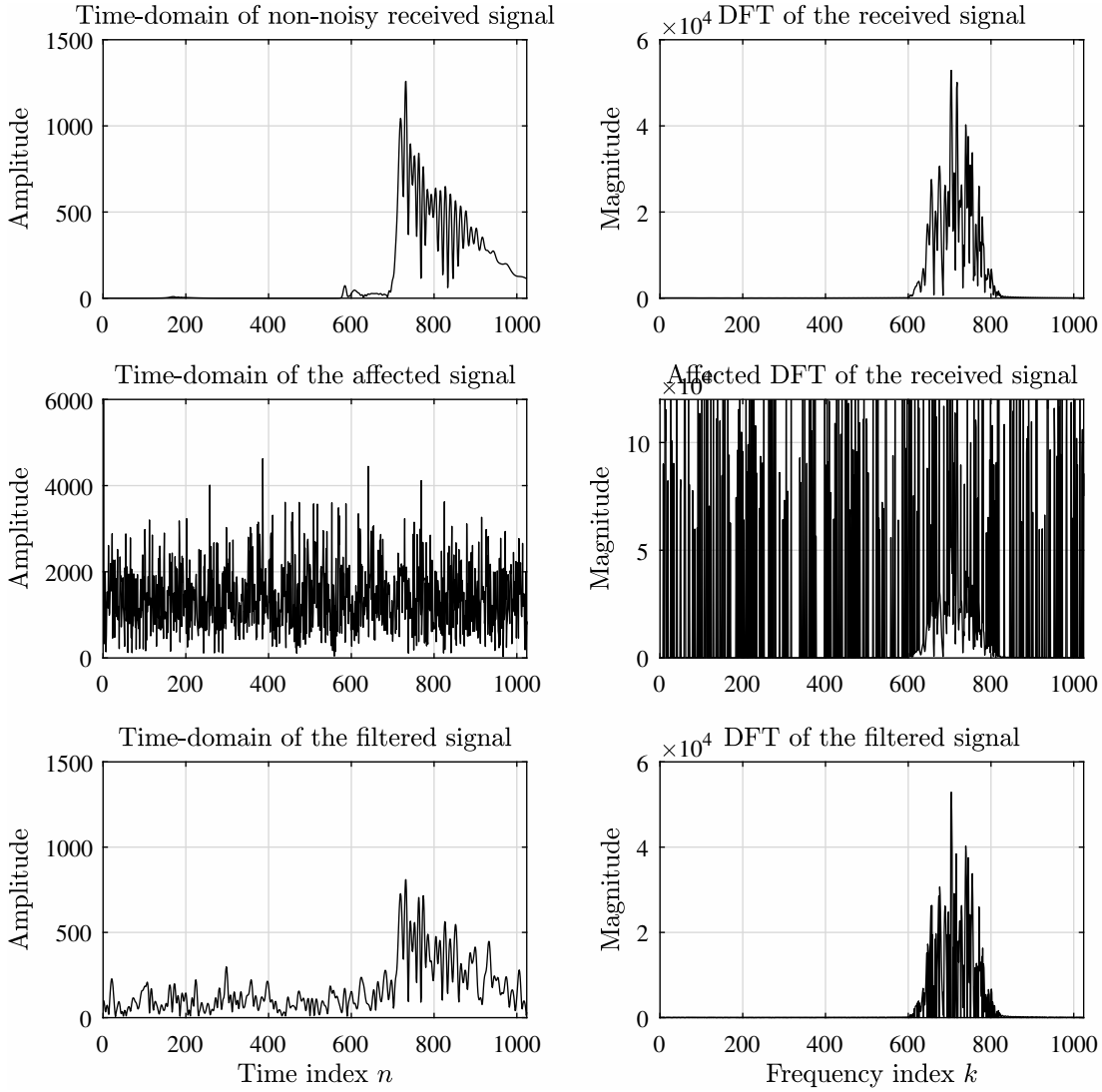

Figure 4.11: Simulated acoustic signal with disturbances: Signals in the time domain (left); Signals in the frequency domain (right): Received signal without disturbances (top), received signal with disturbances (middle), filtered received signal (bottom).

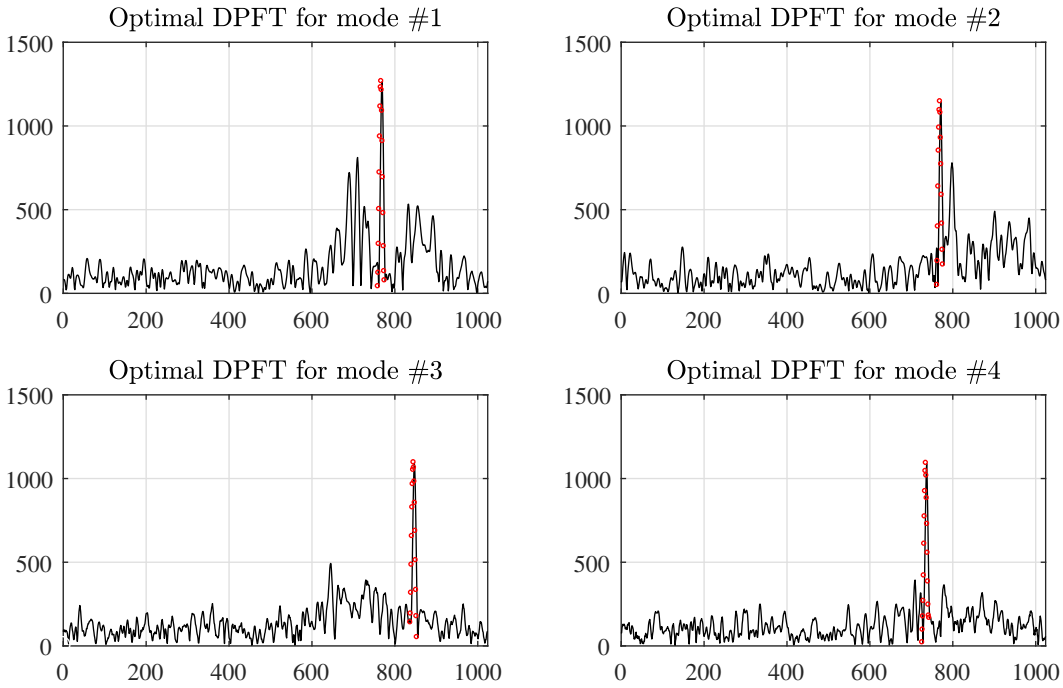

Figure 4.12: Decomposition of the components using DPFT in the acoustic simulated case with disturbances.

4.5 Model-based decomposition

In the previous section, the decomposition of the signal is performed by varying DPFT parameters. In this section, we will use the idea to vary the parameters of the modal functions as the decomposition functions instead of the polynomial phase model of the signal. Since the components take the form of modal functions in the considered acoustic signal propagation case, we take the channel depth D_m and the range r as the parameters that are being estimated, instead of the polynomial coefficients $\beta_{2,3}$. The goal is to vary the parameters of the transfer function model in the way we would vary the frequency parameters in the DPFT. Taking into account the FT of the discrete received signal $X(f)$ and the wavenumbers $k_r(m,f)$ as in Eq. (4.41), instead of the DPFT, given by

$$X(k) = \sum_{m=1}^{M} A_m e^{-j(b_{1m}k + b_{2m}k^2 + b_{3m}k^3)}, \tag{4.73}$$

the received signal will be then decomposed using its normal mode form

$$X(k) = \sum_{m=1}^{K} A(m) e^{jk_r(m,k)r}, \tag{4.74}$$

where

$$k_r(m,k) = \left(\frac{2\pi k}{n\Delta t c}\right)^2 - \left((m-0.5)\pi/D_m\right)^2). \tag{4.75}$$

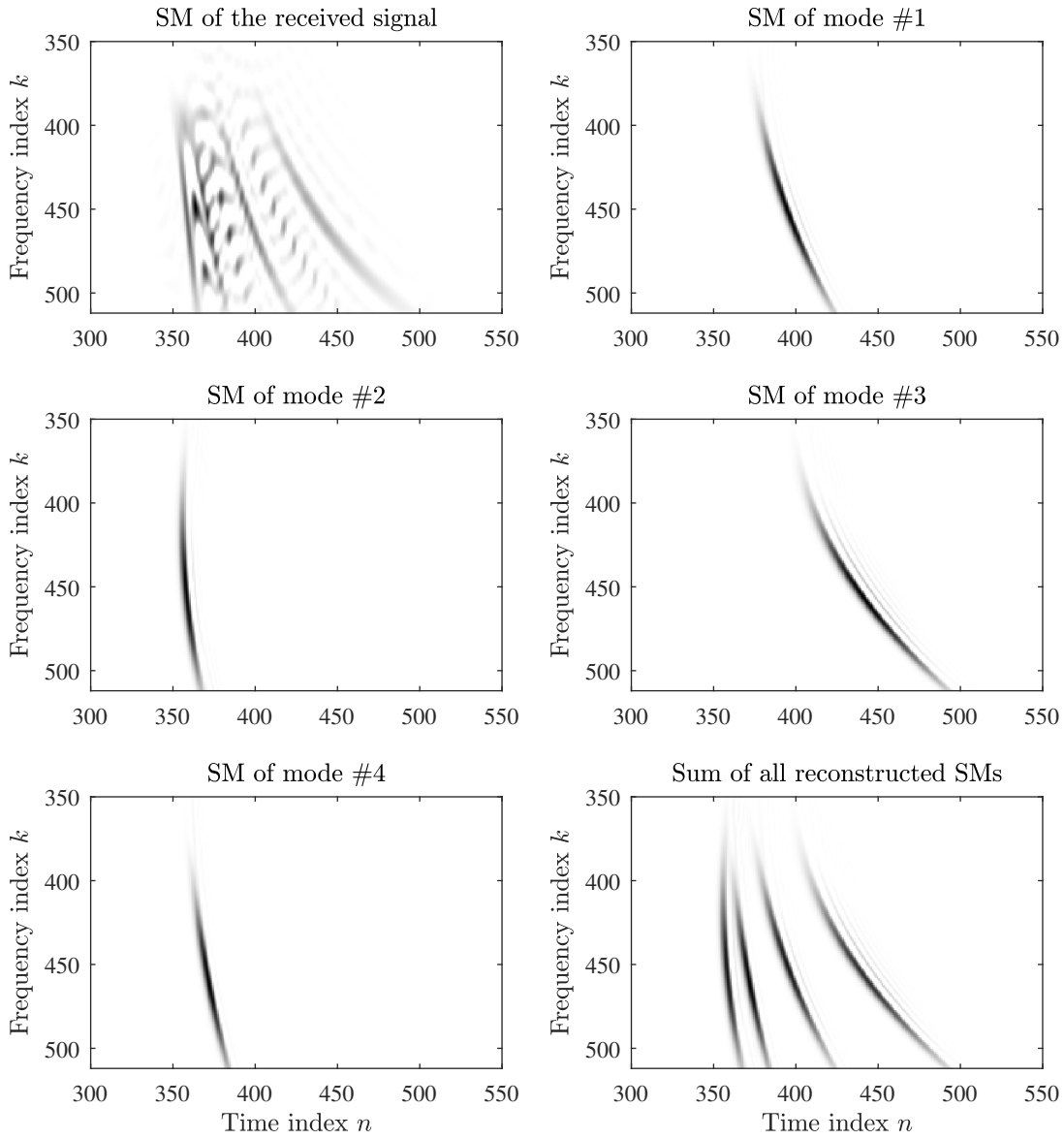

Figure 4.13: S-method decomposition of the components in the acoustic simulated case with disturbances.

The speed and the frequency range in which the underwater acoustic system operates are defined a priori. The values β_2 and β_3 are varied within the expected range in the transform

$$x_{m,\beta_2,\beta_3}(n) = \sum_k X(k) e^{-j\left(\left(\frac{2\pi k}{n\Delta t c}\right)^2 - \left((m-0.5)\pi/\beta_3\right)^2\right)\beta_2} e^{-j2\pi nk/N} \tag{4.76}$$

If the parameters β_2, β_3 are correctly estimated, $\beta_2 = r$ and $\beta_3 = D_m$ then this new representation $x_{\beta_2,\beta_3}(n)$ will achieve maximum concentration. Therefore, the representation

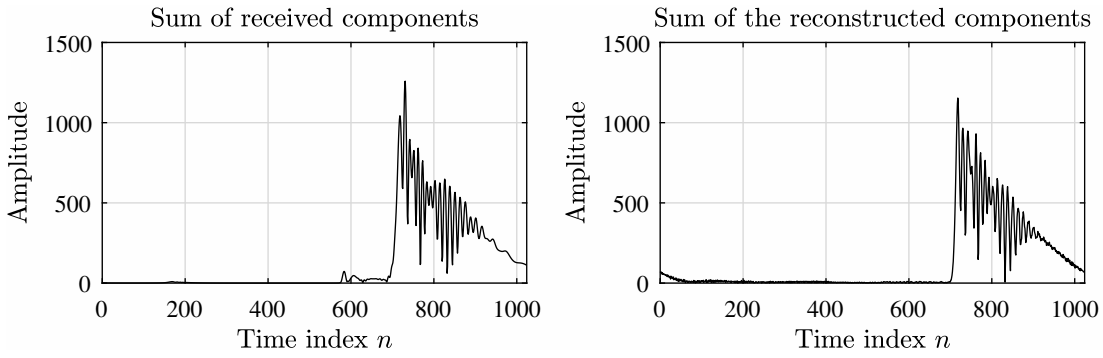

Figure 4.14: Comparison of the signals in the acoustic simulated case with disturbances: The original signal (left) and the reconstructed signal (right).

with the highest concentration produces estimate of the parameters r and D_m

$$(\hat{r}, \hat{D}_m) = \arg \max_{(\beta_2,\beta_3)} |x_{m,\beta_2,\beta_3}(n)| \tag{4.77}$$

when these values are close to the true ones, i.e. $\hat{D}_m \approx D_m$ and $\hat{r} \approx r$. As is in the case of the DPFT, when the strongest component is detected, it is removed and the next mode parameters are detected. This procedure is continued until the remaining components are negligible.

4.5.1 Results

To illustrate the decomposition and reconstruction, let consider the ideal case as from Section 4.2., with the frequency range between $f_{min} = 320$ Hz and $f_{max} = 570$ Hz. The distance between the transmitter and receiver r and the true channel depth D will remain the same. These two parameters are considered as unknown and further estimated.

The transmitted signal is considered to be a pulse with a short interval, close to a delta function, whose spectrum is then equal to 1, i.e. $U(f) = 1$. The received signal is of form Eq. (4.48), which will result in $X(f) = H(f)$.

Variables D and r are arbitrarily varied. The value for depth D is varied in the range between 0 to 100. The distance value r is varied in the range between 1000 to 3000.

It has been calculated that the maximal values are found at the position $D = 20.0357$ m and $r = 2350$ m. The decomposition of each component is shown in Fig. 4.15. The sum of the received coefficients and the sum of reconstructed components are shown in Fig. 4.16.

The decomposition results will be analyzed in the frequency domain using the dual S-method from Eq. (4.70). A Hanning of size $N_w = 63$ is used as the window. The dual S-method representation of a sum of the four received modes is shown Fig. 4.17 (top left). Sum of the decomposed components and the amplitudes of individual components are given

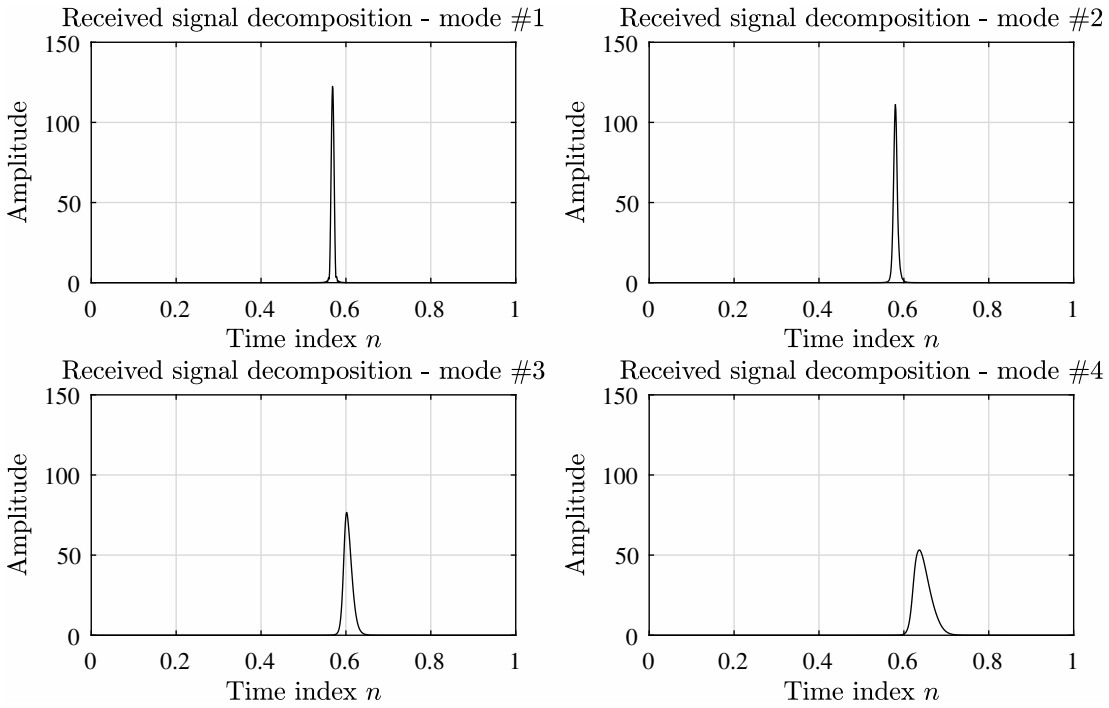

Figure 4.15: Decomposed modes in the time domain using the model-based technique

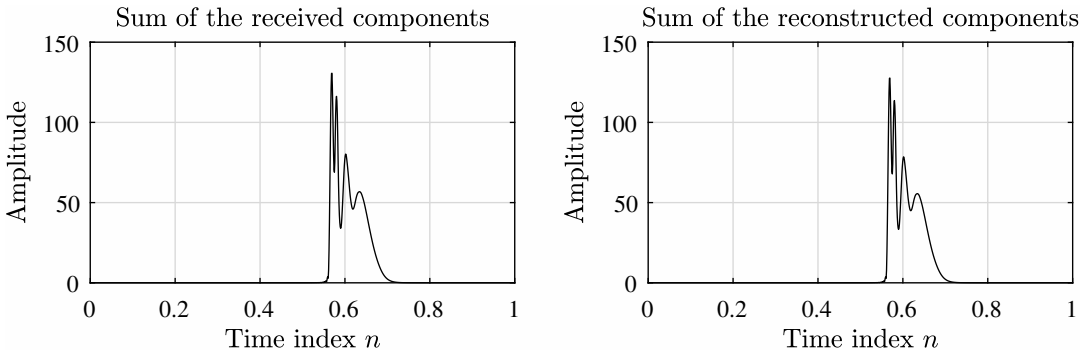

Figure 4.16: Sum of the components: received (left); reconstructed (right)

in Fig. 4.17 (bottom right), with the decomposition of each mode individually in the other four subplots of Fig. 4.17.

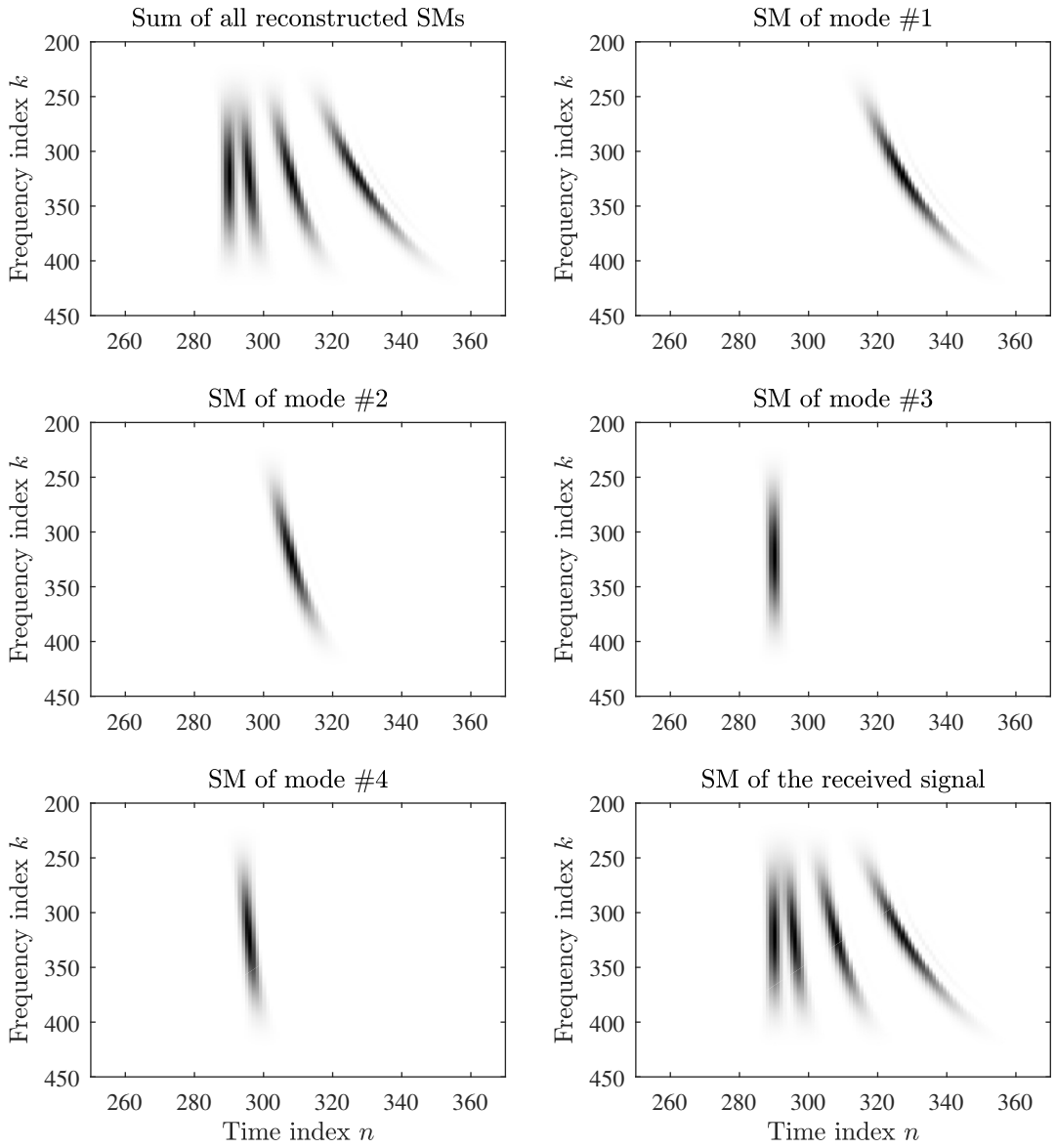

Figure 4.17: S-method decomposition of the components when model-based decomposition is used.

4.6 Comparison

The mean squared error (MSE) in the decomposition is calculated as

$$e = 10 \log \frac{\sum_{k,n} |SM_{DR}(k,n) - \sum_m SM_{Dm}(k,n)|^2}{\sum_{k,n} |SM_{DR}(k,n)|^2} \tag{4.78}$$

where $SM_{DR}(k,n)$ and $SM_{Dm}(k,n)$ are the sum of received dual S-method components and the sum of S-method components of modes of the received signal after the decomposition. The errors in dB are shown in Table 4.4.

Table 4.4: Error in the form of MSE in dB for the examples considered

Case	MSE [dB]
Ideal-case DPFT	-12.6198
Simulated acoustic signal DPFT	-10.1590
Simulated acoustic signal with disturbance DPFT	-7.9361
Model-based technique	-30.5013

The MSE value of the model-based technique gives the best results in terms of error, which is expected due to its specific (i.e., not generalized) nature to find the exact values of parameters. The method is not sensitive to noise until the threshold for the detection is reached, i.e. when the input SNR is approximately -5 dB. When the threshold is reached, the error sharply increases, since some modes are not detected.

Chapter 5

Compressive sensing in image denoising

Contents

This chapter presents further work on compressive sensing, which can be considered as an extension of results presented in the previous chapters. Here, we focus on the reconstruction and error calculation of general images, analyzed in the two-dimensional discrete cosine transform (2D-DCT) domain.

In the first part of the chapter, a method for recovery of sparse images is presented. The algorithm is based on a gradient-descent procedure. The proposed algorithm performs blindly to detect and reconstruct corrupted pixels. The assumption is that the image is sparse in the 2D-DCT domain and that the noise degrades this property. The advantage of the proposed reconstruction algorithm is that the uncorrupted pixels remain unchanged in the reconstruction process. The proposed method can be used without explicitly imposing the image sparsity. The algorithm is compared with some state-of-the-art algorithms, proving its reconstruction robustness.

In most cases, images are approximately sparse or nonsparse in the 2D-DCT domain. The sparsification step of images can produce the error in their final reconstruction. In the second part of the chapter, the exact error is derived for nonsparse images reconstructed under the sparsity assumption. The mean squared error calculation theory is compared to the corresponding statistical values.

5.1 Problem formulation

Let consider an 8-bit $N \times M$ image, $x(n,m)$, meaning that its pixel values are integers between 0 and 255. For compressive sensing methods, it should be assumed that the image is sparse in the 2D-DCT domain.

Definition 5.1
The 2D-DCT (and its inverse) of an image $x(n,m)$ is defined by [8, 116]

$$\begin{aligned} X(k,l) &= \sum_{n=0}^{N-1}\sum_{m=0}^{M-1} x(n,m)\varphi(k,l,n,m) \\ x(n,m) &= \sum_{k=0}^{N-1}\sum_{l=0}^{M-1} X(k,l)\psi(n,m,k,l), \end{aligned} \tag{5.1}$$

where $\varphi(k,l,n,m)$ is the 2D-DCT basis function and $\psi(n,m,k,l)$ is the 2D-DCT inverse basis function, defined as

$$\varphi(k,l,n,m) = \psi(n,m,k,l) = c_k c_l \cos\left(\frac{\pi(2n+1)k}{2N}\right)\cos\left(\frac{\pi(2m+1)l}{2M}\right). \tag{5.2}$$

The constants c_k and c_l are scaling constants defined as

$$c_k = \begin{cases} 1/\sqrt{N}, & \text{for } k=0 \\ \sqrt{2/N}, & \text{for } k \neq 0 \end{cases} \qquad c_l = \begin{cases} 1/\sqrt{M}, & \text{for } l=0 \\ \sqrt{2/M}, & \text{for } l \neq 0 \end{cases}. \tag{5.3}$$

In matrix form, the image and its 2D-DCT can be written as $\mathbf{x} = \mathbf{\Psi X}$ and $\mathbf{X} = \mathbf{\Phi x}$, respectively, where $\mathbf{\Psi}$ and $\mathbf{\Phi}$ are the rearranged matrices defined in (5.2). For the compressive sensing framework, we assume that the considered image is K-sparse in the 2D-DCT domain and that only $N_A \ll NM$ of its pixels are available at the positions $(n,m) \in \mathbb{N}_{\mathbb{A}} = \{(n_1,m_1),(n_2,m_2),...,(n_{N_A},m_{N_A})\}$. Consequently, assuming that the positions of the corrupted pixels are known, we can set their values to zero (as it is done in the initial estimate). The initial image form is then presented as

$$x_a(n,m) = \begin{cases} x(n,m) & \text{for } (n,m) \in \mathbb{N}_{\mathbb{A}} \\ 0 & \text{elsewhere.} \end{cases} \tag{5.4}$$

Note that the nonzero entries of (5.4) are the measurements within the CS framework

$$\mathbf{y} = [x(n_1,m_1), x(n_2,m_2), ..., x(n_{N_A},m_{N_A})]^T. \tag{5.5}$$

The image is sparsified according to the quantization matrix of the JPEG standard [116]. The quality factor (QF) defines the level of sparsification of the image. For different QFs, which influence the level of sparsity in the block, the quantization matrix is defined as

$$Q_{QF} = \text{round}(Q_{50} \cdot q), \tag{5.6}$$

where Q_{50} is the standard quantization matrix and the value q is the level presented as

$$q = \begin{cases} 2 - 0.02QF, \text{ for } QF \geq 50 \\ \frac{50}{QF}, \qquad\quad \text{for } QF < 50 \end{cases}. \tag{5.7}$$

The reconstruction procedure is performed using blocks of the image of size 8×8. Then, each block is analyzed and recovered separately. After each block is recovered, the full image is restored by combining the blocks back. Also, different quality factors are assumed to compare the performance of the algorithm with various sparsity levels.

5.2 Gradient-based reconstruction algorithm

Here, we will consider an image with $N_Q = NM - N_A$ pixels affected by noise. The amplitude of noise can be within the range of the available N_A pixel values. The aim is to reconstruct the corrupted pixels without knowing the number of affected pixels nor their positions, while not changing the values of available noise-free pixels.

5.2.1 Algorithm

The algorithm is based on the minimization of the sparsity measure through iterations [34, 117, 118]. Each particular image pixel is considered as possibly corrupted. Its value is varied by adding an estimation parameter, $\pm\Delta$. For each pixel, the gradient sparsity measure $\|\mathbf{X}\|_1$ is estimated based on its finite difference value. The pixel producing the largest gradient estimate is marked as corrupted and omitted. Then the iterative process is repeated until the sparsity measure does not change significantly. All detected corrupted pixels are set as unavailable. When the set of corrupted pixels is defined, the reconstruction is performed. The reconstruction procedure is described in Algorithm 6 of Appendix [34]. The corrupted pixels are varied through the reconstruction procedure to produce the most sparse solution. During the reconstruction process, the uncorrupted pixels remain unchanged.

The algorithm can also be used when the noise is much stronger than the signal itself, meaning that the corrupted pixels are distinguishable from the uncorrupted pixels (salt-and-pepper noise), so that their positions are easily found. When we have strong noise in the image, we will omit the corrupted pixels from the calculations and continue with the reconstruction as described in Algorithm 6 of the Appendix.

5.2.2 Corrupted pixel selection procedure

For the selection of potentially corrupted pixels, let assume that one pixel is corrupted at a position (n_0, m_0). The image with the corrupted pixel will be defined by $x_a(n, m)$, where the

corrupted pixel is $x_a(n_0, m_0) = x(n_0, m_0) + z$, with z being the noise value. Following the Algorithm 6, the corrupted pixel is varied according to $\pm\Delta$ to form

$$\begin{aligned} x_a^+(n,m) &= x(n,m) + (z+\Delta)\,\delta(n-n_0, m-m_0) \\ x_a^-(n,m) &= x(n,m) + (z-\Delta)\,\delta(n-n_0, m-m_0). \end{aligned} \tag{5.8}$$

The gradient of the sparsity measure is estimated as

$$g(n_0, m_0) = \left\|\mathbf{X}_a^+\right\|_1 - \left\|\mathbf{X}_a^-\right\|_1 \tag{5.9}$$

where $\mathbf{X}_a^+$ and $\mathbf{X}_a^-$ are the 2D-DCT of the images (5.8) with coefficients $X_a^+(k,l)$ and $X_a^-(k,l)$, respectively.

Assume that the 2D-DCT of the corrupted pixel is $(z \pm \Delta)\,\varphi(k, l, n_0, m_0)$. The sparsity measures can be approximated as a sum of the original image measure and the measure of the corrupted pixel (with the Δ shifts)

$$\begin{aligned} \left\|\mathbf{X}_a^+\right\|_1 &= \sum_{k,l=0}^{N-1} \left|X_a^+(k,l)\right| \cong \|\mathbf{X}\|_1 + |z+\Delta|\,C \\ \left\|\mathbf{X}_a^-\right\|_1 &= \sum_{k,l=0}^{N-1} \left|X_a^-(k,l)\right| \cong \|\mathbf{X}\|_1 + |z-\Delta|\,C \end{aligned} \tag{5.10}$$

where C which depends on the corrupted pixel position (m_0, n_0) and the size of the image. The gradient is then

$$g(n_0, m_0) = \left\|\mathbf{X}_a^+\right\|_1 - \left\|\mathbf{X}_a^-\right\|_1 \cong |z+\Delta|\,C - |z-\Delta|\,C. \tag{5.11}$$

For variations from the true image value smaller than the step $|z| < \Delta$ we get

$$g(n_0, m_0) \cong 2Cz \sim z. \tag{5.12}$$

From (5.12), it can be concluded that the gradient is proportional to the intensity of noise at the corrupted pixel.

5.2.3 Pixel selection and reconstruction

The aim is to find the positions of corrupted pixels and select which pixels are uncorrupted. According to the previous subsection, this will be achieved by repeating steps 9-15 of the gradient-based reconstruction procedure in Algorithm 6 in the Appendix. Note that this procedure should be repeated for all pixels, in order to estimate which pixels are corrupted. The full method of pixel selection and recovery is presented in Algorithm 7 of the Appendix. During the reconstruction, we include all previously detected positions of corrupted pixels in each iteration. The procedure is repeated until a required precision is achieved. The algorithm is repeated for each block, and the image is combined back when all blocks are reconstructed.

In the reconstruction, we have concluded that the edge effects of some blocks can influence reconstruction success. Small pieces of the neighboring blocks may appear at the edging pixels in the current block. Since the algorithm finds the solution by minimizing the sparsity, it will recognize those small pieces as disturbances in the considered block. It will try to select them as corrupted pixels, meaning that they are removed. To overcome this problem, the pixel selection analysis is done using partially overlapping blocks. Only the central parts of the blocks (the ones which are not overlapped) are included for the final reconstruction.

5.2.4 Results

The image "Peppers", of size $N \times M = 512 \times 512$, is used to demonstrate the presented method. The image is affected by a combination of two noise types. These disturbing noise types are the salt-and-pepper noise (having intensity either 0 or 255) and the uniform noise (noise in the range between 0 and 255). In color images, the noise is randomly positioned in each of the three channels (R, G, and B) separately. Assume that 50% of the pixels are affected by noise, with 10% of them being the uniform noise. The results of the presented denoising algorithm are compared with a 5×5 median filter and two state-of-the-art methods. The first method is from [119], based on adaptive filtering. The second considered method is the total-variation imaging algorithm from [120, 121].

The results are shown in Fig. 5.1. The original image is presented in Fig. 5.1 (top left). The image with the corrupted pixels is shown in Fig. 5.1 (top right). The reconstruction using the proposed method and the reconstruction of the image using the 5×5 marginal median filter are presented in Fig. 5.1 (middle). In Fig. 5.1 (bottom), the reconstruction with the two state-of-the-art algorithms is shown. The methods for comparing the reconstruction results, along with the specific values of the comparison parameters, will be given next.

Comparison

The performance of the algorithm will be examined using the SSIM index as well as MAE and PSNR, with respect to the original image. The SSIM index is introducted [122] and defined as a function of luminance, contrast and structure comparison between two images, i.e.

$$\mathrm{SSIM}(\mathbf{x}_o, \mathbf{x}_r) = \frac{(2\mu_{x_o}\mu_{x_r} + c_1)(2\sigma_{x_o x_r} + c_2)}{(\mu_{x_o}^2 + \mu_{x_r}^2 + c_1)(\sigma_{x_o}^2 + \sigma_{x_r}^2 + c_2)} \tag{5.13}$$

where $\mathbf{x_o}$ and $\mathbf{x_r}$ are the original and the reconstructed image, respectively. The values μ_{x_o}, μ_{x_r} correspond to the mean values of the two images, $\sigma_{x_o x_r}$ is the covariance between $\mathbf{x_o}$ and $\mathbf{x_r}$, $\sigma_{x_o}^2$, $\sigma_{x_r}^2$ are the variances of the considered images. The constants c_1 and c_2 are used for stabilization. The SSIM value is a constant between the values 0 and 1, where 1 is obtained when the similarity between images is complete and 0 is obtained when no similarity is present.

The MAE is calculated as

$$MAE(\mathbf{x}_o, \mathbf{x}_r) = \mathrm{mean}(\mathrm{mean}(|\mathbf{x}_o - \mathbf{x}_r|)). \tag{5.14}$$

Original image

Noisy image

Reconstructed using proposed method

Reconstructed using 5×5 median filter

Reconstructed using TV-L1

Reconstructed using two-stage adaptive method

Figure 5.1: Reconstruction of color image "Peppers" corrupted with 50% combined noise: Image with corrupted pixels (top left); Reconstruction using the proposed method (middle left); Reconstruction using the 5×5 median filter (middle right); Reconstruction using the two state-of-the-art algorithms (bottom).

Table 5.1 shows the SSIM index and MAE for different quality factors different percenage of corrupted pixels in the grayscale image "Lena", presented in Fig. 5.2 (top left). Note that the quality factor (which determines the sparsity level of the block) nor the number of the corrupted pixels are not known by the gradient algorithm.

Table 5.1: SSIM index and MAE between original and reconstructed image "Lena" for various quality factor QF and percentage of corrupted pixels.

	SSIM				MAE			
QF	**12.5%**	**25%**	**37.5%**	**50%**	**12.5%**	**25%**	**37.5%**	**50%**
5	0.99	0.99	0.91	0.64	0.41	1.08	3.28	10.80
10	0.99	0.98	0.92	0.64	0.38	1.05	3.18	11.63
25	0.99	0.98	0.92	0.63	0.37	1.08	3.27	12.28
50	0.99	0.98	0.92	0.62	0.42	1.17	3.45	12.79
75	0.99	0.98	0.91	0.61	0.47	1.31	3.60	13.10
90	0.99	0.97	0.91	0.60	0.61	1.54	3.85	13.75

Table 5.2: PSNR and SSIM for the reconstruction of the eight test images in Fig. 5.2. The results are obtained by the proposed, two-stage (2-stage) adaptive algorithm [119] and total variation L1 (TV-L1) [120, 121] method.

	PSNR			SSIM		
Test image	**Proposed**	**2-stage**	**TV-L1**	**Proposed**	**2-stage**	**TV-L1**
Pout	45.87	39.59	39.46	0.98	0.63	0.92
Lifting body	43.92	35.90	40.15	0.99	0.73	0.94
Peppers	42.74	39.84	38.58	0.99	0.62	0.95
Lena	41.22	35.87	35.94	0.98	0.75	0.91
Boat	39.33	34.15	34.41	0.97	0.73	0.85
Butterfly	39.22	36.20	35.04	0.98	0.81	0.88
Camera	36.54	36.36	33.01	0.94	0.81	0.79
Tissue	32.44	30.92	29.35	0.91	0.86	0.73

The peak-to-noise ratio (PSNR) and the SSIM index will be used for the comparison of the algorithm with the state-of-the-art algorithms based on a set of eight images from MATLAB software. The PSNR for an 8-bit image is

$$PSNR(\mathbf{x}_o, \mathbf{x}_r) = 10 \log_{10} \left(\frac{255^2}{\text{mean}(\text{mean}(|\mathbf{x}_o - \mathbf{x}_r|)^2)} \right). \tag{5.15}$$

The eight test images are shown in Fig. 5.2, including the image peppers, analyzed earlier. The comparison among the reconstruction algorithms for eight test images corrupted by 50% of combined noise, is given in Table 5.2. This table shows the robustness of the proposed algorithm in comparison with the other two methods for image reconstruction.

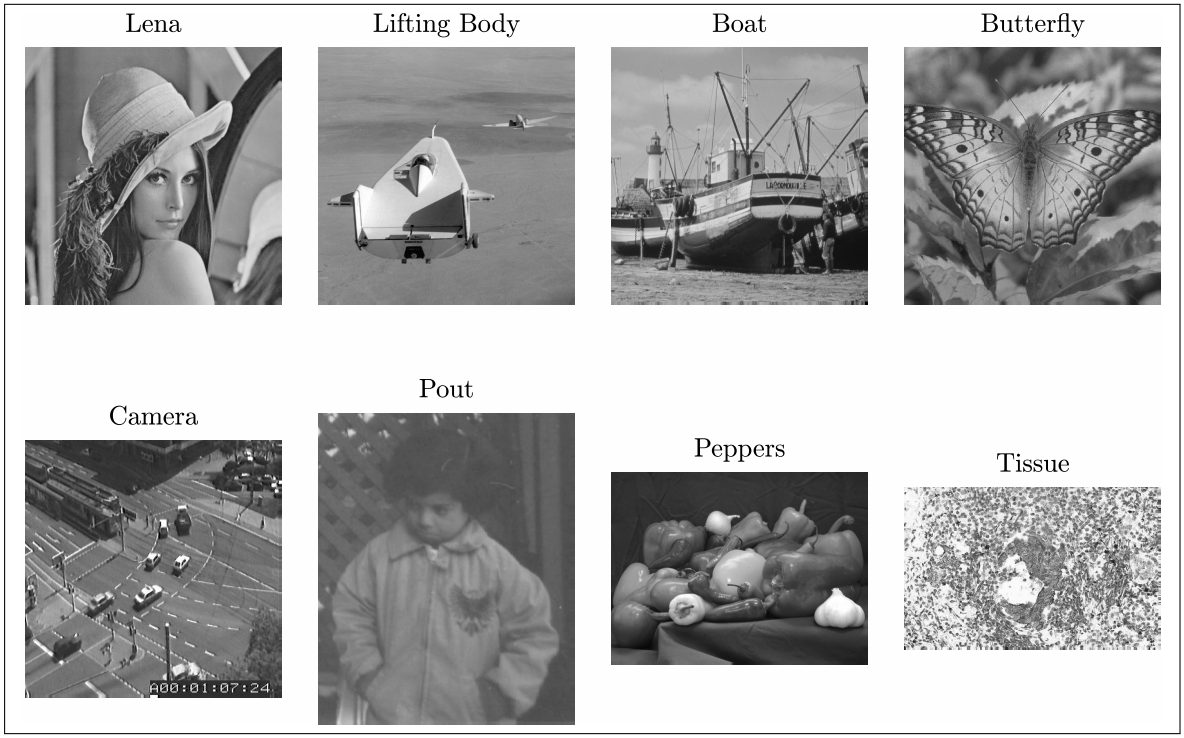

Figure 5.2: The eight test images used for the comparison between the proposed algorithm and two state-of-the-art algorithms.

5.3 Error calculation in nonsparse images

In the previous subsection, the images are considered as being sparsified according to the quality factor and the corresponding quantization matrix, since a significant amount of the energy is concentrated within a small number of 2D-DCT components. However, the remaining nonzero coefficients make that the original images are only approximately sparse or nonsparse. Since, in CS theory, sparsity should be assumed, the reconstruction algorithms will not be able to recover small valued coefficients of nonsparse signals. The exact formulation of the expected squared reconstruction error in the case of nonsparse images is given in the form of a theorem [123].

Theorem: *Assume an image, which is nonsparse in the 2D-DCT domain, with the largest amplitudes in this domain* A_r, $r = 1, 2, ..., K$. *Assume that only* N_A *out of total* NM *samples are available, where* $1 \ll N_A < NM$. *Also assume that the image is reconstructed under the assumption that it is* K*-sparse. The energy of error in the* K *reconstructed coefficients* $\|\mathbf{X}_K - \mathbf{X}_R\|_2^2$ *is related to the energy of unreconstructed components* $\|\mathbf{X}_{K0} - \mathbf{X}\|_2^2$ *coefficients as follows:*

$$\|\mathbf{X}_K - \mathbf{X}_R\|_2^2 = \frac{K(NM - N_A)}{N_A(NM - 1)} \|\mathbf{X}_{K0} - \mathbf{X}\|_2^2, \tag{5.16}$$

where

$$\|\mathbf{X}_K - \mathbf{X}_R\|_2^2 = \frac{K(NM - N_A)}{N_A(NM-1)} \sum_{r=K+1}^{NM} A_r^2, \tag{5.17}$$

and

$$\|\mathbf{X}_{K0} - \mathbf{X}\|_2^2 = \sum_{r=K+1}^{NM} A_r^2. \tag{5.18}$$

The proof is based on the initial estimate of the image

$$X_0(k,l) = \sum_{(n,m)\in\mathbb{N}_{\mathbb{A}}} x(n,m)\varphi_N(n,k)\varphi_M(m,l) \tag{5.19}$$

where $k = 0, 1, ..., n-1,\ l = 0, 1, ..., M-1$. In a matrix form we can write

$$\mathbf{X_0} = \mathbf{A^T y}. \tag{5.20}$$

The coefficients in (5.19) act as random variables, with different statistical properties at positions of the image components, $(k,l) = (k_r, l_r)$, and positions not corresponding to image components, $(k,l) \neq (k_r, l_r)$.

5.3.1 Noise-only coefficients

Let assume first the case when $K = 1$ at (k_1, l_1). Assuming the amplitude to be $A_1 = 1$, the initial estimate can be written as

$$X_0(k,l) = \sum_{(n,m)\in\mathbb{N}_{\mathbb{A}}} \varphi_N(n,k_1)\varphi_M(m,l_1)\varphi_N(n,k)\varphi_M(m,l). \tag{5.21}$$

The variable

$$x_{k_1 l_1}(n,m,k,l) = \varphi_N(n,k_1)\varphi_M(m,l_1)\varphi_N(n,k)\varphi_M(m,l) \tag{5.22}$$

is random for random set of values of (n,m) where the image is available. Its initial estimate is

$$X_0(k,l) = \sum_{(n,m)\in\mathbb{N}_{\mathbb{A}}} x_{k_1 l_1}(n,m,k,l). \tag{5.23}$$

When $(k,l) \neq (k_1, l_1)$, the 2D-DCT coefficients correspond to position where the image component is not present. In this case, the initial estimate behaves as a random Gaussian variable [53]. Following the orthogonality of the basis function and the fact that values of $x_{k_1 l_1}(n,m,k,l)$ are equally distributed, the mean value of the initial estimate is

$$\mu_{X_0(k,l)} = E\{X_0(k,l)\} = 0,\ (k,l) \neq (k_1, l_1). \tag{5.24}$$

In the case of a coefficient corresponding to the image component, using the same orthogonality property and the assumption of equal distribution of values $x_{k_1 l_1}(n, m, k, l)$, it follows that

$$\mu_{X_0(k,l)} = E\{X_0(k,l)\} = \frac{N_A}{NM},\ (k,l) = (k_1, l_1). \tag{5.25}$$

For the zero-mean random variable, the variance is

$$\sigma^2_{X_0(k,l)} = E\Big\{ \sum_{(n,m)\in\mathbb{N}_\mathbb{A}} x^2_{k_1 l_1}(n,m,k,l) + \sum_{(n,m)\in\mathbb{N}_\mathbb{A}} \sum_{\substack{(i,j)\in\mathbb{N}_\mathbb{A} \\ (i,j)\neq(n,m)}} x_{k_1 l_1}(n,m,k,l) x_{k_1 l_1}(i,j,k,l) \Big\}. \tag{5.26}$$

As in the case when $(k,l) \neq (k_1, l_1)$ is observed, it can be concluded that

$$\sum_{n=0}^{N-1} \sum_{m=0}^{M-1} x_{k_1 l_1}(n,m,k,l) = 0. \tag{5.27}$$

Multiplying the left and the right side of (5.27) by $x_{k_1 l_1}(i,j,k,l)$, and taking the expectation of both sides we get

$$E\Big\{ \sum_{n=0}^{N-1} \sum_{m=0}^{M-1} x_{k_1 l_1}(n,m,k,l) x_{k_1 l_1}(i,j,k,l) \Big\} = 0, \tag{5.28}$$

with $(i,j) \in \mathbf{N}$. Values $x_{k_1 l_1}(n,m,k,l)$ are equally distributed. Therefore, the terms $E\{x_{k_1 l_1}(n,m,k,l) x_{k_1 l_1}(i,j,k,l)\}$ for $(n,m) \neq (i,j)$ are the same and equal to a constant D. The total number of these terms is $NM - 1$. Furthermore, based on (5.28) we get

$$(NM-1)\, D + E\left\{x^2_{k_1 l_1}(n,m,k,l)\right\} = 0. \tag{5.29}$$

The initial variance definition can be written as

$$\sigma^2_{X_0(k,l)} = N_A E\{x^2_{k_1 l_1}(n,m,k,l)\} + (N_A^2 - N_A) D, \tag{5.30}$$

as there are exactly N_A expectations with quadratic terms in the first summation and $N_A(N_A - 1)$ terms in the second variance summation equal to D. In order to determine the unknown term $E\left\{x^2_{k_1 l_1}(n,m,k,l)\right\}$, several special cases should be taken into account.

Consider the general case when $k \neq k_1,\ k \neq N - k_1,\ l \neq l_1,\ l \neq M - l_1$. Then

$$E\{x^2_{k_1 l_1}(n,m,k,l)\} = E\{\varphi^2_N(n,k_1)\varphi^2_M(m,l_1)\} \times E\{\varphi^2_N(n,k)\varphi^2_M(m,l)\} = \frac{1}{N^2 M^2} \tag{5.31}$$

holds. Incorporating this result into (5.29) we get that

$$D = -\frac{1}{N^2 M^2} \frac{1}{NM-1}. \tag{5.32}$$

Next, based on (5.30), the variance can be written as

$$\sigma^2_{X_0(k,l)} = \frac{N_A(NM - N_A)}{N^2M^2(NM - 1)}. \tag{5.33}$$

This result also holds when $(k_1, l_1) = (0, 0)$. The special cases of the 2D-DCT indices are considered in [123]. Note that, when $A_1 \neq 1$, the result is multiplied by A_1^2. As $NM \gg 1$, an accurate approximation, when all special cases are included, for the average variance of noise-only coefficients follows

$$\sigma^2_{X_0} \approx A_1^2 \frac{N_A(NM - N_A)}{N^2M^2(NM - 1)}. \tag{5.34}$$

In the realistic case of several components in the 2D-DCT domain, the observed random variable becomes

$$X_0(k, l) = \sum_{(n,m)\in\mathbb{N}_{\mathbb{A}}} \sum_{r=1}^{K} A_r \varphi_N(n, k_r)\varphi_M(m, l_r) \times \varphi_N(n, k)\varphi_M(m, l). \tag{5.35}$$

In this case, the coefficients at noise-only positions $(k, l) \neq (k_r, l_r)$ are random variables formed as the summation of independent zero-mean Gaussian variables over r. The unavailable pixels in each component add to the noise. The noise from each component is proportional to the squared amplitude of that component, following (5.34) with $A_r,\ r = 1, ..., K$. Therefore, the mean value of the K 2D-DCT coefficients is

$$\mu_{X_0(k,l)} = \frac{N_A}{NM} \sum_{r=1}^{K} A_r \delta(k - k_r, l - l_r). \tag{5.36}$$

The average variance of noise-only coefficients in this case easily follows as

$$\sigma^2_{X_0} = \sum_{r=1}^{K} A_r^2 \frac{N_A(NM - N_A)}{N^2M^2(NM - 1)}. \tag{5.37}$$

5.3.2 Nonsparse images reconstruction error

The image is reconstructed under the K-sparsity constraint. The conditions for a unique reconstruction are assumed to be met. According to (5.37), one nonreconstructed element behaves as a noise with variance

$$\sigma^2_{X_0} = A_r^2 \frac{N_A(NM - N_A)}{N^2M^2(NM - 1)}. \tag{5.38}$$

which leads that the variance of all components which are not reconstructed will be

$$\sigma^2_T = \sum_{r=K+1}^{NM} A_r^2 \frac{N_A(NM - N_A)}{N^2M^2(NM - 1)}. \tag{5.39}$$

The total noise energy from the nonreconstructed coefficients in the K reconstructed components is

$$\|\mathbf{X}_K - \mathbf{X}_R\|_2^2 = K\frac{N^2M^2}{N_A^2}\sigma_T^2 = \frac{K(NM-N_A)}{N_A(NM-1)}\sum_{r=K+1}^{NM} A_r^2. \tag{5.40}$$

Note that the noise of the nonreconstructed coefficients can be related to their energy,

$$\|\mathbf{X}_K - \mathbf{X}\|_2^2 = \sum_{r=K+1}^{NM} A_r^2. \tag{5.41}$$

From the previous analysis it follows that

$$\|\mathbf{X}_K - \mathbf{X}_R\|_2^2 = \frac{K(NM-N_A)}{N_A(NM-1)}\|\mathbf{X}_K - \mathbf{X}\|_2^2. \tag{5.42}$$

This completes the proof of the theorem.

5.3.3 Numerical results

An image set with standard MATLAB images is used for the numerical examination of the theorem. The set is presented in Fig. 5.3. Each image is split into $B \times B = 16 \times 16$ blocks. The reconstruction is performed under the sparsity assumption $K = 16$ per block, with 60% of pixels available. The reconstruction is performed using the OMP algorithm. The errors are calculated for each block separately and then the results are averaged over all blocks in the image. The statistical PSNR, for an 8-bit image, is

$$PSNR_{statistics} = 10\log\left(\frac{255^2}{||\mathbf{X}_K - \mathbf{X}_R||_2^2}\right), \tag{5.43}$$

and the theoretical PSNR, according to the thereom, is

$$PSNR_{theory} = 10\log\left(\frac{255^2}{K\frac{B^2-N_A}{N_A(B^2-1)}||\mathbf{X}_K - \mathbf{X}||_2^2}\right). \tag{5.44}$$

The results are presented in Table 5.3, confirming a high agreement between the results.

Table 5.3: Statistical and theoretical calculations of the PSNR for 8 test images in Fig. 5.3.

Test image	**Lifting body**	**Boat**	**Pout**	**Autumn**	**Pirate**	**Pears**	**Peppers**	**Football**
Statistics	82.97	81.97	80.35	90.81	70.97	78.77	79.16	68.69
Theory	83.11	82.13	80.42	90.92	71.10	78.86	79.23	68.63

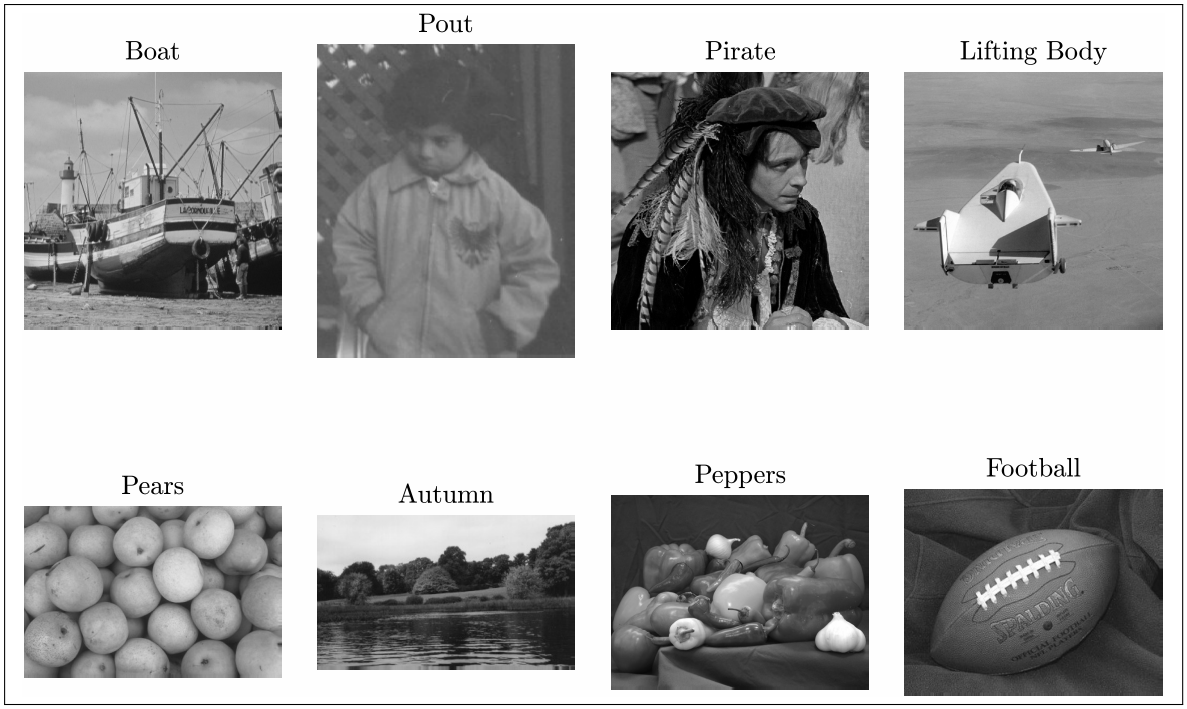

Figure 5.3: The eight test images used for the error analysis.

Conclusions

The compressive sensing theory can be used to develop a successful sampling technique in different fields and various signals. The idea of using a small number of measurements for the signal acquisition improves the efficiency of storage, memory requirements, and transmission of signals. Accurate recovery of signals sampled in such a way is the primary goal of compressive sensing and sparse signal processing. Since many signals in nature can be represented as sparse in some transformation domain, the technique showed huge potential in real-world problems. However, the idea is not yet fully developed and applied in the underwater acoustics field. The non-stationary nature of such signals makes it suitable for the analysis using time-frequency tools under the signal processing approach. In the compressive sensing sense, non-stationary signals are only approximately sparse or nonsparse in the corresponding transformation domain.

In this thesis, three major points are considered, with the aim to find a successful solution for applying compressive sensing methods to the underwater acoustics. It is important to notice the nonsparse characteristic of the signals received in dispersive channels. The nonsparsity, in general, will produce errors in the reconstruction of signals considered as sparse in their nature. The exact error generated in the reconstruction of time-varying signals was derived in this thesis. The uniform and random sampling were considered, together with a generalization of the error depending on the sampling method. For a more realistic case, the effect of quantization, as a crucial step for the hardware implementation, is analyzed. In the end, the noise folding effect is considered as well.

In addition to the dispersive underwater channel analysis, wideband sonar images are considered as an important topic in the underwater acoustics. In the literature, only basic forms of signals were used for the transmission. The usage of various sequences showed interesting results in the reconstruction of sonar signals. The implementation of compressive sensing techniques on those signals was considered. We showed that the reconstruction of sonar signals could be significantly improved in detecting and localizing sparse targets. Dispersive channels introduce multi-component non-stationary signals as an additional challenge to this field. Combining the previously studied reconstruction, together with the principles of the polynomial Fourier transform and mode decomposition, the time-varying components of the sonar signals are successfully detected, decomposed, and analyzed.

The dispersive media was perceived in two different approaches: the decomposition of signals received at a misaligned sensor, and a signal received from a dispersive isovelocity shallow water environment. Three different methods were considered: high-resolution local polynomial case, the dual extension of the polynomial Fourier domain, and a model-function based technique. It is concluded that the model-based method gives the best results in terms of error, which is expected due to its specific nature to find the appropriately adjusted forms and the values of corresponding parameters. The method is not sensitive to the noise until the threshold for the detections is reached. Also, a more general approach, based on the polynomial

Fourier transform, is introduced. Although the mode forms do not fully coincide with the polynomial forms, it was seen that a reasonable error rate is achieved, with a quite general model. The method is further improved by using a sparse decomposition and reconstruction of components using the iterative algorithm.

The presented theory and methods can be extended in various directions. In the decomposition of the dispersive media, the high-resolution techniques showed promising results combined with the polynomial Fourier transform. Another interesting course is in the error calculation, which was developed for the time-varying part of the signals received in the dispersive media. The derivation can be further extended in the direction of the dual polynomial Fourier transformation domain, as the sparsity domain. The last approach is based on the combination of the appropriate sequence form selection in the transmission part of the setup. The combination of the suitable sequences, combined with the dual extension as the sparsity domain and the appropriate error calculation, could result in a robust solution for further analysis of signals transmitted underwater.

Finally, some of the results and developed methods are applied to the general image denoising problem, showing that the presented results and methods are not strictly limited to the underwater acoustic signal analysis.

Bibliography

[1] C. E. Shannon, "Communication in the presence of noise," *Proceedings of the IRE*, vol. 37, no. 1, pp. 10–21, 1949.

[2] H. Nyquist, "Certain topics in telegraph transmission theory," *Transactions of the American Institute of Electrical Engineers*, vol. 47, no. 2, pp. 617–644, 1928.

[3] V. A. Kotelnikov, "On the transmission capacity of" ether" and wire in electrocommunications," *http://ict. open. ac. uk/classics/l. pdf*, 1933.

[4] J. M. Whittaker, *Interpolatory function theory*, vol. 33. The University Press, 1935.

[5] B. Boashash, *Time-frequency signal analysis and processing: a comprehensive reference*. Academic Press, 2015.

[6] C. Leon, "Time-frequency analysis: theory and applications," *USA: Pnentice Hall*, 1995.

[7] L. Stankovic, M. Dakovic, and T. Thayaparan, *Time-frequency signal analysis with applications*. Artech house, 2014.

[8] L. Stankovic, *Digital signal processing: with selected topics: Adaptive systems, Time-frequency analysis, Sparse signal processing*. CreateSpace, 2015.

[9] L. Stankovic, S. Stankovic, and M. Dakovic, "From the stft to the wigner distribution [lecture notes]," *IEEE Signal Processing Magazine*, vol. 31, no. 3, pp. 163–174, 2014.

[10] P. Flandrin and P. Borgnat, "Time-frequency energy distributions meet compressed sensing," *IEEE Transactions on Signal Processing*, vol. 58, no. 6, pp. 2974–2982, 2010.

[11] M. G. Amin, B. Jokanovic, Y. D. Zhang, and F. Ahmad, "A sparsity-perspective to quadratic time–frequency distributions," *Digital Signal Processing*, vol. 46, pp. 175–190, 2015.

[12] D. Angelosante, G. B. Giannakis, and E. Grossi, "Compressed sensing of time-varying signals," in *2009 16th International Conference on Digital Signal Processing*, pp. 1–8, IEEE, 2009.

[13] E. Sejdić, I. Orović, and S. Stanković, "Compressive sensing meets time–frequency: an overview of recent advances in time–frequency processing of sparse signals," *Digital signal processing*, vol. 77, pp. 22–35, 2018.

[14] D. L. Donoho *et al.*, "Compressed sensing," *IEEE Transactions on information theory*, vol. 52, no. 4, pp. 1289–1306, 2006.

[15] E. Candes, J. Romberg, and T. Tao, "Robust uncertainty principles: exact signal reconstruction from highly incomplete frequency information," *IEEE Transactions on Information Theory*, vol. 52, no. 2, pp. 489–509, 2006.

[16] D. L. Donoho, M. Elad, and V. N. Temlyakov, "Stable recovery of sparse overcomplete representations in the presence of noise," *IEEE Transactions on information theory*, vol. 52, no. 1, pp. 6–18, 2005.

[17] R. G. Baraniuk, "Compressive sensing," *IEEE signal processing magazine*, vol. 24, no. 4, 2007.

[18] E. Candes and M. Wakin, "An introduction to compressive sampling," *IEEE Signal Processing Magazine*, vol. 2, no. 25, pp. 21–30, 2008.

[19] M. Elad, *Sparse and redundant representations: from theory to applications in signal and image processing*. Springer Science & Business Media, 2010.

[20] Y. C. Eldar and G. Kutyniok, *Compressed sensing: theory and applications*. Cambridge university press, 2012.

[21] H. Boche, R. Calderbank, G. Kutyniok, and J. Vybíral, *Compressed sensing and its applications*. Springer, 2015.

[22] M. A. Davenport, M. F. Duarte, Y. C. Eldar, and G. Kutyniok, "Introduction to compressed sensing," *preprint*, vol. 93, no. 1, p. 2, 2011.

[23] M. Fornasier and H. Rauhut, "Compressive sensing.," *Handbook of mathematical methods in imaging*, vol. 1, pp. 187–229, 2015.

[24] E. J. Candes, "The restricted isometry property and its implications for compressed sensing," *Comptes rendus mathematique*, vol. 346, no. 9-10, pp. 589–592, 2008.

[25] S. G. Mallat and Z. Zhang, "Matching pursuits with time-frequency dictionaries," *IEEE Transactions on signal processing*, vol. 41, no. 12, pp. 3397–3415, 1993.

[26] J. A. Tropp, "Greed is good: Algorithmic results for sparse approximation," *IEEE Transactions on Information theory*, vol. 50, no. 10, pp. 2231–2242, 2004.

[27] J. A. Tropp and A. C. Gilbert, "Signal recovery from random measurements via orthogonal matching pursuit," *IEEE Transactions on information theory*, vol. 53, no. 12, pp. 4655–4666, 2007.

[28] D. Needell and J. A. Tropp, "Cosamp: Iterative signal recovery from incomplete and inaccurate samples," *Applied and computational harmonic analysis*, vol. 26, no. 3, pp. 301–321, 2009.

[29] I. Daubechies, M. Defrise, and C. De Mol, "An iterative thresholding algorithm for linear inverse problems with a sparsity constraint," *Communications on Pure and Applied Mathematics: A Journal Issued by the Courant Institute of Mathematical Sciences*, vol. 57, no. 11, pp. 1413–1457, 2004.

[30] A. Beck and M. Teboulle, "A fast iterative shrinkage-thresholding algorithm for linear inverse problems," *SIAM journal on imaging sciences*, vol. 2, no. 1, pp. 183–202, 2009.

[31] X. Lv, G. Bi, and C. Wan, "The group lasso for stable recovery of block-sparse signal representations," *IEEE Transactions on Signal Processing*, vol. 59, no. 4, pp. 1371–1382, 2011.

[32] R. Tibshirani, "Regression shrinkage and selection via the lasso," *Journal of the Royal Statistical Society: Series B (Methodological)*, vol. 58, no. 1, pp. 267–288, 1996.

[33] M. A. Figueiredo, R. D. Nowak, and S. J. Wright, "Gradient projection for sparse reconstruction: Application to compressed sensing and other inverse problems," *IEEE Journal of selected topics in signal processing*, vol. 1, no. 4, pp. 586–597, 2007.

[34] L. Stanković, M. Daković, and S. Vujović, "Adaptive variable step algorithm for missing samples recovery in sparse signals," *IET Signal Processing*, vol. 8, no. 3, pp. 246–256, 2014.

[35] D. Needell and R. Ward, "Stable image reconstruction using total variation minimization," *SIAM Journal on Imaging Sciences*, vol. 6, no. 2, pp. 1035–1058, 2013.

[36] F. Krahmer, C. Kruschel, and M. Sandbichler, "Total variation minimization in compressed sensing," in *Compressed Sensing and its Applications*, pp. 333–358, Springer, 2017.

[37] C. Poon, "On the role of total variation in compressed sensing," *SIAM Journal on Imaging Sciences*, vol. 8, no. 1, pp. 682–720, 2015.

[38] T. Blumensath and M. E. Davies, "Iterative hard thresholding for compressed sensing," *Applied and computational harmonic analysis*, vol. 27, no. 3, pp. 265–274, 2009.

[39] H.-J. M. Shi, M. Case, X. Gu, S. Tu, and D. Needell, "Methods for quantized compressed sensing," in *2016 Information Theory and Applications Workshop (ITA)*, pp. 1–9, IEEE, 2016.

[40] T. Blumensath, M. Yaghoobi, and M. E. Davies, "Iterative hard thresholding and l0 regularisation," in *2007 IEEE International Conference on Acoustics, Speech and Signal Processing-ICASSP'07*, vol. 3, pp. III–877, IEEE, 2007.

[41] M. E. Tipping, "Sparse bayesian learning and the relevance vector machine," *Journal of machine learning research*, vol. 1, no. Jun, pp. 211–244, 2001.

[42] S. Ji, Y. Xue, and L. Carin, "Bayesian compressive sensing," *IEEE Transactions on signal processing*, vol. 56, no. 6, pp. 2346–2356, 2008.

[43] L. Welch, "Lower bounds on the maximum cross correlation of signals (corresp.)," *IEEE Transactions on Information theory*, vol. 20, no. 3, pp. 397–399, 1974.

[44] S. Datta, S. Howard, and D. Cochran, "Geometry of the welch bounds," *Linear algebra and its applications*, vol. 437, no. 10, pp. 2455–2470, 2012.

[45] H. Rabah, A. Amira, B. K. Mohanty, S. Almaadeed, and P. K. Meher, "Fpga implementation of orthogonal matching pursuit for compressive sensing reconstruction," *IEEE Transactions on very large scale integration (VLSI) Systems*, vol. 23, no. 10, pp. 2209–2220, 2014.

[46] I. Orović, A. Draganić, N. Lekić, and S. Stanković, "A system for compressive sensing signal reconstruction," in *IEEE EUROCON 2017-17th International Conference on Smart Technologies*, pp. 170–175, IEEE, 2017.

[47] S. Vujović, M. Daković, I. Orović, and S. Stanković, "An architecture for hardware realization of compressive sensing gradient algorithm," in *2015 4th Mediterranean Conference on Embedded Computing (MECO)*, pp. 189–192, IEEE, 2015.

[48] H. Hassanieh, P. Indyk, D. Katabi, and E. Price, "Simple and practical algorithm for sparse fourier transform," in *Proceedings of the twenty-third annual ACM-SIAM symposium on Discrete Algorithms*, pp. 1183–1194, Society for Industrial and Applied Mathematics, 2012.

[49] M. E. Ahsen and M. Vidyasagar, "Error bounds for compressed sensing algorithms with group sparsity: A unified approach," *Applied and Computational Harmonic Analysis*, vol. 43, no. 2, pp. 212–232, 2017.

[50] C. Thrampoulidis, S. Oymak, and B. Hassibi, "Recovering structured signals in noise: Least-squares meets compressed sensing," in *Compressed Sensing and Its Applications*, pp. 97–141, Springer, 2015.

[51] L. Stanković, M. Brajović, I. Stanković, C. Ioana, and M. Daković, "Reconstruction error in nonuniformly sampled approximately sparse signals," *IEEE Geoscience and Remote Sensing Letters*, vol. 17, in print, 2020.

[52] I. Stanković, M. Brajović, M. Daković, C. Ioana, and L. Stanković, "Quantization in compressive sensing: A signal processing approach," *IEEE Access*, submitted, 2020.

[53] L. Stankovic, S. Stankovic, and M. Amin, "Missing samples analysis in signals for applications to l-estimation and compressive sensing," *Signal Processing*, vol. 94, pp. 401–408, 2014.

[54] I. Stanković, M. Brajović, M. Daković, and C. Ioana, "Effect of random sampling on noisy nonsparse signals in time-frequency analysis," in *2018 26th European Signal Processing Conference (EUSIPCO)*, pp. 480–483, IEEE, 2018.

[55] J. H. Ender, "On compressive sensing applied to radar," *Signal Processing*, vol. 90, no. 5, pp. 1402–1414, 2010.

[56] G. Zhao, Z. Wang, Q. Wang, G. Shi, and F. Shen, "Robust isar imaging based on compressive sensing from noisy measurements," *Signal Processing*, vol. 92, no. 1, pp. 120–129, 2012.

[57] F. Wang, T. F. Eibert, and Y.-Q. Jin, "Simulation of isar imaging for a space target and reconstruction under sparse sampling via compressed sensing," *IEEE Transactions on Geoscience and Remote Sensing*, vol. 53, no. 6, pp. 3432–3441, 2015.

[58] L. Stanković, T. Thayaparan, V. Popović, I. Djurović, and M. Daković, "Adaptive s-method for sar/isar imaging," *EURASIP Journal on Advances in Signal Processing*, vol. 2008, pp. 1–10, 2007.

[59] L. Stankovic, "Isar image analysis and recovery with unavailable or heavily corrupted data," *IEEE Transactions on Aerospace and Electronic Systems*, vol. 51, no. 3, pp. 2093–2106, 2015.

[60] Y.-S. Yoon and M. G. Amin, "Compressed sensing technique for high-resolution radar imaging," in *Signal Processing, Sensor Fusion, and Target Recognition XVII*, vol. 6968, p. 69681A, International Society for Optics and Photonics, 2008.

[61] V. C. Chen and H. Ling, *Time-frequency transforms for radar imaging and signal analysis*. Artech house, 2002.

[62] E. Arias-Castro and Y. C. Eldar, "Noise folding in compressed sensing," *IEEE Signal Processing Letters*, vol. 18, no. 8, pp. 478–481, 2011.

[63] M. A. Herman and T. Strohmer, "High-resolution radar via compressed sensing," *IEEE transactions on signal processing*, vol. 57, no. 6, pp. 2275–2284, 2009.

[64] L. Zegov, R. Pribić, and G. Leus, "Optimal waveforms for compressive sensing radar," in *21st European Signal Processing Conference (EUSIPCO 2013)*, pp. 1–5, IEEE, 2013.

[65] H. Yan, J. Xu, S. Peng, and X. Zhang, "A compressed sensing method for a wider swath in synthetic aperture imaging," 2013.

[66] H. Yan, J. Xu, and X. Zhang, "Compressed sensing radar imaging of off-grid sparse targets," in *2015 IEEE Radar Conference (RadarCon)*, pp. 0690–0693, IEEE, 2015.

[67] H. Yan, S. Peng, Z. Zhu, J. Xu, and X. Zhang, "Wideband sonar imaging via compressed sensing," in *OCEANS 2014-TAIPEI*, pp. 1–4, IEEE, 2014.

[68] H. Yan, J. Xu, X.-G. Xia, F. Liu, S. Peng, X. Zhang, and T. Long, "Wideband underwater sonar imaging via compressed sensing with scaling effect compensation," *Science China Information Sciences*, vol. 58, no. 2, pp. 1–11, 2015.

[69] H. Yan, J. Xu, X.-G. Xia, X. Zhang, and T. Long, "Underwater sonar target imaging via compressed sensing with m sequences," *Science China Information Sciences*, vol. 59, no. 8, p. 122308, 2016.

[70] J. S. Sewada, C. Ioana, M. Geen, and J. Mars, "Wideband signals for phase differencing sonar systems," in *2018 OCEANS-MTS/IEEE Kobe Techno-Oceans (OTO)*, pp. 1–5, IEEE, 2018.

[71] I. Stanković, C. Ioana, M. Daković, and L. Stanković, "Analysis of off-grid effects in wideband sonar images using compressive sensing," in *OCEANS 2018 MTS/IEEE Charleston*, pp. 1–6, IEEE, 2018.

[72] I. Stanković, C. Ioana, and M. Daković, "Sequence comparison in reconstruction and targeting in underwater sonar imaging," in *OCEANS 2019-Marseille*, pp. 1–10, IEEE, 2019.

[73] I. Stanković, J. S. Sewada, M. Geen, C. Ioana, M. Daković, and J. Mars, "Transmitted sequence influence to sonar target detection using compressive sensing," in *OCEANS 2019-Seattle*, pp. 1–10, IEEE, 2019.

[74] I. Stanković, C. Ioana, M. Brajović, M. Daković, and L. Stanković, "Time-varying cross-range in wideband sonar imaging," in *2019 11th International Symposium on Image and Signal Processing and Analysis (ISPA)*, pp. 318–323, IEEE, 2019.

[75] L. Stanković, M. Daković, I. Stanković, and S. Vujović, "On the errors in randomly sampled nonsparse signals reconstructed with a sparsity assumption," *IEEE Geoscience and Remote Sensing Letters*, vol. 14, no. 12, pp. 2453–2456, 2017.

[76] A. Papoulis and S. U. Pillai, *Probability, random variables, and stochastic processes*. Tata McGraw-Hill Education, 2002.

[77] S. Šajić, N. Maletić, B. M. Todorović, and M. Šunjevarić, "Random binary sequences in telecommunications," *Journal of Electrical Engineering*, vol. 64, no. 4, pp. 230–237, 2013.

[78] G. Björck, "Functions of modulus 1 on zn whose fourier transforms have constant modulus, and cyclic n-roots," 1990.

[79] B. M. Popović, "Fourier duals of björck sequences," in *International Conference on Sequences and Their Applications*, pp. 253–258, Springer, 2010.

[80] A. Mitra, "On pseudo-random and orthogonal binary spreading sequences," *International Journal of Information and Communication Engineering*, vol. 4, no. 6, pp. 447–454, 2008.

[81] D. Chu, "Polyphase codes with good periodic correlation properties (corresp.)," *IEEE Transactions on information theory*, vol. 18, no. 4, pp. 531–532, 1972.

[82] K. Li, L. Gan, and C. Ling, "Convolutional compressed sensing using deterministic sequences," *IEEE Transactions on Signal Processing*, vol. 61, no. 3, pp. 740–752, 2012.

[83] J. J. Benedetto and J. J. Donatelli, "Ambiguity function and frame-theoretic properties of periodic zero-autocorrelation waveforms," *IEEE Journal of Selected Topics in Signal Processing*, vol. 1, no. 1, pp. 6–20, 2007.

[84] A. Kebo, I. Konstantinidis, J. J. Benedetto, M. R. Dellomo, and J. M. Sieracki, "Ambiguity and sidelobe behavior of cazac coded waveforms," in *2007 IEEE Radar Conference*, pp. 99–103, IEEE, 2007.

[85] I. Djurovic, T. Thayaparan, and L. Stankovic, "Sar imaging of moving targets using polynomial fourier transform," *IET Signal Processing*, vol. 2, no. 3, pp. 237–246, 2008.

[86] A. Anand and M. K. Mukul, "Comparison of stft based direction of arrival estimation techniques for speech signal," in *2016 IEEE International Conference on Recent Trends in Electronics, Information & Communication Technology (RTEICT)*, pp. 200–205, IEEE, 2016.

[87] S. Ejaz and M. A. Shafiq, "Comparison of spectral and subspace algorithms for fm source estimation," *Progress In Electromagnetics Research*, vol. 14, pp. 11–21, 2010.

[88] L. Stankovic, V. Popovic, and M. Dakovic, "On the capon's method application in time-frequency analysis," in *Proceedings of the 3rd IEEE International Symposium on Signal Processing and Information Technology (IEEE Cat. No. 03EX795)*, pp. 721–724, IEEE, 2003.

[89] P. Stoica, R. L. Moses, *et al.*, "Spectral analysis of signals," 2005.

[90] I. Murgan, A. Digulescu, I. Candel, and C. Ioana, "Compensation of position offset of acoustic transducers using compressive sensing concept," in *OCEANS 2016 MTS/IEEE Monterey*, pp. 1–4, IEEE, 2016.

[91] M. T. Özgen, "Extension of the capon's spectral estimator to time–frequency analysis and to the analysis of polynomial-phase signals," *Signal processing*, vol. 83, no. 3, pp. 575–592, 2003.

[92] I. Stanković, C. Ioana, and M. Dakovic, "High-resolution local polynomial fourier transform in acoustic signal analysis," in *2017 International Symposium ELMAR*, pp. 163–166, IEEE, 2017.

[93] A. Belouchrani and M. G. Amin, "Time-frequency music," *IEEE Signal Processing Letters*, vol. 6, no. 5, pp. 109–110, 1999.

[94] Y. Jiang and A. Papandreou-Suppappola, "Discrete time-frequency characterizations of dispersive linear time-varying systems," *IEEE Transactions on Signal Processing*, vol. 55, no. 5, pp. 2066–2076, 2007.

[95] C. Ioana, A. Jarrot, C. Gervaise, Y. Stéphan, and A. Quinquis, "Localization in underwater dispersive channels using the time-frequency-phase continuity of signals," *IEEE Transactions on Signal Processing*, vol. 58, no. 8, pp. 4093–4107, 2010.

[96] S. Stanković, I. Orović, and L. Stanković, "Polynomial fourier domain as a domain of signal sparsity," *Signal Processing*, vol. 130, pp. 243–253, 2017.

[97] I. Tolstoy and C. S. Clay, *Ocean acoustics*, vol. 293. McGraw-Hill New York, 1966.

[98] E. K. Westwood, C. T. Tindle, and N. R. Chapman, "A normal mode model for acousto-elastic ocean environments," *The Journal of the Acoustical Society of America*, vol. 100, no. 6, pp. 3631–3645, 1996.

[99] F. B. Jensen, W. A. Kuperman, M. B. Porter, and H. Schmidt, *Computational ocean acoustics*. Springer Science & Business Media, 2011.

[100] W. A. Kuperman and J. F. Lynch, "Shallow-water acoustics," *Physics Today*, vol. 57, no. 10, pp. 55–61, 2004.

[101] M. Stojanovic, "Underwater acoustic communication," *Wiley encyclopedia of electrical and electronics engineering*, 2001.

[102] M. Stojanovic and J. Preisig, "Underwater acoustic communication channels: Propagation models and statistical characterization," *IEEE communications magazine*, vol. 47, no. 1, pp. 84–89, 2009.

[103] C. Ioana, N. Josso, C. Gervaise, J. Mars, and Y. Stéphan, "Signal analysis approach for passive tomography: applications for dispersive channels and moving configuration," 2009.

[104] E. de Sousa Costa, E. B. Medeiros, and J. B. C. Filardi, "Underwater acoustics modeling in finite depth shallow waters," in *Modeling and measurement methods for acoustic waves and for acoustic microdevices*, IntechOpen, 2013.

[105] G. V. Frisk, *Ocean and seabed acoustics: a theory of wave propagation*. Pearson Education, 1994.

[106] J. Zhang and A. Papandreou-Suppappola, "Time-frequency based waveform and receiver design for shallow water communications," in *2007 IEEE International Conference on Acoustics, Speech and Signal Processing-ICASSP'07*, vol. 3, pp. III–1149, IEEE, 2007.

[107] L. Ziomek, *Fundamentals of acoustic field theory and space-time signal processing*. CRC press, 1994.

[108] B. A. McCollom, *Complex wavenumber determination for seismo-acoustic propagation scenarios*. PhD thesis, Colorado School of Mines. Arthur Lakes Library, 2013.

[109] L. Novotny, "Electromagnetic fields and waves," *Lecture Notes: 227-0052-10L [Power Point), ETH Zurich, Photonic Laboratory*, pp. 23–25, 2013.

[110] I. Stakgold and M. J. Holst, *Green's functions and boundary value problems*, vol. 99. John Wiley & Sons, 2011.

[111] J. J. Zhang, A. Papandreou-Suppappola, B. Gottin, and C. Ioana, "Time-frequency characterization and receiver waveform design for shallow water environments," *IEEE Transactions on Signal Processing*, vol. 57, no. 8, pp. 2973–2985, 2009.

[112] V. Katkovnik, "A new form of the fourier transform for time-varying frequency estimation," *Signal Processing*, vol. 47, no. 2, pp. 187–200, 1995.

[113] B. Boashash and P. O'Shea, "Polynomial wigner-ville distributions and their relationship to time-varying higher order spectra," *IEEE Transactions on Signal Processing*, vol. 42, no. 1, pp. 216–220, 1994.

[114] V. Katkovnik, "Discrete-time local polynomial approximation of the instantaneous frequency," *IEEE Transactions on Signal Processing*, vol. 46, no. 10, pp. 2626–2637, 1998.

[115] X. Li, G. Bi, S. Stankovic, and A. M. Zoubir, "Local polynomial fourier transform: A review on recent developments and applications," *Signal Processing*, vol. 91, no. 6, pp. 1370–1393, 2011.

[116] S. Stanković, I. Orović, and E. Sejdić, *Multimedia signals and systems*. Springer, 2012.

[117] L. Stanković, M. Daković, and S. Vujović, "Reconstruction of sparse signals in impulsive disturbance environments," *Circuits, Systems, and Signal Processing*, vol. 36, no. 2, pp. 767–794, 2017.

[118] I. Stanković, I. Orović, M. Daković, and S. Stanković, "Denoising of sparse images in impulsive disturbance environment," *Multimedia Tools and Applications*, vol. 77, no. 5, pp. 5885–5905, 2018.

[119] Z. M. Ramadan, "Efficient restoration method for images corrupted with impulse noise," *Circuits, Systems, and Signal Processing*, vol. 31, no. 4, pp. 1397–1406, 2012.

[120] V. Caselles, A. Chambolle, and M. Novaga, "Total variation in imaging.," *Handbook of mathematical methods in imaging*, vol. 2015, pp. 1455–1499, 2015.

[121] B. Zhang, Z. Zhu, and S. Wang, "A simple primal–dual method for total variation image restoration," *Journal of Visual Communication and Image Representation*, vol. 38, pp. 814–823, 2016.

[122] Z. Wang, A. C. Bovik, H. R. Sheikh, and E. P. Simoncelli, "Image quality assessment: from error visibility to structural similarity," *IEEE transactions on image processing*, vol. 13, no. 4, pp. 600–612, 2004.

[123] M. Brajović, I. Stanković, M. Daković, C. Ioana, and L. Stanković, "Error in the reconstruction of nonsparse images," *Mathematical Problems in Engineering*, vol. 2018, 2018.

List of publications

Journals and book chapters

1. **I. Stanković**, M. Daković, C. Ioana, "Decomposition and Analysis of Signals Sparse in the Dual Polynomial Fourier Transform," Elsevier Microprocessors and Microsystems, vol. 63, pp. 209–215, November 2018.

2. **I. Stanković**, C. Ioana, M. Daković, "On the reconstruction of nonsparse time-frequency signals with sparsity constraint from a reduced set of samples," Elsevier Signal Processing, vol. 142, pp. 480–484, January 2018.

3. **I. Stanković**, M. Brajović, M. Daković, C.Ioana, L. Stanković, "Quantization in Compressive Sensing: A Signal Processing Approach," IEEE Access, vol. 8, pp. 50611–50625, March 2020.

4. **I. Stanković**, M. Brajović, M. Daković, C.Ioana, L. Stanković, "Bit-depth quantization and reconstruction error in images," Signal, Image and Video Processing, accepted, 2020.

5. **I. Stanković**, I. Orović, M. Daković, S. Stanković, "Denoising of Sparse Images in Impulsive Disturbance Environment," Multimedia Tools and Applications, vol. 77, no. 5, pp. 5885–5905, March 2018.

6. L. Stanković, M. Brajović, **I. Stanković**, C. Ioana, M. Daković, "Reconstruction Error in Nonuniformly Sampled Approximately Sparse Signals," IEEE Geoscience and Remote Sensing Letters, accepted for publication.

7. **I. Stanković**, M. Brajović, M. Daković, L. Stanković, "Analysis of Noise in Complex-Valued Binary and Bipolar Sigmoid Compressive Sensing," Telfor Journal, 2019.

8. L. Stanković, M. Daković, **I. Stanković**, S. Vujović, "On the Errors in Randomly Sampled Nonsparse Signals Reconstructed with a Sparsity Assumption," IEEE Geoscience and Remote Sensing Letters, vol. 14, no. 12, pp. 2453–2456, December 2017.

9. N. A. Khan, M. Mohammadi, **I. Stanković**, "Sparse Reconstruction based on iterative TF domain filtering and Viterbi based IF estimation Algorithm," Elsevier Signal Processing, vol. 166, January 2020.

10. L. Stanković, M. Daković, **I. Stanković**, "Compressive Sensing Methods for Reconstruction of Big Sparse Signals," in "Biomedical Signal Processing in Big Data", E. Sejdic ed., CRC Press, 2017.

11. M. Brajović, **I. Stanković**, M. Daković, C. Ioana, L. Stanković, "Error in the Reconstruction of Nonsparse Images," Mathematical Problems in Engineering, vol. 2018

12. L. Stanković, **I. Stanković**, M. Daković, "Nonsparsity Influence on the ISAR Recovery from a Reduced Set of Data," IEEE Transactions on Aerospace and Electronic Systems, December 2016.

Conferences

1. **I. Stanković**, M. Brajović, M. Daković, L. Stanković, C. Ioana, "Quantization Effect in Nonuniform Nonsparse Signal Reconstruction," 9th Mediterranean Conference on Embedded Computing, MECO 2020, Budva (Montenegro), June 2020.

2. **I. Stanković**, M. Brajović, M. Daković, C. Ioana, L. Stanković, "On the Quantization and the Probability of Misdetection in Compressive Sensing," 27th Telecommunications Forum TELFOR 2019, Belgrade (Serbia), November 2019.

3. M. Daković, M. Ponjavić, **I. Stanković**, J. Lerga, C. Ioana, "Time-Frequency Analysis of Ionospheric Whistler Signals," 27th Telecommunications Forum TELFOR 2019, Belgrade (Serbia), November 2019.

4. **I. Stanković**, J. Singh Sewada, M. Geen, C. Ioana, M. Dakovic, J. Mars, "Transmitted Sequence Influence to Sonar Target Detection using Compressive Sensing," IEEE OCEANS 2019, Seattle (WA, USA), October 2019.

5. **I. Stanković**, C. Ioana, M. Brajović, M. Daković, L. Stanković, "Time-Varying Cross-Range in Wideband Sonar Imaging," ISPA 2019, Dubrovnik (Croatia), September 2019.

6. M. Brajović, **I. Stanković**, L. Stanković, M. Daković, "Decomposition of Two-Component Multivariate Signals with Overlapped Domains of Support," ISPA 2019, Dubrovnik (Croatia), September 2019.

7. **I. Stanković**, A. Digulescu, C. Ioana, K. Dayet, "Electric arc detection using compressive sensing," GRETSI, Lille (France), August 2019.

8. **I. Stanković**, C. Ioana, M. Daković, "Sequence Comparison in Reconstruction and Targeting in Underwater Sonar Imaging," IEEE OCEANS 2019, Marseille (France), June 2019.

9. **I. Stanković**, M. Brajović, M. Daković, C. Ioana, "Gradient-Descent Algorithm Performance With Reduced Set of Quantized Measurements," 8th Mediterranean Conference on Embedded Computing, MECO 2019, Budva (Montenegro), June 2019.

10. **I. Stanković**, M. Brajović, M. Daković, L. Stanković, "Complex-Valued Binary Compressive Sensing," 26th Telecommunications Forum TELFOR, Belgrade (Serbia) November 2018.

11. **I. Stanković**, C. Ioana, M. Daković, L. Stanković, "Analysis of off-grid effects in wideband sonar images using compressive sensing," IEEE OCEANS 2018, Charleston (South Carolina, USA), October 2018.

12. M. Brajović, **I. Stanković**, C. Ioana, M. Daković, L. Stanković, "Reconstruction of Rigid Body with Noncompensated Acceleration After Micro-Doppler Removal," 5th International Workshop on Compressed Sensing applied to Radar, Multimodal Sensing, and Imaging (CoSeRa), Siegen, Germany, September 2018.

13. L. Stanković, M. Brajović, **I. Stanković**, C. Ioana, M. Daković, "Analysis of Initial Estimate Noise in the Sparse Randomly Sampled ISAR Signals," 5th International Workshop on Compressed Sensing applied to Radar, Multimodal Sensing, and Imaging (CoSeRa), Siegen, Germany, September 2018.

14. **I. Stanković**, M. Brajović, M. Daković, C. Ioana, "Effect of Random Sampling on Noisy Nonsparse Signals in Time-Frequency Analysis," 26th European Signal Processing Conference EUSIPCO 2018, Rome, Italy, September 2018.

15. **I. Stanković**, C. Ioana, M. Daković, I. Candel, "Sparse Signal Reconstruction in Dual Polynomial Fourier Transform," 7th Mediterranean Conference on Embedded Computing, MECO 2018, Budva, Montenegro, June 2018.

16. **I. Stanković**, I. Djurović, M. Daković, "Adaptive average BM3D filter for reconstruction of images with combined noise," 7th Mediterranean Conference on Embedded Computing, MECO 2018, Budva, Montenegro, June 2018.

17. **I. Stanković**, C. Ioana, M. Daković, "High-Resolution Local Polynomial Fourier Transform in Acoustic Signal Analysis," ELMAR, Zadar (Croatia), September 2017.

18. **I. Stanković**, C. Ioana, M. Daković, "Model-based decomposition of acoustic signals in dispersive environment," GRETSI, Nice (France), September 2017.

19. **I. Stanković**, M. Daković, C. Ioana, "Time-Frequency Signal Reconstruction of Nonsparse Audio Signals," IEEE DSP, London (United Kingdom), August 2017.

20. M. Daković, L. Stanković, B. Lutovac, **I. Stanković**, "On the Fixed-point Rounding in the DFT," IEEE EUROCON, Ohrid (Macedonia), July 2017.

21. **I. Stanković**, M. Daković, C. Ioana, "Decomposition of Signals in Dispersive Channels using Dual Polynomial Fourier Transform," MECO, Bar (Montenegro), June 2017.

22. **I. Stanković**, I. Orović, M. Daković, "Overlapping Blocks in Recontstruction of Sparse Images," 40th International Convention on Information and Communication Technology, Electronics and Microelectronics MIPRO, Opatija (Croatia), May 2017.

23. M. Daković, **I. Stanković**, M. Brajović, L. Stanković,, "Sparse Signal Reconstruction Based on Random Search Procedure," 40th International Convention on Information and Communication Technology, Electronics and Microelectronics MIPRO, Opatija (Croatia), May 2017.

24. M. Daković, **I. Stanković**, J. Ender, L. Stanković, "Sample Selection Strategy in DFT based on Compressive Sensing," 24th Telecommunications Forum TELFOR, Belgrade (Serbia), November 2016.

25. L. Stanković, **I. Stanković**, M. Daković, "Analysis of Noise and Nonsparsity in the ISAR Image Recovery from a Reduced Set of Data," 4th International Workshop on Compressed Sensing Theory and its Applications to Radar, Sonar and Remote Sensing CoSeRa, Aachen (Germany), September 2016.

26. **I. Stanković**, W. Dai, “Reconstruction of Global Ozone Density Data using a Gradient-Descent Algorithm," 58th International Symposium ELMAR, Zadar (Croatia), September 2016.

27. S. Vujović, **I. Stanković**, M. Daković, L. Stanković, “Comparison of a Gradient-Based and LASSO (ISTA) Algorithm for Sparse Signal Reconstruction," 5th Mediterranean Conference on Embedded Computing MECO, Bar (Montenegro), June 2016.

28. **I. Stanković**, I. Orović, S. Stanković, M. Daković, “Iterative Denoising of Sparse Images," 39th International Convention on Information and Communication Technology, Electronics and Microelectronics MIPRO, Opatija (Croatia), May 2016.

29. **I. Stanković**, A. Draganić, “Reconstruction of Video Data based on DCT and Gradient-Descent Method," 23rd Telecommunications Forum TELFOR, Belgrade (Serbia), November 2015.

30. **I. Stanković**, I. Orović, S. Stanković, “Image Reconstruction from a Reduced Set of Pixels using a Simplified Gradient Algorithm," 22nd Telecommunications Forum TELFOR, Belgrade (Serbia), November 2014.

Appendix A

Reconstruction algorithms

This Appendix presents some of the most commonly used algorithms in the compressive sensing theory. This, however, does not exclude the vast number of techniques developed during the years. It simply illustrates some procedures which were successfully implemented in many areas. Additionally, Algorithm 7 presents the algorithm proposed in Chapter 5 of this thesis.

Orthogonal matching pursuit algorithm

Algorithm 1 One-step OMP reconstruction

Input:

- Measurement vector $\mathbf{y}$
- Measurement matrix $\mathbf{A}$
- Number of selected coefficients in each iteration r, by default $r = 1$
- Required precision ε

$\mathbb{K} \leftarrow \emptyset$
$\mathbf{e} \leftarrow \mathbf{y}$
while $\|\mathbf{e}\|_2 > \varepsilon$ **do**
  $(k_1, k_2, \ldots, k_r) \leftarrow$ positions of r highest values in $\mathbf{A}^H\mathbf{e}$
  $\mathbb{K} \leftarrow \mathbb{K} \cup \{k_1, k_2, \ldots, k_r\}$
  $\mathbf{A}_K \leftarrow$ columns of matrix $\mathbf{A}$ selected by set $\mathbb{K}$
  $\mathbf{X}_K \leftarrow \text{pinv}(\mathbf{A}_K)\mathbf{y}$
  $\mathbf{y}_K \leftarrow \mathbf{A}_K\mathbf{X}_K$
  $\mathbf{e} \leftarrow \mathbf{y} - \mathbf{y}_K$
end while
$\mathbf{X} \leftarrow \begin{cases} \mathbf{0} & \text{for positions not in } \mathbb{K} \\ \mathbf{X}_K & \text{for positions in } \mathbb{K} \end{cases}$

Output:

- Reconstructed signal coefficients $\mathbf{X}$

Algorithm 2 Iterative OMP reconstruction

Input: Vector $\mathbf{y}$, matrix $\mathbf{A}$, assumed sparsity K

1: $\mathbb{K} \leftarrow \emptyset$, $\mathbf{e} \leftarrow \mathbf{y}$
2: **for** $i = 1$ **do** K
3: $\quad k \leftarrow$ position of the highest value in $\mathbf{A}^H\mathbf{e}$
4: $\quad \mathbb{K} \leftarrow \mathbb{K} \cup k$
5: $\quad \mathbf{A}_K \leftarrow$ columns of matrix $\mathbf{A}$ selected by set $\mathbb{K}$
6: $\quad \mathbf{X}_K \leftarrow \text{pinv}(\mathbf{A}_K)\mathbf{y}$
7: $\quad \mathbf{y}_K \leftarrow \mathbf{A}_K\mathbf{X}_K$
8: $\quad \mathbf{e} \leftarrow \mathbf{y} - \mathbf{y}_K$
9: **end for**

Output: Reconstructed $\mathbf{X}_R = \mathbf{X}_K$ and positions $\mathbb{K}$.

Iterative hard thresholding algorithm

Algorithm 3 Iterative Hard Thresholding (IHT) Reconstruction Algorithm

Input: Vector $\mathbf{y}$, Matrix $\mathbf{A}$, Assumed sparsity K,
Number of iterations I_t, and parameter τ.

1: $\mathbf{X}_0 \leftarrow \mathbf{0}$
2: **for** $i = 1$ **do** I_t
3: $\quad \mathbf{Y} \leftarrow \mathbf{X}_0 + \tau\mathbf{A}^H(\mathbf{y} - \mathbf{A}\mathbf{X}_0)$
4: $\quad \mathbb{K} \leftarrow \text{sort}(|\mathbf{Y}|)$, indices of K largest $|\mathbf{Y}|$
5: $\quad \mathbf{X}_0 \leftarrow \mathbf{0}$, $\mathbf{X}_0 \leftarrow \mathbf{Y}$ for $k \in \mathbb{K}$, Hard Thresholding
6: **end for**

Output: Reconstructed $\mathbf{X}_R = \mathbf{X}_0$, the set of positions $\mathbb{K}$.

LASSO – ISTA reconstruction algorithm

Algorithm 4 LASSO – ISTA reconstruction

Input:

- Measurement vector $\mathbf{y}$
- Measurement matrix $\mathbf{A}$
- Regularization parameter α
- Sparsity promotion parameter λ

1: $\mathbf{X} \leftarrow \mathbf{0}_{N\times 1}$
2: **repeat**
3: $\quad \mathbf{s} \leftarrow \frac{1}{\alpha}\mathbf{A}^T(\mathbf{y} - \mathbf{A}\mathbf{X}) + \mathbf{X}$
4: $\quad$ **for** $k \leftarrow 1$ to N **do**
5: $$X(k) \leftarrow \begin{cases} s(k) + \lambda & \text{for } s(k) < -\lambda \\ 0 & \text{for } |s(k)| \leq \lambda \\ s(k) - \lambda & \text{for } s(k) > \lambda \end{cases}$$
6: $\quad$ **end for**
7: **until** stopping criterion is satisfied

Output:

- Reconstructed signal coefficients $\mathbf{X}$

Bayesian-based reconstruction algrotihm

Algorithm 5 Bayesian-based reconstruction

Input: Vector $\mathbf{y}$, Matrix $\mathbf{A}$

1: $\alpha_i \leftarrow 1$ ▷ For $i = 1, 2, \ldots, N$
2: $\sigma^2 \leftarrow 1$ ▷ Initial estimate
3: $T_h = 10^2$ ▷ Threshold
4: $\mathbf{p} = [1, 2, \ldots, N]^T$
5: **repeat**
6: $\mathbf{D} \leftarrow$ diagonal matrix with d_i values
7: $\mathbf{\Sigma} \leftarrow (\mathbf{A}^T\mathbf{A}/\sigma^2 + \mathbf{D})^{-1}$
8: $\mathbf{V} \leftarrow \mathbf{\Sigma}\mathbf{A}^T\mathbf{y}/\sigma^2$
9: $\gamma_i \leftarrow 1 - d_i\Sigma_{ii}$ ▷ For each i
10: $d_i \leftarrow \gamma_i/V_i$ ▷ For each i
11: $\sigma^2 \leftarrow \dfrac{\|\mathbf{y} - \mathbf{A}\mathbf{V}\|^2}{M - \sum_i \gamma_i}$
12: $\mathbb{R} \leftarrow \{i : |d_i| > T_h\}$
13: Remove columns from matrix $\mathbf{A}$ selected by $\mathbb{R}$
14: Remove elements from array d_i selected by $\mathbb{R}$
15: Remove elements from vector $\mathbf{p}$ selected by $\mathbb{R}$
16: **until** stopping criterion is satisfied
17: Reconstructed vector $\mathbf{X}$ nonzero coefficients are in vector $\mathbf{V}$ with corresponding positions in vector $\mathbf{p}$, $X_{p_i} = V_i$

Output:

- Reconstructed signal vector $\mathbf{X}_R = \mathbf{V}$, the set of positions $\mathbb{K} = \mathbf{p}$.

Gradient-based reconstruction algorithm

Algorithm 6 Gradient-based image reconstruction

Input:

- Set of the uncorrupted pixel positions $\mathbb{N}_A$
- Corrupted image $\mathbf{x}$

Output:

- Reconstructed image $\mathbf{x}_R$

function GradRec($\mathbf{x}, \mathbb{N}_A$)
  $x_a^{(0)}(m,n) \leftarrow \begin{cases} x(m,n) & \text{for } (m,n) \in \mathbb{N}_A \\ 0 & \text{for } (m,n) \notin \mathbb{N}_A \end{cases}$
  $\Delta \leftarrow \max_{m,n} |x_a^{(0)}(m,n)|$
  $p \leftarrow 0$
  repeat
    repeat
      $\mathbf{x}_a^{(p+1)} \leftarrow \mathbf{x}_a^{(p)}$
      for all $(m_i, n_i) \notin \mathbb{N}_A$ **do**
        $\mathbf{x}_a^{+} \leftarrow \mathbf{x}_a^{(p)}$
        $x_a^{+}(m_i,n_i) \leftarrow x_a^{+}(m_i,n_i) + \Delta$, $\mathbf{X}_a^{+} \leftarrow \mathrm{DCT2}\{\mathbf{x}_a^{+}\}$
        $\mathbf{x}_a^{-} \leftarrow \mathbf{x}_a^{(p)}$
        $x_a^{-}(m_i,n_i) \leftarrow x_a^{-}(m_i,n_i) - \Delta$, $\mathbf{X}_a^{-} \leftarrow \mathrm{DCT2}\{\mathbf{x}_a^{-}\}$
        $g(m_i,n_i) \leftarrow \|\mathbf{X}_a^{+}\|_1 - \|\mathbf{X}_a^{-}\|_1$
        $x_a^{(p+1)}(m_i,n_i) \leftarrow x_a^{(p)}(m_i,n_i) - \mu g(m_i,n_i)$
      end for
      $p \leftarrow p + 1$
    until stopping criterion is satisfied
    $\Delta \leftarrow \Delta/3$
  until required precision is achieved
  $\mathbf{x}_R \leftarrow \mathbf{x}_a^{(p)}$
  return $\mathbf{x}_R$
end function

Proposed method in Chapter 5

Algorithm 7 Proposed method in Chapter 5

Input:

- Image $\mathbf{x}$ of size $N \times M$ with possibly corrupted pixels
- Number of pixels to be selected in each iteration r

Output:

- Reconstructed image $\mathbf{x}$
- Set of the uncorrupted pixels $\mathbb{N}_A$

$\Delta \leftarrow \max_{m,n} |x(m,n)|$
$\mathbb{N}_A \leftarrow \{(m,n) : m = 1,2,\ldots,M,\ n = 1,2,\ldots,N\}$
$\mathbb{N}_x \leftarrow \emptyset$
repeat
  for all $(n,m) \in \mathbb{N}_A$ **do**
    $\mathbf{x}^+ \leftarrow \mathbf{x}$
    $x^+(m,n) \leftarrow x^+(m,n) + \Delta$
    $\mathbf{X}^+ \leftarrow \mathrm{DCT2}\{\mathbf{x}^+\}$
    $\mathbf{x}^- \leftarrow \mathbf{x}$
    $x^-(m,n) \leftarrow x^-(m,n) - \Delta$
    $\mathbf{X}^- \leftarrow \mathrm{DCT2}\{\mathbf{x}^-\}$
    $g(m,n) \leftarrow \|\mathbf{X}^+\|_1 - \|\mathbf{X}^-\|_1$
  end for
  Select r pixels $(m,n) \in \mathbb{N}_A$ with highest $|g(m,n)|$
  Add selected pixels to set $\mathbb{N}_x$
  Remove selected pixels from set $\mathbb{N}_A$
  $\mathbf{x} \leftarrow \textsc{GradRec}(\mathbf{x}, \mathbb{N}_A)$ ▷ Algorithm 6
until the sparsity is not significantly changed
Optionally, perform sparsification of the reconstructed image
return $\mathbf{x}$, $\mathbb{N}_A$

Abstract — In signal processing, the theory behind compressive sensing presented a successful sampling technique in different fields. The idea of using a small number of measurements for the acquisition improves the efficiency of storage, memory and transmission of signals. Since many signals in the nature can be represented as sparse in some representation domain, the technique showed huge potential in medicine, telecommunications, radar systems, etc. Although very successful, the idea of compressive sensing is not yet developed in the underwater acoustics. Acoustic signals transmitted under water introduce many complex characteristics difficult for their analysis. Problems occur in the process of transmitting and receiving signals due to its dispersive media, especially in shallow water environments as a representative example of a dispersive channel. Additionally, dispersivity produces multiple nonlinear components. The non-stationary nature of such signals makes it suitable for the analysis using time-frequency tools under the signal processing approach. In the compressive sensing sense, non-stationary signals are only approximately sparse or nonsparse in the corresponding transformation domain.

Keywords: Signal processing, Compressive sensing, Sparse signal processing, Non-stationary signals, Reconstruction, Decomposition, Dispersive channels.

Résumé — Dans le traitement du signal, la théorie derrière la détection compressive a présenté une technique d'échantillonnage réussie dans différents domaines. L'idée d'utiliser un petit nombre de mesures pour l'acquisition améliore l'efficacité du stockage, de la mémoire et de la transmission des signaux. Étant donné que de nombreux signaux dans la nature peuvent être représentés comme clairsemés dans certains domaines de représentation, la technique a montré un énorme potentiel en médecine, en télécommunications, en systèmes radar, etc. Bien que très réussie, l'idée de la détection compressive n'est pas encore développée dans l'acoustique sous-marine. Les signaux acoustiques transmis sous l'eau présentent de nombreuses caractéristiques complexes difficiles à analyser. Des problèmes surviennent dans le processus de transmission et de réception des signaux en raison de ses milieux dispersifs, en particulier dans les environnements en eau peu profonde comme exemple représentatif d'un canal dispersif. De plus, la dispersivité produit plusieurs composants non linéaires. La nature non stationnaire de ces signaux le rend approprié pour l'analyse à l'aide d'outils temps-fréquence dans le cadre de l'approche de traitement du signal. Au sens de la compression, les signaux non stationnaires ne sont approximativement que clairsemés ou non dans le domaine de transformation correspondant.

Mots clés : Traitement du signal, Détection compressive, Traitement des signaux clairsemés, Signaux non stationnaires, Reconstruction, Décomposition, Canaux dispersifs.

Rezime — U obradi signala, teorija iza kompresivnog odabiranja predstavlja uspjesnu tehniku uzorkovanja u razlicitim oblastima. Ideja koriscenja malog broja mjerenja uzoraka poboljsava efikasnost skladistenja, memorije i prenosa signala. Buduci da se mnogi signali u prirodi mogu predstaviti kao rijetki u odredenom domenu reprezentacije, ova tehnika pokazala je ogroman potencijal u medicini, telekomunikacijama, radarskim sistemima, itd. Iako je veoma uspjesna, ideja kompresivnog odabiranja jos nije razvijena u podvodnoj akustici. Akusticni signali koji se prenose pod vodom uvode mnoge slozene karakteristike kompleksne za njihovu analizu. Problemi se javljaju u procesu prenosenja i primanja signala zbog disperzivnih medija, posebno u plitkom vodenom okruzenju kao reprezentativan primer disperzivnog kanala. Pored toga, disperzitet proizvodi vise nelinearnih komponenti. Nestacionarna priroda takvih signala ga cini pogodnim za analizu koristeci vremenske-frekvencije alate u obradi signala. U teoriji kompresivnog odabiranja senzora, nestacionarni signali su samo priblizno rijetki ili nesparzni u odgovarajucoj domeni transformacije.

Kljucne rijeci: Obrada signala, Kompresivno odabiranje, Obrada rijetkih signala, Nestacionarni signali, Rekonstrukcija, Dekompozicija, Disperzivni kanali.

GIPSA Lab, INP Grenoble / Faculty of Electrical Engineering, University of Montenegro
Grenoble, France / Podgorica, Montenegro